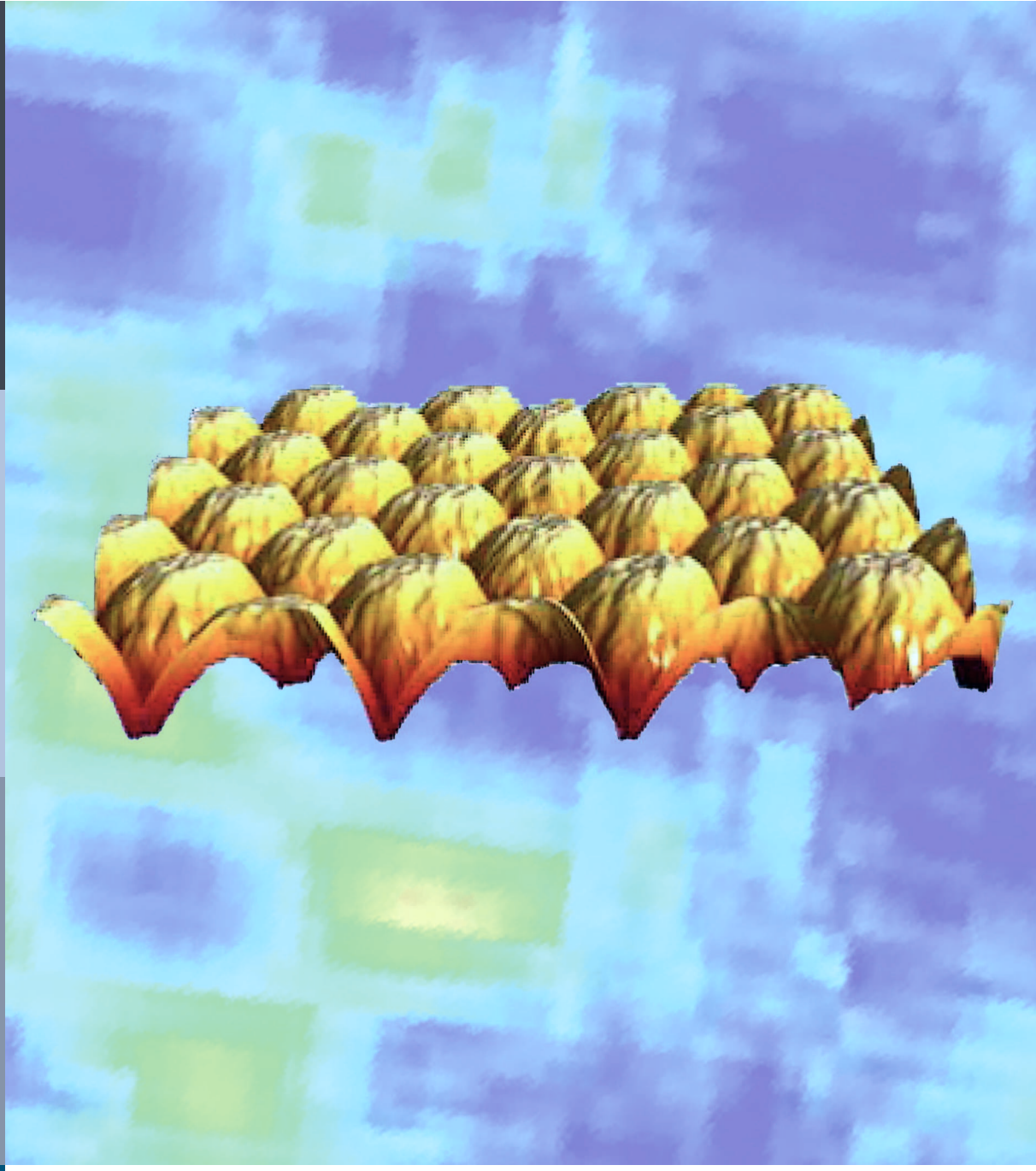

Optics of Nanostructured Thin-Film Silicon Solar Cells

Christian Haase

Mitglied der Helmholtz-Gemeinschaft

JÜLICH
FORSCHUNGSZENTRUM

Schriften des Forschungszentrums Jülich
Reihe Energie & Umwelt / Energy & Environment Band / Volume 85

Forschungszentrum Jülich GmbH
Institute of Energy Research (IEF)
Photovoltaics (IEF-5)

Optics of Nanostructured Thin-Film Silicon Solar Cells

Christian Haase

Schriften des Forschungszentrums Jülich
Reihe Energie & Umwelt / Energy & Environment Band / Volume 85

ISSN 1866-1793 ISBN 978-3-89336-671-2

Bibliographic information published by the Deutsche Nationalbibliothek.
The Deutsche Nationalbibliothek lists this publication in the Deutsche Nationalbibliografie; detailed bibliographic data are available in the Internet at http://dnb.d-nb.de.

Publisher and Distributor:	Forschungszentrum Jülich GmbH Zentralbibliothek 52425 Jülich Phone +49 (0) 24 61 61-53 68 · Fax +49 (0) 24 61 61-61 03 e-mail: zb-publikation@fz-juelich.de Internet: http://www.fz-juelich.de/zb
Cover Design:	Grafische Medien, Forschungszentrum Jülich GmbH
Printer:	Grafische Medien, Forschungszentrum Jülich GmbH
Copyright:	Forschungszentrum Jülich 2010

Schriften des Forschungszentrums Jülich
Reihe Energie & Umwelt / Energy & Environment Band / Volume 85

D 579 (Diss., Bremen, Jacobs Univ., 2010)

ISSN 1866-1793
ISBN 978-3-89336-671-2

Table of contents

Symbols & Acronyms	Description
a	the absorption coefficient
α	angle of light incidence
α_t	angle of total internal reflection
a-Si:H	amorphous silicon (solar cell)
A	surface area
Ag	silver
Al	aluminium
$Abs_{front,}$	parasitic absorption in the front contact
Abs_{back}	parasitic absorption in the back contact
$A_{Deckman}$	theoretical absorption probability
A^{opt}	optical absorption
$\vec{b}$	magnetic field vector
$\vec{B}$	magnetic flux
CdTe	cadmium telluride (solar cell)
CIGS	Cu(In,Ga)(S,Se) copper/indium/gallium/(di)selenide (solar cell)
χ_{magn}	magnetical susceptibility
χ_{el}	electric susceptibility
d	absorber layer thickness of
$\vec{d}$	electrical displacement field vector
dl	length of the antenna element
$\vec{D}$	electrical displacement field (also electrical flux)
Δt	time step width of a FIT simulation step
$\vec{e}_x$	electrical field vector
$\vec{E}$	electrical field
E_F	Fermi energy
E_g	bandgap energy
EQE	external quantum efficiency
$\boldsymbol{\varepsilon}$	electric permittivity
FDTD	Finite-Difference-Time-Domain method
FEM	finite element method
FF	fill factor
FIT	Finite Integration Technique
G	groove size of grating
$\vec{h}$	magnetic field vector
$\vec{H}$	magnetic field
H_2	hydrogen
HCl	hydrochloric acid
HRSEM	high-resolution scanning electron microscope
I	current
I_0	saturation current
I_{abs}	absorbed photon flux
I_{esc}	photon flux that is escaping through the surface A
I_{in}	flux that is entering into the surface A
I_{MPP}	current at maximum power point
I_{photo}	photo current
I_{sc}	short circuit current

$j(\Omega)$	photon flux density per angular element
$\vec{J}$	current density
φ	zenith angle to the radial distance r_d,
k	Boltzmann constant
L	thickness of a weakly absorbing material layer
$\vec{M}$	magnetisation
$\boldsymbol{\mu}$	magnetic permeability
µc-Si	microcrystalline silicon (solar cell)
n	diode factor
n_{Si}	refractive index of silicon
η	energy conversion efficiency
υ	frequency
P	period size
$\vec{P}$	polarisation
PBG	photonic bandgap material
PC	photonic crystal
PECVD	plasma enhanced chemical vapour deposition
PMMA	polymer material
PVD	physical vapour deposition
P_{in}	power of incident sun light
P_{MPP}	maximum possible electrical power
P_{out}	maximal electrical power
q	elementary electric charge
r_d	radial distance from antenna
r_{single}	reflection after single light incidence
r_{total}	total reflection
$R(\alpha)$	angle (of incidence) dependent reflection
R_{front}	reflection losses at front interface
R_L	load resistance
R_P	parallel resistance
R_S	series resistance
R_{SH}	shunt resistance
R_{TCO}	resistance of the front TCO
V	voltage
V_{oc}	open circuit voltage
V_{MPP}	voltage at maximum power point
SiH_4	silane gas
σ	electrical conductivity
T	temperature
TCO	transparent conductive oxide
TFT	thin-film transistor
TiO_2	titan dioxide
V	volume
w	radian frequency
wt %	weight percent
ZnO	zinc oxide
ZnO:Al	aluminium doped zinc oxide

Introduction

A solar cell is an optoelectronic device that converts light energy into electrical energy. This is based on the photovoltaic effect that was first investigated by Becquerel in 1837. In the Bell Laboratories the first solar cell was made in 1953 by Chapin, Fuller and Pearson. The first commercial interest in solar cells was the power supply of satellites. In the meantime many solar cell concepts have been developed [1-2]. At the moment the world market for solar cells is dominated by crystalline solar cells [3]. Today several thin-film cell concepts based on amorphous silicon (a-Si:H), cadmium telluride (CdTe) and copper / indium / gallium / (di)selenide (CIGS: Cu(In,Ga)(S,Se)) are going into commercial production as the thin-film solar cell technology is already providing similar or even lower costs per watt peak than the standard crystalline silicon solar cell [4-7]. The steep "learning curve" for thin-film technologies is expected to bring the production costs down even below 1 €/W(peak). This would lead to the grid parity, the point at which photovoltaic electricity is equal to or cheaper than grid power. Photovoltaic production has been doubling every two years, increasing by an average of ~ 50 percent per year since 2002, making it the world's fastest-growing energy technology. Until today cumulative global installations have reached 15200 megawatts. For an unlimited growth of productions capacities of thin-film solar cells the absorber material amorphous silicon plays a special role in contrast to CdTe or CIGS cells as it is not volume limited like telluride or indium or toxic like cadmium [6]. A short energy payback time of about 1 year of the energy needed for the solar cell production has been reached for thin-film silicon modules [8]. Advantages under non ideal conditions like higher outdoor temperatures or a high amount of non direct sun light lead to a plus of produced electricity per installed watt (peak) for thin-film silicon in comparison to crystalline silicon modules [4]. The energy conversion efficiency of thin-film silicon solar cell modules is today mainly below 10 % and thus about half of the efficiency of crystalline silicon modules. The main reason is the use of very thin (and thus cheaper) silicon absorber layers with a total thickness of ~ 2 µm in comparison to an absorber thickness of ~ 200 µm for crystalline silicon cells. This leads to a lower absorption of photons and less current is generated in the thin-film silicon solar cell. As the features of a thin-film solar cell are in the micrometer and sub-micrometer range new preparation methods and analysis techniques, so called nanotechnologies, are necessary. The realization of nanooptics with standard concepts is inhibited by the Abbe-limit. In nanostructures, like noble metal nano particles or nanogratings, high intensity electromagnetic fields have been found very close to the structures. First explanations with strong

simplifications are given by the effective medium theory. A thorough understanding of the physics involved at the transition between optics and subwavelength optics must be developed and applied to the thin-film silicon solar cell to reach higher energy conversion efficiencies.

To exclude today's experimental preparation limitations nanostructures are computationally investigated in the present study using the Finite Integration Technique, a numerical simulation method that solves the Maxwell equations in 3 dimensions.

- As a first approach to get insight into light propagation in thin-film silicon solar cells subwavelength grating couplers are integrated into the solar cell architecture. This is a reduction of the many degrees of freedom of a solar cell design to a simple structure.

- The gratings couplers are defined by their period size, groove height and shape. Variations of these parameters with a focus on the red light that has to be trapped more effectively are performed.

- Optical measurements of line grating prototypes are directly compared to the corresponding optical simulations.

- Besides the light trapping of light also the light in-coupling properties are of great importance. The sun light must enter into the solar cell with as little reflection as possible.

- In a periodic unit cell simulation the fixed parameters like the layer thicknesses need to be varied to be able to give general design rules.

- Every parameter of the simulation model needs to be investigated to guarantee a reproducible convergence of the simulation.

- Solar cell designs are varied from simple 1D line grating to 2D and 3D pyramids with multistep or smooth interfaces.

- The shape of the front or back interface needs to be investigated.

- The influence of an unsymmetrical structure is compared to the corresponding symmetrical structure.

- To understand the optical randomisation effect that is introduced by a random nano-texture a direct comparison between a random and periodic design is performed.

Chapter 1 deals with the thin-film silicon solar cell concept and the characteristically involved solar cell parameters. In Chapter 2 the properties and the preparation of the different thin-film layers are introduced. Chapter 3 explains the Yablonovitch limit of the photogeneration. The simulation tool used in this investigation, the Finite integration technique (FIT), is introduced in Chapter 4. The basic model of a one dimensional line grating coupler for enhanced light trapping integrated in a thin-film silicon solar cell is introduced in Chapter 5. The important texture parameters of a grating solar cell are investigated and a short circuit current for an AM1.5 spectrum is calculated to evaluate the light trapping potential of new texture designs. First prototypes of line grating solar cells are presented. In Chapter 6 the texture parameters are expanded to 2D and 3D textures and the back reflector design is investigated. In Chapter 7 square based pyramids with flat interfaces are used as period light trapping structure and the opening angles of these pyramids for an enhanced photo current are calculated. In the last Chapter 8 quasi random structures are introduced with features similar to the common random light trapping structures. The quasi random structures are compared to the periodic structures and their potential is discussed.

The accumulated knowledge of optical simulations and solar cell prototypes has led to a number of design rules to understand and develop new thin-film silicon solar cell architectures with integrated nanostructures.

References Introduction:

[1] A. Goetzberger, C. Hebling, H.-W. Schock: Photovoltaic materials, history, status and outlook. Materials Science and Engineering R 40 (2003), p. 1- 46
[2] J. P. Benner, L. Kazmerski: Photovoltaics: Gaining greater visibility; IEEE Spectrum 36 (1999), p. 34 - 42
[3] P. Maycock; PV Review. Refocus 6 (2005), p. 18-22

[4] S. Hegedus, Thin film solar modules: the low cost, high throughput and versatile alternative to Si wafers.” Progress in Photovoltaics: Research and Applications 14, no. 5 (2006): 393-411

[5] K. L. Chopra, P. D. Paulson, and V. Dutta. “Thin-film solar cells: an overview.” Progress in Photovoltaics: Research and Applications 12, no. 2-3 (2004): 69-92.

[6] M. Green, Consolidation of thin-film photovoltaic technology: the coming decade of opportunity. Progress in Photovoltaics: Research and Applications 14, no. 5 (2006): 383-392.

[7] Y. Hamakawa, Thin-Film Solar Cells: Next Generation Photovoltaics and Its Applications. Springer, 2004

[8] V. Fthenakis, E. Alsema; (2006), Photovoltaics Energy Payback Times, Greenhouse Gas Emissions and External Costs: 2004–early 2005 Status, Progress In Photovoltaics: Research and Applications, 14, 3, p. 275-280.

1 The thin-film silicon solar cell concept

1.1 Solar cell principle

In a photovoltaic cell solar radiation is converted into electrical power. For every semiconducting solar cell the basic mechanism is the same: The absorption of a photon by exciting an electron from the valence band to the conduction band contributes to the electrical current within the solar cell if the carriers recombine neither in the absorber layer volume nor at the surfaces or interfaces of the device. A high optical absorption and a minimized carrier recombination are the essential features for an efficient power conversion.

The power of most electrical devices is determined by the product of current (I) and voltage (V). From the IV-curve the power output of a solar cell can be determined.

1.2 Thin-film silicon solar cell

A thin-film silicon solar cell consists of an amorphous or microcrystalline single junction layer or a tandem configuration with both absorber layers. In every case a pin-diode structure is necessary, i.e. a p- and n- doped layer is generating an electric field over the sandwiched intrinsic i-layer. The layer concept is shown in Fig. 1.1. On a glass sheet the transparent electrical oxide (TCO) front contact is deposited followed by the pin diode layers. A single silver (Ag) layer or a 2-layer system like TCO/Ag or TCO/white paint are used as the electrical back contact of the device.

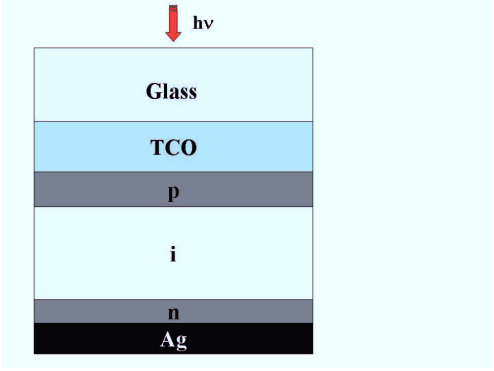

Fig. 1.1: Scheme of a thin-film silicon solar cell in p-i-n (doped) superstrate configuration deposited on a glass substrate.

In the silicon absorber layer the absorption of photons leads to the generation of electron-hole pairs. The generated electron hole pairs are separated by means of the electric field that is created by the p- and n-layer. The photo generated holes drift to the p-layer and the electron drift to the n-layer. If both charge carriers reach the front- and back contact without recombination via e.g. defects a photocurrent can be measured. In contrast to a classical silicon solar cell with an absorber layer thickness (d) of $d \sim 200$ µm, the transport of charged carriers in a thin-film silicon solar cell is dominated by the electrical field. Thin-film silicon solar cells are called "drift cells". The collection of charge carriers depends strongly on the intrinsic field. Therefore, these diodes have a voltage dependent photocurrent [1.1-3].

$$I_{Photo} = I_{Photo}(V) \tag{1.1}$$

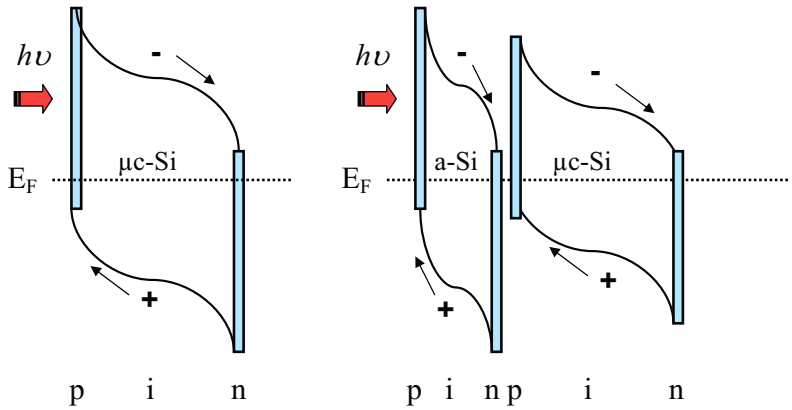

Fig. 1.2: Band diagram of a thin-film silicon solar cell in single junction (left) and tandem junction configuration (right).

To use the sun spectrum more effectively a solar cell with two or more absorber layer can be used. (tandem-, triple-cell etc.) The absorbers have different band gaps or in very advance setup a continuous band gap grading over the entire absorber layer. The tandem junction solar cell solar cell is then a series connection of two single solar cells. The front cell (top cell) can be made of amorphous silicon (a-Si:H) with a bandgap E_g of ~1.8 eV. The lower absorber

layer (bottom cell) can be made of microcrystalline silicon (μc-Si:H) with an E_g of 1.14eV. The top cell absorbs the blue spectrum of the sunlight and the bottom cell the red and infrared spectrum. The use of two or more absorbers with different bandgap materials reduces the generation of "hot carriers" with much excess energy that will be lost as heat through almost immediate thermalization of these hot carriers to the band edge. On the other hand it makes the device more complicated as more layers have to be grown on top of each other and besides this morphological issue the series connection of the single diodes have to be matched to each other, as the lowest current of the both diodes would limit the photocurrent in the devices. The current matching can be understood with Fig. 1.2. As the electrons generated in the top cell and the holes generated in the bottom cell recombine at the internal n/p-contact the number of electron-hole pairs generated in both diodes needs to be equal.

This current matching within a tandem cell can be done with an adaption of the thickness of each diode, a variation of the bandgap and also with a sophisticated light management with the help of an intermediate (diffractive) reflector [1.4] or different back reflector systems.

The variation of the band gap of the a-Si:H top cell can be done, for example by alloying with carbon or oxygen towards higher, with germanium towards lower photon energies: 1.7 eV < E_g(a-Si:H) < 1.9 eV. [1.3]

1.3 Characteristics of a single junction solar cell

The main parameters of a solar cell can be derived from the dark *IV*-curve, the *IV*-curve under illumination and the quantum efficiency measurement. Under dark conditions the diode factor n and the saturation current I_0 can be determined. The *IV*-curve under illumination gives the open circuit voltage V_{OC}, the short circuit current I_{sc}, the fill factor FF and the energy conversion efficiency η [1.2]. To understand the solar cell and the characteristic parameters in detail it is a common approach to discuss the properties with the help of an equivalent circuit diagram. An ideal solar cell is a current source that is connected in parallel to a diode. The ohmic losses in the solar cell are given by the resistances R_S (series resistance) and R_P (parallel resistance). The series resistance is originating in the resistance of the contacts and the material quality of the layers. The resistance of the front TCO is a critical issue and is given by R_{TCO}. The parallel resistance R_P represents the leakage currents in the cell. R_S and R_P are dependent on the illumination intensity which is proportional to the number of generated carriers. R_L denotes the load resistance and R_{SH} the resistance introduced by shunts.

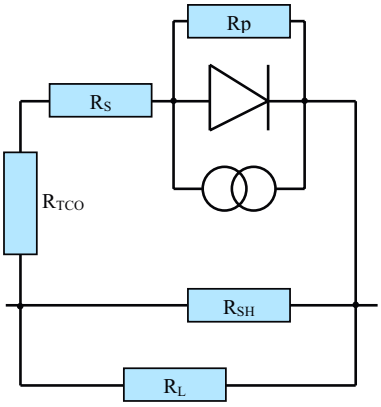

Fig. 1.3: Equivalent circuit diagram of a thin-film silicon solar cell.

1.4 Dark IV-curve

The dark *IV*-curve as shown in Fig. 1.4 can be explained with the diode equation. It is for $n = 1$ equivalent to the Shockley-equation [1.5]:

$$I(V) = I_0 \cdot \left(\exp\left(\frac{qV}{nkT} \right) - 1 \right) \tag{1.4}$$

With $I(V)$ as current, V the applied voltage, I_0 the saturation current, n the ideality or diode factor, T the temperature, q the elementary electric charge and k the Boltzmann constant.

The ideality factor n is an empiric parameter, which varies for high quality thin-film silicon solar cells between 1 and 2. n is inverse proportional to the gradient of the dark *IV*-curve on a logarithmic scale. It gives hints where the recombination takes place.

$n = 1$ The recombination takes place in the field free regions of the solar cell, the n- and p-layers.

$n = 2$ The recombination takes place in the i-layer. Here an electric field is present.

This is in contrast to a standard crystalline silicon solar cell where the wafer is p-doped and a highly doped n+ region is diffused in. Only where both doped layers are adjacent the electric field is present (space charge region). In novel back contact crystalline silicon solar cell designs alternating n- and p-regions and their fields are located at the backside of the solar cell to optimize the carrier extraction and minimize the recombination losses [1.6].

For crystalline wafer solar cells the life time measurement of generated carriers is one of the most important techniques as it determines the quality of the material. A recombination of carriers needs to be avoided until the carriers are separated by the field.

For high quality thin-film silicon solar cells a mix of recombination paths in the i-layer and in the doped regions takes place. This leads to diode factor $n = 1.5 – 1.8$.

From the measured dark *IV*-curve also the saturation current I_0 can be derived for $V = 0$ volt.

For negative and small positive voltages (Fig. 1.4, region (A)) the shunt resistance induced by local shunts dominates the *IV*-curve. In region (B) the diode behaviour is mainly unaffected by resistances and in region (C) the TCO and series resistance influences the *IV*-curve.

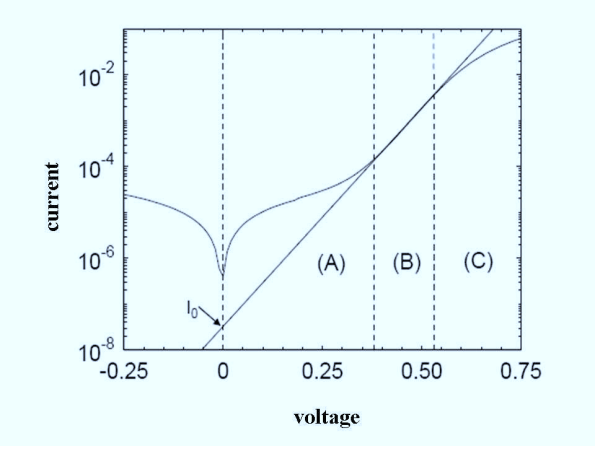

Fig. 1.4: Measurement of a typical dark IV-curve. In region (A) the shunt resistance, in (B) the diode behaviour and in (C) the TCO and series induced resistances influence the IV-curve.

1.5 *IV*-curve under illumination

Under illumination an additional current $I_{Photo}(V)$, the photocurrent is generated. Based on a superposition of dark current and photocurrent the illuminated *IV*-curve is given by

$$I(V) = I_0 \cdot (\exp(q(V - I(V)(R_{TCO} + R_S))/nkT - 1)) - I_{Photo}(V) \tag{1.5}$$

In the ideal case all photo generated carriers are collected by the applied voltage.

By definition the current for $V = 0$ is called the short circuit current I_{sc}.

$$I_{Photo}(V = 0) = I_{sc} \tag{1.6}$$

Usually the material quality of thin-film silicon is too low due to the limiting life time and the mobility of the carriers. Therefore, with increasing voltage

$$I_{Photo}(V) < I_{sc} \tag{1.7}$$

The open circuit voltage V_{OC} is present for the open circuit operation of the device. The current is zero. This can be seen in Fig. 1.5.

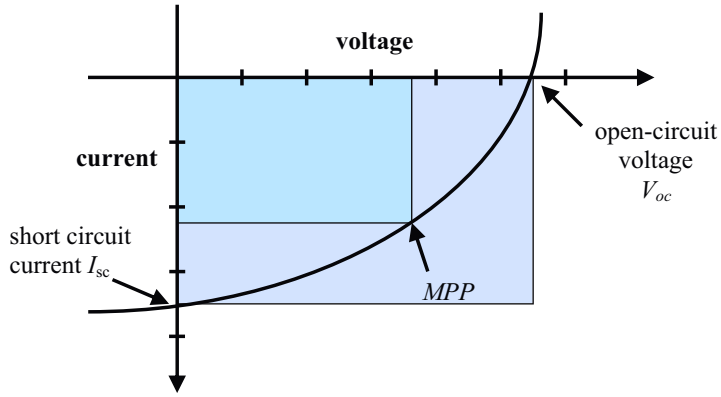

Fig. 1.5: Typical experimental IV-curve of an illuminated p-i-n diode. An ideal IV-curve has a fill factor FF = 100 %, if the blue area is as big as the grey area. From this IV-curve the efficiency of the solar cell can be derived.

The fill factor *FF* is defined as the ratio of maximum possible electrical power (P_{MPP})

$$P_{MPP} = V_{MPP} \cdot I_{MPP} \tag{1.8}$$

and the product of V_{oc} and I_{sc}:

$$FF = \frac{V_{MPP} \cdot I_{MPP}}{V_{oc} \cdot I_{sc}} \tag{1.9}$$

The conversion efficiency η of a solar cell defined as the ratio of maximal electrical power ($P_{out} = P_{MPP}$) and the incident sun light power P_{in}. It can be determined by the parameters of the illuminated *IV*-curve:

$$\eta = \frac{P_{out}}{P_{In}} = \frac{V_{oc} \cdot I_{sc} \cdot FF}{P_{in}} \tag{1.10}$$

References Chapter 1:

[1.1] M. Green, Silicon Solar Cells: Advanced Principles and Practice

[1.2] M. Green, Solar Cells: Operating Principles, Technology and System Applications

[1.3] Brendel, R. Thin-film crystalline silicon solar cells, Wiley-VCH, 2003

[1.4] P. Obermeyer, C. Haase, H. Stiebig, Applied Physics Letters 92, 181102, 2008

[1.5] Shockley, William - Electrons and holes in semiconductors, with applications to transistor electronics, Krieger (1956) ISBN 0-88275-382-7

[1.6] Presentation of SunPower at IEEE 33th, San Diego, 2008, Proceedings in print

2 Thin-film materials

2.1 Thin-film silicon solar cells on glass substrate

The solar cell based on the superstrate concept consists of a thin-film silicon layer stack deposited on a glass substrate. The thin-films have a total thickness of a few micrometers only. As an absorber layer amorphous or microcrystalline silicon is used or a layer stack of amorphous and microcrystalline silicon, the so called tandem solar cell configuration. The electrical contact layer is usually a sputtered TCO (transparent conducting oxide (ZnO)) as a front contact, a sputtered or evaporated silver back contact or a back reflector combination of an 80 nm thick back TCO in between the silicon and the silver layer.

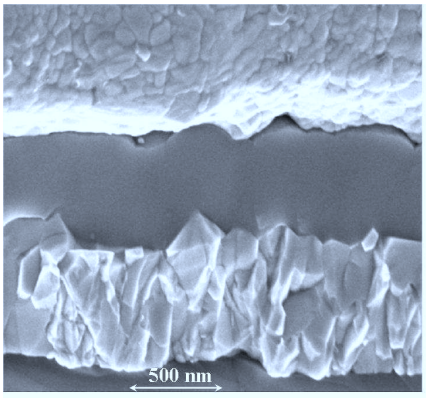

Fig. 2.1: High-resolution scanning electron microscope (HRSEM) cross section of a thin-film silicon solar cell. Layers from top to bottom are: sputtered silver back reflector, amorphous silicon, sputtered and post-etched ZnO and a glass substrate. Picture reprinted from B. Rech et al. [2.1].

2.2 Microcrystalline and amorphous silicon prepared by plasma enhanced chemical vapour deposition (PECVD)

The amorphous and microcrystalline absorber layers are deposited from the gas phase. In a process chamber the gases Silane (SiH_4) and hydrogen (H_2) are decomposed and thus a deposition reaction of silicon is possible. The ignition of plasma leads to a large amount of silane gas precursors based on SiH_3 and SiH_4 in a low temperature deposition regime. In a plasma the ability of the positive and negative charges to move somewhat independently makes the plasma electrically conductive so that it responds strongly to electromagnetic fields. Alternating high frequent electromagnetic fields are used in a PECVD chamber to continuously excite the plasma. The ionized gas molecules are accelerated by an electrical field and deposited on the glass substrate. For a high amount of crystalline silicon phase and larger silicon crystal grains the material is the so-called microcrystalline silicon (in Fig. 2.2, left side). For a low percentage of crystal grains the amorphous phase occurs (right side of Fig. 2.2).

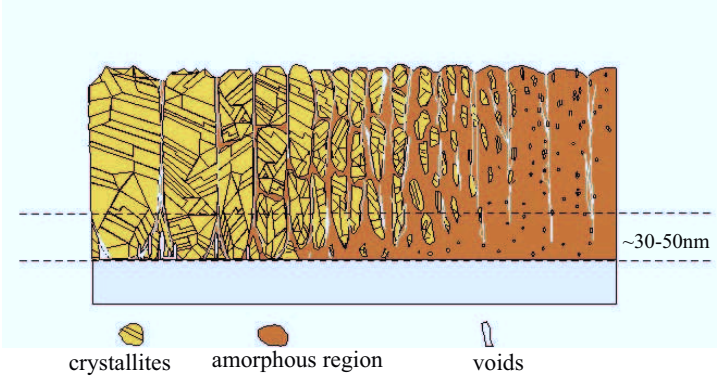

Fig. 2.2: Morphology of thin-film silicon with a more crystalline phase on the left side and a more amorphous phase on the right side [2.2].

The morphology of the silicon layer and the amount of amorphous or crystalline volume fraction depends on the deposition parameters, as summarized in the following table.

deposition parameter :	**consequence for silicon phase :**
increased silane concentration	***in**creased amorphous phase / **de**creased µc-Si phase*
increased pressure	***in**creased amorphous phase / **de**creased µc-Si phase*
increased total gas flow	***in**creased amorphous phase / **de**creased µc-Si phase*
increased hf-power	***de**creased amorphous phase / **in**creased µc-Si phase*
increased temperature	***de**creased amorphous phase / **in**creased µc-Si phase*
increased excitation frequency	***de**creased amorphous phase / **in**creased µc-Si phase*

Tab. 2.1: Dependence of the amount of amorphous or crystalline phase on the deposition parameters [2.2].

A high silane concentration, pressure or total gas flow leads to a shift of the growth conditions to a region where the amorphous phase prevails. For higher temperatures, high frequency power and increasing excitation frequencies the silicon film grows with a more crystalline volume fraction [2.2]. The excitation frequency used in the PECVD system is 13.56 MHz. For a deposition on low cost window glass the maximum process temperature is limited to ~200°C.

In other CVD reaction concepts even higher deposition temperatures generally enhance the crystallinity and electronical quality of the deposited silicon layer in addition to a significantly higher growth rate that can be as high as 10 µm/min (for deposition temperature T > 1000°C). For such high deposition temperatures a foreign substrate like pre-ribbons [2.3] or scrap silicon wafers that have been used in the microelectronic industry before are the alternative to glass substrates. The deposition speed of the low temperature PECVD concept that has a sufficient electronic quality is below or in the range of 1 nm/sec [2.4]. To reach a high throughput of the machines a high deposition rate is economically advantageous. The doping of the p- and n- layer is usually done by adding a doping gas to the PECVD process gases. Further information about the deposition of thin-film silicon by PECVD can be found elsewhere [2.5].

2.3 Zinc oxide - A transparent and conductive oxide

In the investigated solar cell concept a magnetron-sputtered aluminium-doped zinc oxide ZnO:Al film is used as a transparent and conductive front contact. The ZnO films exhibits high conductivity and transparency.

A post deposition etching step in diluted hydrochloric acid (HCl) leads to a surface topography that introduces a simple way to integrate a nano/microstructure for an enhanced light trapping in the silicon thin-film solar cell.

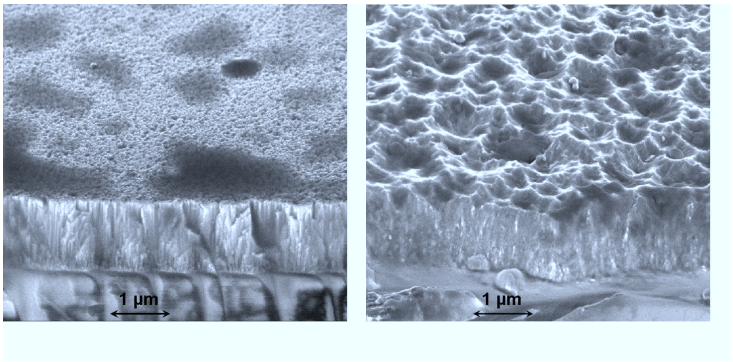

Fig. 2.3: High-resolution scanning electron microscope (HRSEM) cross section of sputtered ZnO:Al films before (left), and after (right) a short dip in diluted hydrochloric acid (HCl). The acid can lead to etched craters that are up to 2 µm in diameter. Picture reprinted from Rech et al. [2.1].

In the sputter process an electrical field between two electrodes accelerates argon ions that are bombarding a target, which can be either ceramic or metallic zinc oxide. The zinc and oxygen atoms a released from the target by the physical argon ion bombardment and deposited in form of a zinc oxide (ZnO) layer on a glass substrate. The electrical and optical properties are dependent on the choice of deposition parameters. The most important parameters are: temperature, pressure, deposition power, total gas flow and gas composition. Each parameter influences the properties of the TCO layer. For example, Hüpkes et al. [2.6] and Kluth et al. [2.7] showed that the amount of oxygen added to the process gas strongly influences film properties. The amount of doping can be varied by using ZnO:Al_2O_3 targets with 0.2, 1 or 2

weight % of Al_2O_3. This is influencing the carrier concentration leading to different conductivities and free carrier absorption in the near infrared part of the sun spectrum.
The choice of process parameters can lead to different regimes of etching behaviour. A minor target doping and low heater temperature results in small and irregular features in the post etching surface topography and a “bad” light trapping is the consequence. Temperatures of T ~ 200°C and target doping levels of ~ 2 *wt* % (weight percent) lead to more regular crater formation with opening angles between 120° and 135° and lateral feature sizes of 1 – 3 µm. This improves the light scattering properties [2.8].
The sensitivity of the post-etching morphology of sputtered TCO to the individual sputter parameters is a critical aspect in the development and optimization of thin-film silicon solar cells. For instance, a change of the sputter target, the gas sources, fluctuating temperature process profiles or a continuously increasing thickness of a parasitic deposited layer inside the chamber can lead to a change of the morphology of the post-etching structure. A permanent fine-tuning of many process parameters needs to be avoided in industrial concepts.
Therefore, a controllable nano/microstructure that is not directly depending on the TCO deposition itself is from this point of view in the long term of thin-film silicon solar cell development, also favourable.

2.4 Back contact silver layer

Thermal evaporation is like sputtering a physical vapour deposition (PVD) technique. It allows depositing thin layers of different metals like silver (Ag) or aluminium (Al) as the back contact of the thin-film solar cell. A vapour is thermally created, transported to the substrate (solar cell) and then the vapour condenses and a thin metal layer is formed. It is the electrical back contact of the solar cell and in addition the optical back side reflector that is important for the trapping of light with long wavelength inside the solar cell. The deposited Ag and Al layers are compact, homogenous and show a good adhesion to ZnO and a lower adhesion to silicon. Their ductility can reduce physical stresses within the layers and compensate stresses introduced by thermal expansion.

The introduction of losses due to plasmonic effects at the nano-structured or almost flat metal thin-film back reflector is considered to lead to losses up to 15 % for specific frequencies [2.9].

2.5 Up-scaling of thin-film deposition techniques

The deposition of the thin-film layers (TCO, silicon and metals) and processing of thin-film silicon solar cells has been demonstrated over the years by the leading research institutes and several companies world wide. The current demand for solar energy has made former TFT (thin-film transistor) equipment manufacturers to move to the thin-film silicon solar cell technology. They provide a broad knowledge in up-scaling of deposition technologies that allows the handling and deposition of uniform thin-films similar to the above described layers on glass substrates or other flexible substrates like metal foil up to an area of 5.7 m^2 (status 2009) and even 8.7 m^2 is in planning for the year 2010. [2.10]

This up-scaling of the deposition techniques for thin-film solar cells is the key to the "economies of scale" that are necessary to lower the production costs of solar energy.

References Chapter 2

[2.1] B. Rech, H. Wagner Appl. Phys. A 69, 155–167 (1999)

[2.2] L. Houben, O. Vetterl , Sol. Energ. Mat. Sol. Cells 62 (2000)

[2.3] Faller et al., Mc-Si thin film solar cells by fast CVD on low cost SSP pre-ribbons, Institute of Electrical and Electronics Engineers IEEE, 25th IEEE Photovoltaic Specialists Conference 1996. Proceedings 1996

[2.4] T. Repmann. Stapelsolarzellen aus amorphem und mikrokristallinem Silizium. PhD thesis, RWTH Aachen, 2003

[2.5] T. Kilper, Großflächige Plasmaabscheidung von mikrokristallinem Silizium für mikromorphe Dünnschichtsolarmodule, Fakultät für Elektrotechnik und Informationstechnik der Technischen Universität Carolo-Wilhelmina zu Braunschweig, Dissertation, 2008

[2.6] J. Hüpkes, B. Rech, S. Calnan, O. Kluth, U. Zastrow, H. Siekmann, and M. Wuttig, Thin Solid Films 502, 286, 2006

[2.7] O. Kluth, G. Schöpe, B. Rech, R. Menner, M. Oertel, K. Orgassa, and H. W. Schock, Thin Solid Films 502, 311, 2006

[2.8] M. Berginski, Jürgen Hüpkes, Melanie Schulte, Gunnar Schöpe, Helmut Stiebig, and Bernd Rech, JOURNAL OF APPLIED PHYSICS 101, 074903, 2007

[2.9] R. Collins, presentation at 33rd IEEE photovoltaic specialist conference, San Diego, 2008, paper in print

[2.10] Sharp corporation, website

3 Limitation of photo generation in thin-film solar cells

3.1 The Yablonovitch limit

The absorptance of a layer is usually increasing when the amount of light that is reflected at the interface is reduced. Also, an enhancement of the path length inside the absorber layer increases the absorptance. Consequently, two simple approaches to increase the absorptance of a solar cell are the integration of antireflective properties into the cell design and a large absorber layer thickness.

If the photons that are incident on the cell are reflected but redirected on the cell again then another chance to enter into the solar cell occurs. This can be reached with a pyramid-like structure on top of the solar cell.

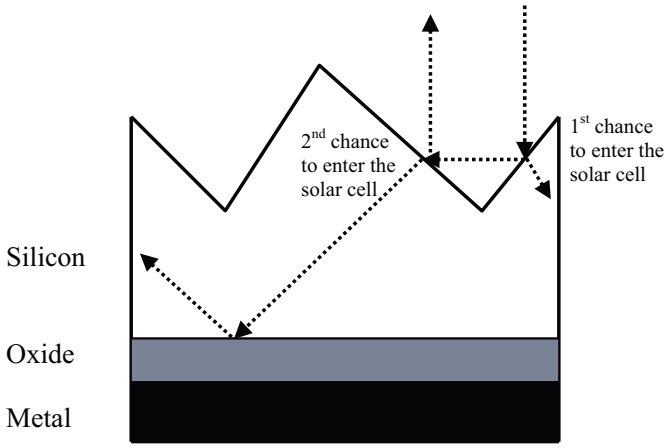

Fig. 3.1: The surface reflectance of a flat interface is significantly reduced by the integration of a pyramid texture as a second chance for the incident light to enter into the absorber layer is possible.

The total reflectance (r) is significantly reduced by a second chance to enter the cell.

$$r_{total} = r^{2}_{single} \tag{3.1}$$

A surface with 10 % reflectance for flat interfaces has with a pyramid texture a reduced reflectance of only 1 %. This is, of course, a simplifications as the reflection of a surface is angular dependent with α being the angle of light incidence $r = r(\alpha)$.

In addition to the reduced reflectance the light is diffracted at the pyramid like surface and the light path strongly deviates from the normal transition through the absorber, i.e. the light path is prolonged. To enable a light trapping effect a highly reflective back reflector is needed. A combination of a metal and oxide layer is possible. Very important is that after the reflection at the back reflector the light is incident on the front interface in an angle that supports total internal reflection.

The angle of total internal reflection α_t is given by:

$$\sin \alpha_t = \frac{1}{n_{Si}} \tag{3.2}$$

with $n_{Si} \sim 3.6$ ($\lambda = 1000$ nm) as the refractive index of silicon. Only photons are not internally reflected that are incident under an angle $\alpha_t < 16.6°$.

The prolongation of the average light path has been estimated by Yablonovitch et al. [3.1] under the assumption that the combination of a structured surface and a highly reflective back reflector leads to an isotropic distribution of photons inside of the solar cell. The structured surface scatters the photons with an angular distribution that is comparable to the distribution given by a black, Lambertian surface that emits photons. A Lambertian surface, by definition, fully randomizes reflected and transmitted light for all wavelengths [3.2]. For this angular distribution the photons that are leaving without total internal reflection ($\alpha_t < 16.6°$) from the absorber layer through the front interface are redistributed over an effective solid angle of π. This is common for the emission of radiation from a surface (Stefan-Boltzmann law of radiation). The isotropic distribution inside the absorber layer fills the angle 4π which is twice the half space of 2π from the top and bottom interface. Inside the absorber layer the photon flux density per angular element $j(\Omega)$ is a factor of $(n_{Si})^2$ larger than outside of the solar cell. [3.2]

For a thickness L of a weakly absorbing material, here, the silicon layer, the absorbed photon flux I_{abs} is determined by the flux that is entering into the surface A of the cell after a reflection (1-r) I_{in} and the photon flux that is escaping through the surface I_{esc}. A prerequisite for these assumptions is the ideal reflection of all photons at the back side of the solar cell and neglecting of an emission of photons within the absorber layer [3.1]

$$(1-r)\cdot I_{in} = I_{esc} + I_{abs} \tag{3.3}$$

For the assumed isotropic and homogenous distribution of photons with the photon flux density per angular element $j(\Omega)$ the per volume $V = L \cdot A$ absorbed photon flux is

$$I_{abs} = 4\pi \cdot a \cdot V \cdot j(\Omega) \tag{3.4}$$

With a as the absorption coefficient.

This leads to

$$(1-r)Aj(\Omega)_{in} = Aj(\Omega)_{esc} + 4\pi \cdot aVj(\Omega) \tag{3.5}$$

$$(1-r)\,j(\Omega)_{in} = (1-r)\pi(n_{Si})^2\, j(\Omega) + 4\pi \cdot aLj(\Omega) \tag{3.6}$$

The optical absorption A^{opt} of a cell can be calculated by definition:

$$\mathrm{A}^{opt} = (1-r)4\pi \cdot aL/((1-r)\pi/(n_{Si})^2 + 4\pi \cdot aL) \tag{3.7}$$

$$\mathrm{A}^{opt} = I_{abs}/I_{in} = (1-r)I_{abs}/(I_{esc} + I_{abs}) \tag{3.8}$$

$$\mathrm{A}^{opt} = (1-r)/((1-r)/4n_{Si}{}^2 aL + 1)) \tag{3.9}$$

For small absorption coefficients a the **optical absorption $\mathbf{A}^{opt}$** of a solar cell is

$$\mathrm{A}^{opt} = 4 \cdot n_{Si}{}^2 a \cdot L \tag{3.10}$$

It is for a not too large reflectivity independent of r [3.2].

For silicon the optical absorption A^{opt} is a factor 4 $n_{Si}^2 \sim 50$ larger than the absorption without a light trapping scheme.
In comparison to a normal transition through the absorber ***the average light path is thus enhanced by a factor of 50.***

Although the above derivation is only valid for a homogenous distribution of photons, that is only realized for $a < 1/L$, it is also valid for large a as for $a < 1/L$ the saturation value $a = (1-r)$ is reached which is not exceeded even for large a.

The Yablonovitch model has been modified by Deckman et al. [3.3] to a less idealized system. In their model they consider the parasitic absorption in the front and back contact ($Abs_{front,}$ Abs_{back}). Like in the Yablonovitch model the randomization of the light path in the device is Lambertian, i.e. totally diffuse.
Deckman et al. derive with an infinite geometric expression that for a silicon layer with thickness L, refractive index n_{Si}, absorption coefficient a, the theoretical absorption probability $A_{Deckman}$ is:

$$A_{Deckman} = (1-(Abs_{front} + Abs_{back}) \cdot \exp(-2aL) - (1 - Abs_{front} - Abs_{back}) \cdot \exp(-4aL)) \cdot (1-(1 - Abs_{front} - Abs_{back}) \cdot \exp(-4aL) + (1 - Abs_{front} - Abs_{back}) \cdot \exp(-4aL) \cdot n_{Si}^{-2})^{-1} \quad (3.11)$$

For the parasitic absorption in the front and back contact of p-i-n thin-film silicon solar cells additional absorption in the doped layers needs to be taken into account:

$$Abs_{front} = Abs_{front-TCO} + Abs_{p-doped-silicon} \quad (3.12)$$

$$Abs_{back} = (1 - Abs_{back-TCO/Silver}) + Abs_{n-doped-silicon} \quad (3.13)$$

To derive a limit for the quantum efficiency Deckman et al. assume that all occurring absorption processes in the silicon layer lead to a generation of electron-hole pairs. To account for the losses that are present until the photons reach the intrinsic silicon absorber layer the model considers the reflection losses R_{front} and absorption losses Abs_{front} for a single pass through the front contact.

The limit for the quantum efficiency based on the theoretical absorption probability $A_{Deckman}$ under consideration of parasitic losses is:

$$QE_{Deckman} = Abs_{Deckman} \cdot (1 - R_{front}) \cdot (1 - Abs_{front-TCO}) \cdot (1 - Abs_{p-doped-silicon}) \tag{3.14}$$

In the studies of Springer et al. [3.4] a limit estimation for quantum efficiencies of a thin-film silicon solar cell is presented that is based on a semi-empirical Monte-Carlo simulation and a wave theory approach. Light scattering is also expected to be Lambertian. The scattering for the individual surfaces and the measured absorption of each layer are considered. For a large quantity of photons the individual path until absorption is calculated that gives spatial information about the localization of losses. Springer et al. found that for a µc-Si:H solar cell with a thickness of 1.2 µm the front contact losses are the dominant effect for the red and infrared spectrum. They make up to 70 % of the total losses and are thus larger than the reflection losses. The losses in the back contact layers are estimated to be below 15 % [3.4]. For the red and infrared spectrum the losses in the doped layers can be neglected.

References Chapter 3

[3.1] E. Yablonovitch, Journal Optical American Society, 72, 899, (1982)

[3.2] Peter Würfel, Physik der Solarzellen, Spektrum Verlag, Germany, 1995

[3.3] H. Deckman, C. Wronski, H. Witzle, E. Yablonovitch, Optically enhanced amorphous silicon solar cells, Applies Physics Letters 42, 968-970 (1983)

[3.4] J. Springer, A. Poruba, M. Vanacek, Improved three-dimensional optical model for thin-film silicon solar cells, Journal of applied physics 96, 5329-5337, 2004

4 Computational modelling

Approximately every 11 years the computer technology overcomes the next technological barrier. Then the computation speed of the fastest computer in the world is increased by a factor of 1000. Today's super-computer consists of up to 20.000 multi-core processors.
For the simulations conducted in this study two quad-core processors with 2.66 GHz each and 8 GB Ram are used. The calculation speed limiting factor of the FIT technique is the size of the processor memory, the "Cache". It handles the large matrixes generated in the calculation.
Previous simulation studies of solar cell optics and light trapping have been performed with the ray tracing technique [1.3; 4.1-2].

4.1 Optical simulations - Coherent or incoherent?

A simulation does only reproduce interference fringes for the calculated transmittance, reflectance or absorption spectra, if the phase of the electromagnetic radiation is considered [4.3]. The experimental *EQE* measurements also show interference fringes. For untextured, flat layers they are of stronger nature than for textured layer systems. Generally, the experimental setup smoothes the interference fringes, as the optical resolution is in the range of 15 nm, only. Usually the coherent method oscillates around the incoherent values and the integrated current density values J_{sc} differs only by 0.5 %.
For the broad band solar spectrum the coherence length is sufficiently small with ~1 µm [4.4], that all interference effects are averaging out when calculating the current densities J_{sc}. Considering the years average illumination and for film thicknesses down to d = 0.5µm the difference between coherent and incoherent simulations is around 1 %. [1.3]
But geometrical ray-tracing is not applicable if the texture period is similar in size to the wavelength as present in this study of µc-Si thin-film solar cells.
It is proposed by Brendel [1.3] that for the simulation of the optical response incoherent simulations are a valid technique down to a period size of 2 µm. A quantitative comparison of an exact coupled wave theory or an approximate incoherent ray-tracing has so far not been conducted.

4.2 Near field - far field optics

The existence of electro-magnetic far field and near field components for a precise description of the radiation of antenna is well known. For the description of the electrical field of an antenna with distance r_d from the source of the antenna using spherical coordinates gives:

$$\vec{E}(\varphi) \propto \frac{2\pi \cdot Z_o \cdot I \cdot dl \cdot \cos\varphi}{\lambda} \cdot \left(-\left(\frac{\lambda}{2\pi \cdot r_d} \right)^3 \cos\omega - \left(\frac{\lambda}{2\pi \cdot r_d} \right)^2 \sin\omega + \left(\frac{\lambda}{2\pi \cdot r_d} \right)^1 \cos\omega \right) \quad (4.1)$$

with *dl* the length of the antenna element, *I* the current in the element, $\omega = (2\pi f / \lambda) - wt$ with w the radian frequency, r_d the distance from the element to the point of observation, φ the zenith angle to the radial distance r_d, λ the signal wavelength and Z_o the vacuum impedance [4.5-6]. Three terms are found. The inverse distance term proportional to r_d^{-1} is called the radiation term. It represents the energy flow away from the wire. The square distance term proportional to r_d^{-2} is the induction term. This contribution represents the energy stored in the field during one quarter of the cycle and then returned to the antenna in the next. The inverse cube distance term proportional to r_d^{-3} is the quasi-stationary term or the electrostatic field term that results from the accumulation of charge at the ends of the antenna element.

The fields of an antenna in a homogeneous isotropic medium, like air, can be mathematically expressed by a multipole expansion [4.8]. This expansion is composed of spherical harmonics describing the angular dependence and spherical Bessel functions describing the radial dependence. In the near field of this antenna the multipole expansion is no longer useful as too many terms would be required for a precise description of the fields. For radio antenna the operating distance is usually a multiple of the transmitted wavelength.

In an inhomogeneous media / material the multipole expansion is no longer valid and the full solution of the Maxwell's equations is generally required as it describes the radiating fields and evanescent fields more adequate. For thin film silicon solar cells the multi layer device is in the range of a few μm and the contribution of the optical near field terms is necessary. Because the near-field light decays exponentially within a distance less than the wavelength of the light and consists of non propagating fields, only, it usually travels undetected when investigations in the far distance are carried out, like the optical far field characterisation of scattering rough TCO surfaces. [4.9]

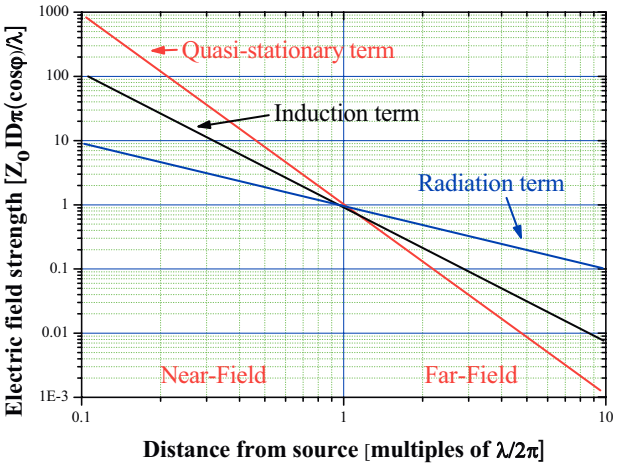

Fig. 4.1: The electrical field of an antenna depending on the distance from the source is shown. The radiation term represents the energy flow away from the wire. The induction term represents the energy stored in the fields. The quasi-stationary term results from the accumulation of charge at the ends of the antenna element. The separation into near field and far field is shown [4.7].

For the investigation of crystalline silicon solar cells a far field investigation can be sufficient as the absorber layer thickness is around 200 µm and thus much larger than a multiple of the incident wavelength. For this case, a ray tracing method can give enough information for the understanding of light trapping.

In quantum mechanical terms, the far field exists due to the propagation of classical photons. The near field, seen in quantum terms, can be ideally imagined as “virtual photons” that have an evanescent existence.

The near field has with respect to different telecommunication technologies three main characteristics:

1. The near field is that part of the radiated field that lies within a few wavelength of the diffracting edge or radiating antenna.
2. It is the near-by region of an antenna where the angular field distribution is dependent on the distance from the antenna.
3. For optical applications, for example, fibres, it is the region close to the light source or the aperture.

Generally, light in the near-field carries more high-frequency information and has its greatest amplitude in the region within the first few tens of nanometres of the specimen surface depending on the diffractive nature of the specimen.
Consequently, as the light propagates away from a surface or interface into the far-field region, the highest-frequency spatial information is filtered out, and the well known diffraction-based Abbe limit on resolution is imposed. In the late 19^{th} century this diffraction limit of spatial resolution was proposed by Ernst Abbe and Lord Raleigh. This law states that using light waves for optical microscopy is limited to spatially resolve details that are below approximately half of the probing wavelength. Thus, for the visible spectrum the limit is around 250 nm. In 1928 Edward Hutchinson Synge proposed the concept of the near-field microscopy. The Scanning Near-Field Optical Microscopy (SNOM) realizes his proposal. It brings a small optical probe very close, i.e. in the near-field of the sample surface. At distances smaller than the wavelength away from the surface the previously described, non propagating evanescent modes can be detected. The k-vectors parallel to the surface can here be very large, which corresponds to small lateral dimensions below 100 nm. The SNOM can be therefore used as a high resolution microscope to investigate the TCO morphology. In addition the electric field strength above a rough TCO can be measured for monochromatic radiation. This new measurement method has potential in the characterisation of rough TCO morphologies. Its weakness is that it allows only the investigation of structure / air (vacuum) surfaces. For thin-film silicon solar cells the near-fields inside the silicon layer are of the greatest interest. The measurement is also strongly dependent on the SNOM tip size and the tip to surface distance. Nevertheless, SNOM measurements are used for the characterisation of rough TCO textures. Strong electric fields above the TCO structure edges were detected [4.10].

For the investigation of the optical properties of thin-film silicon solar cells, or other thin-film devices, a simulation method based on Maxwell equations, like the performed FIT

simulations, seems to be ideal in comparison to other optical (far-field) characterisation methods.

Optical simulations based on the Maxwell equations have several advantages over conventional characterisation methods, as they:

1. consider the existence of *near-field* and *far field* light components
2. allow to measure *inside* of the multi-layer solar cell
3. exclude morphological, and electrical effects that can heavily influence solar cell parameters
4. exclude the scattering of data that are typical in experimental studies with a small statistical quantity
5. Maxwell simulations are widely used for more than 50 years whereas for instance SNOM is a quite "young" method

4.3 Finite Integration Technique FIT

The electromagnetism can be described with a set of four partial differential equations, i.e. the Maxwell equations. They describe the properties of the electric and magnetic fields and relate them to their sources, the charge density and current density. A precise discretization in time and space allows a complete numerical analysis.
The finite element method (FEM) is a very general solver for numerous partial differential equations. It starts with basis functions for the individual elements that are further developed by time dependent calculus of variations [4.11]. It turned out to be not the most efficient and fastest method.
The FDTD method (Finite-Difference-Time-Domain) is a very efficient solver especially for the computation of the Maxwell equations [4.12]. It uses the differential form for the discretization of the differential equations other than the Finite Integration Technique (FIT) that uses the integral form of the Maxwell equations as a discretization starting scheme [4.13].
All finite-element or FDTD like Maxwell solvers are based on the same physical principles but are using different mathematical formalism within the simulation. Depending on the investigated device and required accuracy of the result the calculation time can differ significantly.

The commercial FIT solver from the company CST® used in the presented investigations is widely used for the development of antenna, waveguide design and other high frequency applications.

4.4 Maxwell solver

The differential equations of interest for optical light matter interaction are the Maxwell equations. They contain the permeability $\boldsymbol{\mu}$ which is the degree of magnetization of a material that responds linearly to an applied magnetic field. The permittivity $\boldsymbol{\varepsilon}$ describes how an electric field affects and is affected by a dielectric medium. Thus, the permittivity relates to the material's ability to transmit electromagnetic fields. The electrical conductivity $\boldsymbol{\sigma}$ is a measure of the material's ability to conduct an electric current when an electrical potential difference forces the movable charge to flow [4.8].

Maxwell's equations are generally applied to the macroscopic averages of fields, which vary strongly on a microscopic scale in the vicinity of individual atoms where they undergo quantum mechanical effects as well.

As shown in Fig. 2.2a the morphology of a µc-Si thin-film layer is a mixture of amorphous and crystalline phase regions. The optical constants of these layers are usually characterised with a 0.5 x 0.5 cm^2 laser spot area. In the measurement this leads to a averaging effect of the optical constants of amorphous and crystalline silicon. The measured optical constants are used in the FIT simulations. The FIT software discretized the Maxwell equations on a 3D grid. The investigated device is plotted via a CAD input and the individual layers are characterized with the material parameters μ, ε and σ. The space coordinates of the device are transformed into matrix formalism and as a first step the time domain behaviour is developed with the finite-difference method. A plane wave with a fixed frequency υ is used as excitation source and the electromagnetic parameters are computed.

$$\iint_{\tilde{A}} -\frac{\partial}{\partial t}\vec{B}\cdot d\vec{\tilde{A}} = \oint_{\partial\tilde{A}} \vec{E}\cdot d\vec{r} \tag{4.2}$$

$$\oint_{\partial\tilde{V}} \oint \vec{B}\cdot d\vec{\tilde{A}} = 0 \tag{4.3}$$

$$\iint_{\tilde{A}} (\vec{J} + \frac{\partial}{\partial t}\vec{D})\cdot d\vec{\tilde{A}} = \oint_{\partial\tilde{A}} \vec{H}\cdot d\vec{\tilde{r}} \tag{4.4}$$

$$\oint_{\partial\tilde{V}} \oint \vec{D}\cdot d\vec{\tilde{A}} = \iiint_{\tilde{V}} \rho\cdot d\tilde{V} \tag{4.5}$$

The Maxwell equations in integral form are (4.2) Faraday's law of inductions, (4.3) Gauss's law for magnetism, (4.4) Ampere's Circuital Law and (4.5) Gauss's law.

$\vec{E}$ is the electrical field strength, $\vec{D}$ the electrical displacement field (also electrical flux), $\vec{H}$ the magnetic field, $\vec{B}$ the magnetic flux and $\vec{J}$ the current density. For the calculation the volume *V*, the surface area *A* and the surface edge *r* are used.

The above fields are related to each other by the material equations:

$$\vec{D} = \varepsilon_0 \varepsilon_r \vec{E} = \varepsilon_0 (1 + \chi_{el}) \vec{E} = \varepsilon_0 \vec{E} + \vec{P} \tag{4.6}$$

$$\vec{B} = \mu_0 \mu_r \vec{H} = \mu_0 (1 + \chi_{magn}) \vec{H} = \mu_0 (\vec{H} + \vec{M}) \tag{4.7}$$

$$\vec{J} = \sigma \cdot \vec{E} \tag{4.8}$$

$\vec{P}$ is the polarisation, $\vec{M}$ the magnetisation, χ_{el} and χ_{magn} the electrical and magnetical susceptibility. The electric susceptibility χ_{el} of a dielectric material is a measure of how easily it polarizes in response to an electric field. The magnetic susceptibility is the degree of magnetization of a material in response to an applied magnetic field. The Finite Integration Technique uses these material equations in discrete matrix formalism on a dual grid [4.14-16]. The device that is under investigation within the simulation is designed with a CAD program and a mesh system of small cubic cells is used. The individual size of the small mesh cells can be adapted depending of the physical problem. Either a fixed mesh number per wavelength ratio or an automatic refinement of the mesh size depending on the gradient of the optical properties can be used.

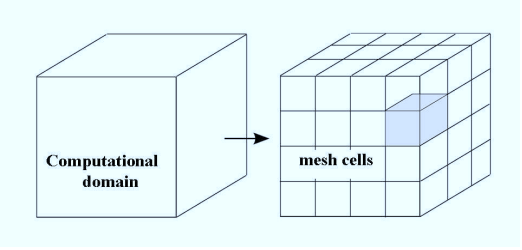

Fig. 4.1: The computational domain is divided into small meshcells. For each meshcell the Maxwell equations are solved individually. Up to 15 million small meshcells are used in our

solar cell simulations. This leads especially for small wavelength λ < 400 nm to large data files of a few Gigabyte and a simulation duration of several hours per single wavelength.

Next, the concept of the dual grid is explained with the illustration of the field components at the individual mesh cell. The red grid is characterized by the electrical field strength $\vec{e}_x$ (with *x = i, j, k, l*) at all four sides of the red square. The magnetical flux $\vec{b}$ is perpendicular to the red square. The dual grid is represented by the blue cube. It has the same lattice size but it is translated in space by half a lattice constant.

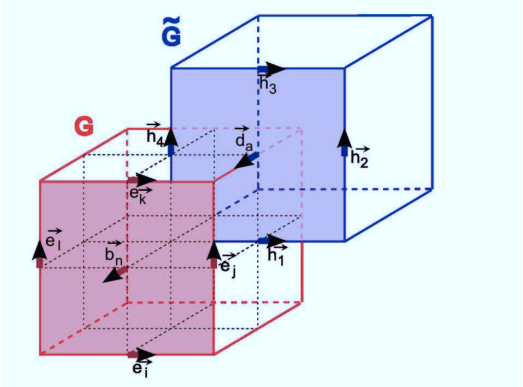

Fig. 4.2: Definition of the dual grid. Each cube is a single mesh cell within the computational domain on which the vector components of the electrical field strength $\vec{e}_x$, the magnetical flux $\vec{b}$, the electrical displacement field (flux) $\vec{d}$ and the magnetic field $\vec{h}$ are defined.

On the edges of the blue, dual grid the magnetic field vectors $\vec{h}_i$ (i = 1, 2, 3, 4) are defined and on the blue square the electrical displacement field (flux) $\vec{d}_i$ is given. For simplicity reasons only the front side vectors are illustrated. The consequence of the translation of half a lattice constant between both grids is the presence of two different field vectors at each vector-position in the graph. The fields $\vec{E}$ and $\vec{B}$ are related via the permittivity ε and the field $\vec{B}$ and $\vec{H}$ are related via the permeability μ. The discretized field components can now be calculated as a summation of the vector along the edges or through the surface. The FIT method considers all fields within a single meshcell to be constant. This is of course a strong

simplification but with a mesh resolution that is sufficiently high the error can be reduced. With Faraday's law of induction the principle can be demonstrated. The magnetical flux $\vec{b}_n$ through the red surface is related to the electrical field strength $\vec{e}_x$ around the four edges. The integral as over the single mesh cell is thus reduced to

$$-\left(\frac{\partial}{\partial t}\right)\vec{b}_n = \vec{e}_i + \vec{e}_j + \vec{e}_k + \vec{e}_l \tag{4.9}$$

To complete this calculation for all mesh cells in the grid the above equation is transformed into a matrix formalism. All components of the electrical field are represented by the vector $\vec{e}$ and for the magnetic flux $\vec{b}$ is the ensemble vector [4.13][4.15].

$$-\frac{\partial}{\partial t}\underbrace{\begin{pmatrix} \cdot \\ b_n \\ \cdot \end{pmatrix}}_{\vec{b}} = \underbrace{\begin{pmatrix} & & \cdot & \cdot & \cdot & & \\ 1 & \cdot & 1 & \cdot & -1 & \cdot & -1 \\ & & \cdot & \cdot & \cdot & & \end{pmatrix}}_{\overline{C}} \underbrace{\begin{pmatrix} e_i \\ \cdot \\ e_j \\ \cdot \\ e_k \\ \cdot \\ e_l \end{pmatrix}}_{\vec{e}} \tag{4.10}$$

Every line of the matrix is containing zeros, except one line in which 4 entries are either -1 or 1 depending on the orientation of the vector.

The same principle is performed for all four Maxwell equations and the 3 material equations and a set of 7 matrix equations is derived:

$$-\dot{\vec{b}} = \overline{C} \cdot \vec{e} \tag{4.11}$$

$$\overline{S}\vec{b} = 0 \tag{4.12}$$

$$\vec{i} + \dot{\vec{d}} = \overline{\overline{C}} \cdot \vec{h} \tag{4.13}$$

$$\overline{\overline{S}} \cdot \vec{d} = q \tag{4.14}$$

$$\vec{d} = \overline{D}_{\varepsilon} \cdot \vec{e} \tag{4.15}$$

$$\vec{b} = \overline{D}_{\mu} \cdot \vec{h} \tag{4.16}$$

$$\vec{i} = \overline{D}_{\kappa} \cdot \vec{e} \tag{4.17}$$

The matrix $\overline{S}$ represents the 6 field vectors which are perpendicular on the surface of each mesh cell. Its dimension is N x 3N and in each row there are three “ones” and three “minus ones”. The matrix $\widetilde{C}$ and $\widetilde{S}$ are the corresponding matrix on the dual grid. The matrixes $\overline{D}_{\varepsilon}$, $\overline{D}_{\mu}$ and $\overline{D}_{\kappa}$ are mainly unfilled, in the ideal case even diagonal. The well developed and patented formulism of the FIT method is based on the simplification to maintain the fundamental properties of the differential equations in these matrix equations. A systematic numbering of the mesh cell ensemble leads to

$$\overline{C} = \overline{\widetilde{C}}^{T} \tag{4.18}$$

$$\overline{S}\overline{C} = 0 \tag{4.19}$$

This way the equations for the differential operators can be expressed in the matrix formalism.

$$rot(grad) = 0 \leftrightarrow \overline{C}\overline{\widetilde{S}}^{T} = 0 \tag{4.20}$$

$$div(rot) = 0 \leftrightarrow \overline{S}\overline{C} = 0 \tag{4.21}$$

Weiland et al. showed that this method leads to distinct solutions without any parasitic charges. To calculate the variation in time the equations

$$-\left(\frac{\partial}{\partial t}\right)\vec{b} = \overline{C}\vec{e} \tag{4.22}$$

$$\vec{i} + \left(\frac{\partial}{\partial t}\right)\vec{d} = \overline{C}\vec{h} \tag{4.23}$$

need to be considered. A further derivation leads to a simplified matrix equation.

$$\overline{M} \cdot \bar{f} = D_m\left(\frac{\partial}{\partial t}\right)\bar{f} + \bar{s} \tag{4.24}$$

With $\bar{f}$ being a matrix that is composed of $\vec{e}$ and $\vec{h}$ vectors. The above equation contains the matrix $\bar{f}$ and its time derivative. Therefore, a discretization of $\bar{f}$ in time is necessary. This is realized by the use of finite differences.

$$\dot{\bar{f}} = \frac{\partial}{\partial t}\bar{f}^{i} = (\bar{f}^{i} - \bar{f}^{i-1})/\Delta t \tag{4.25}$$

The index i indicates the i-th time step and Δt is the time step width. With this time dependence and the previous derivations it is possible to develop a simplified recursion formula that contains the electric fields which are depending on the magnetic fields of half a time step Δt ago.

$$\vec{b}^{\,i+1} = \vec{b}^{\,i+1}(t, \vec{b}^{\,i}, \vec{e}^{\,i+1/2}) \tag{4.26}$$

$$\vec{e}^{\,i+3/2} = \vec{e}^{\,i+3/2}(t, \vec{e}^{\,i+1/2}, \vec{b}^{\,i+1}) \tag{4.27}$$

This method of recursion time-dependence is called the Leap-Frog method. It is illustrated ion the following figure.

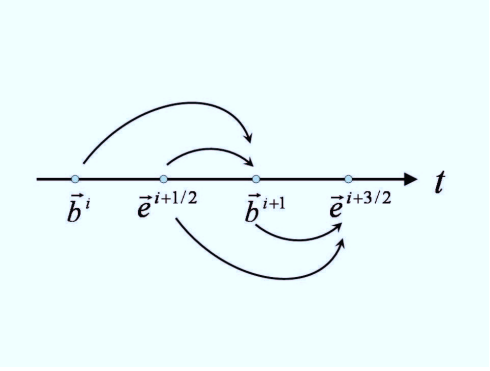

Fig. 4.3: The leap-frog scheme is a recursion method for the time development of fields (in our case the electromagnetic fields) that results in a numerical simplification.

It seems easily understandable that the time step Δt is very important for the convergence of the solution for the calculated fields. The time step itself is correlated to the mesh size via the Courant-Friedrich-Levy condition [4.17-8]:

$$\Delta t \leq (c_0(\varepsilon\mu)^{-1/2}((1/\Delta x^2) + (1/\Delta y^2) + (1/\Delta z^2))^{1/2})^{-1} \tag{4.28}$$

This relation between meshcell size (Δx, Δy, Δz) and the time step Δt has to be satisfied everywhere in the unit cell to reach a convergence of the calculation.

The FIT simulation uses a plane wave as incoming radiation source. The field vectors of the electric and magnetic field can be chosen to oscillate harmonically in time. The frequency and the polarisation of the field oscillation can be selected.

The plane wave is incident on the simulation unit cell for only a very short time. The pulse duration is about 4 femto seconds long. In this time the field energy is stored in the electromagnetic fields of the whole system due to the incoming plane wave. Then the pulse stops and the waves are propagating within the calculation domain until the energy decay reaches - 30 dB. This is the so called steady state criterion. During the entire time until the steady state is reached the fields are recorded [4.19]. From these fields it is then possible to calculate parameters like the power loss density that is used in the investigation. The higher the energy decay for the steady state criterion is chosen the more precise the result will be. In case of a weakly absorbing material, like silicon for $\lambda > 1000$ nm, the wave propagates many times within the cell until this steady state is reached. For large unit cells and special parameter combinations the decay limit needs to be readjusted to -20 dB to satisfy the steady state criterion.

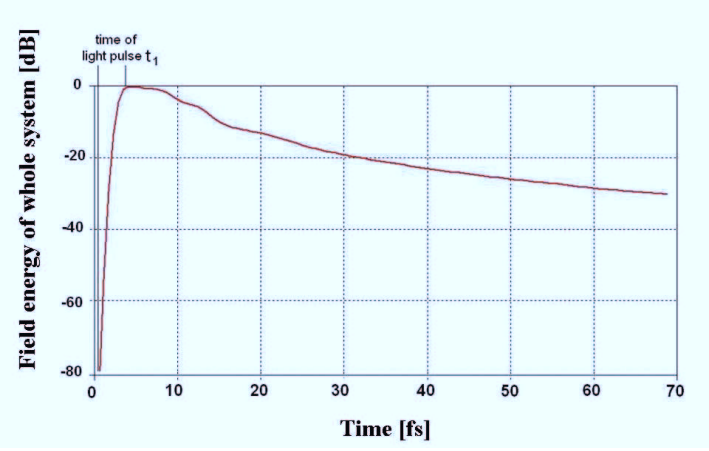

Fig. 4.4: The field energy in the computation domain is strongly increasing when the light pulse is incident during the first 4 femto seconds. Then the pulse is stopped and wave propagates within the solar cell until the field energy is decay by 30 dB, i.e. the light is absorbed.

References Chapter 4

[4.1] P. Campbell, Light-Trapping and Reflection Control in a Crystalline Silicon Solar Cell. In: Ph.D. Thesis, University of New South Wales, Sydney (1989).
[4.2] G. H. Spencer and M. V. R.K. Murty (1962), "General ray tracing Procedure". J. Opt. Soc. Am. **52** (6): 672–678.
[4.3] Harbecke, B., Coherent or incoherent reflection and transmission of multilayer structures, Appl. Phys. B, 39, 165, 1986
[4.4] A. Donges, The coherence length of black-body radiation 1998 Eur. J. Phys. **19** 245-249
[4.5] N. Ida, J.P. Bastos, ”Electromagnetics and Calculation of Fields”, Springer ; second edition 1997.
[4.6] C.G. Someda,”Electromagnetic Waves”, Chapman & Hall; 1st edition 1998.
[4.7] J. Johansson, U. Lundgren, Master Thesis, Sweden, EMC of Telecommunication
[4.8] J. D. Jackson, Classical Electrodynamics, 3rd edition Wiley, New York, 1998
[4.9] J. Springer, A. Poruba, and M. Vanecek, J. Appl. Phys. **96**, 5329, 2004
[4.10] K. Bittkau, R. Carius, C. Lienau, Phys. Rev. B **76**, 035330, 2007
[4.11] J. Volakis, A. Chatterjee, L. Kempel, Review of the finite-element method for three-dimensional electromagnetic scattering, Journal of Optical Society America, A11, 1422-1433, 1994
[4.12] A. Tavlove, Hagness S., Computational Electrodynamics, The finite difference time domain method, Artech Hous
[4.13] T. Weiland, "A discretization method for the solution of Maxwell's equations for six-component Fields", Electronics and Communications AEUE, vol. 31, no. 3, pp. 116-120, 1977e, 2005
[4.14] T. Weiland, On the unique numerical solution of Maxwellian eigenvalues problems in three dimensions, Particle Accelerators 17, 227-242, 1985
[4.15] T. Weiland, Time domain electromagnetic field computation with finite difference method, International journal of numerical modelling 9, 295-319, 1996
[4.16] K. Yee Numerical solution of initial boundary value problems involving Maxwell’s equations in isotropic media, IEEE: transactions on antennas and propagation, AP-14, 302-307, 1966
[4.17] R. Courant, K. Friedrichs, H. Lewy, Über die partiellen Differenzengleichungen der mathematischen Physik, Mathematische Annalen, vol. 100, no. 1, p. 32–74, 1928.

[4.18] R. Courant, K. Friedrichs, H. Lewy, "On the partial difference equations of mathematical physics", IBM Journal, March 1967, pp. 215-234
[4.19] CST, Microwave Studio Suite 2008, Darmstadt, Germany

5 FIT simulations of thin-film silicon solar cells with 1D grating coupler

5.1 Grating coupler (1D) for light trapping in thin-film silicon solar cells

As an alternative to solar cells deposited on randomly textured substrates the integration of periodically textured grating couplers in thin-film solar cells was proposed by several studies [5.1-3].
The 1D line grating is a very simple structure. The various degrees of freedom that would be necessary for the parameterization of a random interface are thus reduced significantly.

A sketch of a solar cell with integrated grating coupler is shown in Fig. 5.1. It consists of a periodically textured zinc oxide (ZnO) front contact, a 1 µm thick microcrystalline silicon absorber layer, and a ZnO/metal back contact.
The transmission grating leads to a diffraction of the light. The diffraction angle in transmission and reflection is given by the following equation:

$$\sin(\Theta_m) = \frac{m \cdot \lambda}{P \cdot n} \tag{5.1}$$

For normal incidence m is the diffraction order, P the period size and λ the vacuum wavelength. n denotes the refractive index of the material in which the transmitted, diffracted light propagates. Both concepts – application of randomly and periodically textured substrates - focus on a diffraction of the incoming light and a prolonging of the light path within the cell.

The red part of the sun spectrum has to be particularly addressed to achieve an effective light trapping as the absorption probability for red light in µc-Si:H or a-Si:H is much lower than for blue light. Since the question of the perfect design of a thin-film silicon solar cell for effective light trapping still remains open, the investigation of a one-dimensional (1D) grating structure shall give more insight into the diffractive properties of textured surfaces [5.1][5.4].

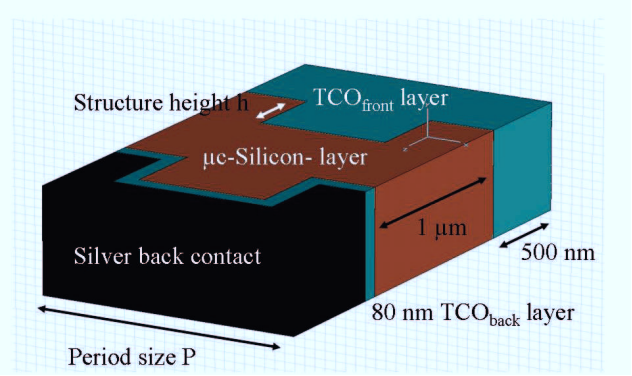

Fig. 5.1: Scheme of thin-film silicon solar cell with integrated grating coupler.

Therefore, three-dimensional (3D) optical simulations of thin-film silicon solar cells with periodically textured substrates were carried out using CST Microwave Studio® . This allows for the investigation of the optical properties of such a device in detail and provides a study independent from electrical and morphological influences.

To prove the simulations they are compared with experimental results of a 1D grating prototype texture to obtain more insight into the light propagation in a multi-layer device.

The 1D grating couplers are defined by their period size P, the groove height (or structure height) h_g, the groove length (G) to period ratio G/P, the shape of the grating and the filling factor. In this investigation we have concentrated on grating coupler with P between 1 and 4 µm because the randomly textured ZnO, on which the highest efficiency of microcrystalline silicon solar cells are prepared [5.5], has mainly a lateral structure size between 1 µm and 2 µm [5.6]. The investigation of the 1D line grating coupler is divided in three parts:
Firstly, the variations of grating parameters P and h_g under monochromatic illumination conditions are discussed. Secondly, the influence of the grating parameters with a focus on the red light that has to be trapped more effectively will be presented and the simulation results are compared with experimental data. In the third section we change the shape of the 1D-grating from binary to triangular (blazed grating) in order to discuss the effect of enhanced light in-coupling.

The unit cell of the calculated 1D grating structure is in agreement with Fig. 5.1. The model assumes periodic boundary conditions for the calculation unit cell. The glass substrate that is present in reality is not integrated in our simulations as it has no significant influence on the light diffraction and would make the simulations more time and memory consuming. A unit cell with a substrate glass layer would lead to a slightly higher light incoupling as it has an additional AR effect as the refractive index of glass lies in between the refractive index of air and ZnO. The textured ZnO front contact consists of a 500 nm thick layer and ZnO strips with different groove heights. The back side ZnO layer has a thickness of 80 nm. The optical properties of µc-Si:H and the transparent conductive oxide (ZnO) are described by their optical constants $n(\lambda)$ and $k(\lambda)$ and can be found in numerous publications of our institute that have led to a successful description of layers [5.8], sensors [5.9] and solar cells [5.10] based on amorphous and microcrystalline silicon thin-films. For simplicity the silver back contact is calculated as a homogenous flat lossy metal because (i) the optical properties of the evaporated silver at the ZnO/metal interface are unknown and differ significantly from the silver-"bulk" material [5.10] and (ii) speed-up of the very time-consuming calculations. Reference [5.10] reports about the growth of evaporated back contact silver layers with a formation of "island"-like silver shapes within the layer.

The incoming light wave is circular polarised with normal incidence. For data analysis the 3D local and integral power loss profile (see Ref. 5.11) of each layer was calculated.

5.2 Monochromatic quantum efficiency of µc-Si:H solar cells with integrated grating

Firstly, we have investigated the influence of the grating parameters period P and groove height h_g, on the optical properties of µc-Si:H diodes with an i-layer thickness of 1 µm. The study of the wave propagation in thin-film devices was performed in order to find the optimised structure sizes for efficient light trapping. The incorporation of a 1D grating into a solar cell requires at least a two dimensional analysis of the wave propagation within the cell due to diffraction of the light at the textured interfaces. To demonstrate the effect of light diffraction in thin-film silicon p-i-n diodes the calculated power loss profiles for circular polarized monochromatic illumination (λ = 800 nm) are plotted for different groove heights h_g, (see Figure 5.2).

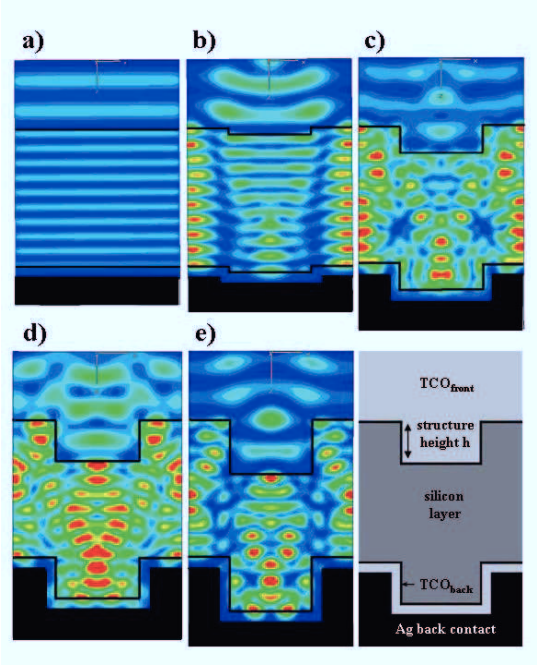

Fig. 5.2: Power loss profiles for different groove heights h under monochromatic illumination (λ = 800 nm). The calculated QE values are for case a) h_g=0.001µm, QE= 0.08, b) h_g = 0.05 µm, QE = 0.16, d) h_g = 0.3 µm, QE = 0.3, e) h_g = 0.4 µm, QE = 0.2. The constant period size is P = 1.2 µm. The calculation unit cell scheme of a solar cell with grating structure is shown in the lower right corner.

All calculations were performed for normal incidence. The period of the grating was fixed at 1.2 µm. In case of a quasi flat cell (h_g = 1 nm) alternating maxima and minima within the generated power loss profile can be observed. This pattern occurs due to constructive or destructive interference of light waves propagating in direction of the back contact and light waves that have already been reflected at the back contact. Cells with integrated grating couplers show perpendicular to the direction of light incidence a laterally inhomogeneous pattern within *P*. For a small groove height of only 50 nm a spatial change in the loss profile can be observed (Fig. 5.2b). This change of pattern is different for each groove height.

Maxima of the absorption exist especially in the groove region. Based on the simulated power loss profiles the external quantum efficiency *EQE* for a wavelength of 800 nm was calculated. The *EQE* of the silicon layer is defined as

$$EQE = Power_{absorbed} / Power_{incident} \tag{5.2}$$

It is assumed that each photon absorbed in the silicon layer generates an electron – hole pair which contributes to the photocurrent. In general, cells with an integrated grating have an increased *EQE* for every groove height h_g compared to a flat cell (for λ = 800 nm: for a flat cell *EQE* = 0.08, cell with grating: 0.08 < *EQE* < 0.37) due to increased absorption within the i-layer. The increase of the absorption in the silicon layer with increasing h_g originates from a more efficient diffraction of the incident light and an improved light in-coupling.

The variation in *EQE* with h_g consists of a superposition of the TCO front layer thickness variation and a change in the diffractive nature. Fig. 5.3 shows the calculated QE for monochromatic illumination conditions with blue (400 nm) and near infrared light (800 nm) as a function of h_g (closed and open stars). Additionally, the *EQE* of a flat cell with a thickness of the TCO front contact varying between 500 nm and 1900 nm is plotted. To have comparable device structures the initial TCO layer thickness was chosen to 500nm (see Fig. 5.3) and for the flat structure the x-axis represents the increase of the TCO front contact from 500 nm (h = 0) to 1.9 µm (h = 1.4 µm). In general, the simulated *EQE* of the flat structure decreases with increasing TCO front-layer thickness. This can be attributed to higher absorption losses in a thicker front TCO. This is valid for blue and for red illumination. For blue illumination, both the TCO front layer thickness variation and the groove height variation show a comparable behaviour. The calculated *QE* for 400 nm wavelength of a flat structure oscillates due to an interference of the light striking at the solar cell and light that has been reflected at the TCO/silicon interface. For a TCO layer thickness of an odd multiple of $\lambda/(4n_{TCO})$ the TCO layer acts as an anti-reflection coating and the reflection of the solar cell shows a minimum. Consequently, the monochromatic *QE* exhibits a maximum.

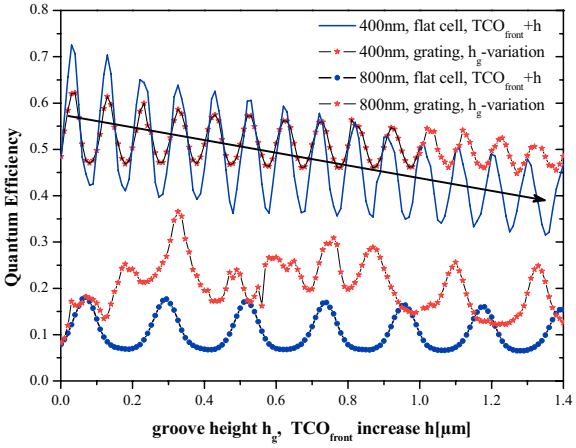

Fig. 5.3: Variation of front TCO layer thickness for a flat structure in comparison to a grating with a structure height shown for blue (λ = 400 nm) and red (λ = 800 nm) light illumination. The period size is constant P = 1.2 µm.

On the other hand for a TCO-layer thickness of a multiple of $\lambda/(2n_{TCO})$ the reflection of the cell has a maximum and, therefore the *QE* shows a minimum. The decrease in *QE* with increasing h_g is caused by the increase of the absorbance in the front TCO layer. With growing TCO front layer thickness the TCO volume increases and thus, the absorption is enhanced. The *QE* and absorbance of the front TCO layer have an almost opposite behaviour. The amplitude of the *QE* fringes from a structure with grating is around half of a flat structure since only 50 % of the TCO substrate is covered by grooves. With increasing groove length the amplitude rises (not shown). The average value of *QE* is very similar for small h_g and differs with increasing h_g. The deviation between the average values with increasing h_g is due to the higher absorption in the structure without gratings. In this case, the calculated monochromatic *QE* can be nearly considered as a contribution from two individual diodes: a flat structure with a constant TCO layer thickness of 500 nm and a flat structure with increasing TCO layer thickness. For a groove height h_g > 1.0 µm the silicon layer is non-continuous - as the Si-layer is only 1 µm thick - and splits up into separated absorption regions. This is now an imaginary device. Since the calculated *QE*s are very similar for both

structures the simulation demonstrates that the incorporation of the grating does not lead to significantly improved light in-coupling. This result is in good agreement with the measured reflection of solar cells based on a-Si:H and µc-Si:H with and without grating coupler [5.6][5.14]. An improved absorption due to diffraction effects is not observed as blue light is absorbed in the front part of the device and the diffraction angles are very small, e.g. the first order diffraction angle is only around 5°.

For red light (λ = 800 nm) higher monochromatic *QE* values of the cell with an integrated grating coupler in comparison to a structure without grating coupler were obtained from the calculations. For h_g = 0 nm, the optical system is mismatched, therefore a high reflection and a low *QE* is simulated. For small h_g values (h_g < 50 nm) *QE* increases for both structures mainly due to an improved light in-coupling. For higher h_g values both curves differ. For 0.05 µm ≤ h_g ≤ 0.33 µm an increased diffraction efficiency of the light leads to an increased red response.

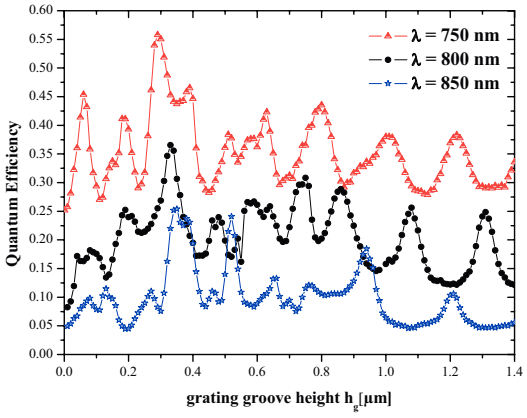

Fig. 5.4: Quantum efficiency calculation for P = 1.2 µm and a variation in the groove height. Three wavelengths are compared to exclude local standing wave effects.

The distinct maximum at h_g = 0.33 µm originates from the low reflectance - the flat structure also shows a maximum in *QE* in this region - and diffraction of the light at the

grating. For h_g > 0.33 µm the monochromatic *QE* shows a variation in the range between 0.10 - 0.3, but the *QE* is still enhanced compared to the value of a flat cell. The red response of the structure with grating exceeds the *QE* of a flat cell with a thick TCO front-layer (TCO front > 1 µm). The remaining difference in the amplitude and in the peak shift with higher h_g indicates that an explanation based on a superposition of the contribution of two individual diodes with different TCO layer thicknesses is not valid for light with longer wavelength. To exclude a local standing wave effect for this wavelength the same variation of h_g was conducted for λ = 750 nm and λ = 850 nm (Fig. 5.4).

Due to wavelength dependent optical coefficients *(n(λ), k(λ))* the *QE* values of the three curves are at different levels. A similar behaviour of the *QE* as a function of h_g was observed for the 3 investigated cases. For each wavelength a distinct maximum of the *QE* can be observed for 0.3 < h_g < 0.4 µm and it shifts to higher h_g with longer wavelength. This result demonstrates that h_g between 300 and 400 nm are necessary for an efficient light trapping in thin-film silicon cells with integrated grating coupler.

5.3 Influence of silicon layer thickness on groove height dependence of light trapping

In the following the thickness of the silicon layer was varied, since light propagation within the thin-film layer stack depends also on the individual layer thickness. The standard thickness of d(Si) = 1.0 µm was increased to d(Si) = 1.025µm, 1.05 µm and 1.075µm. Again, the groove height of the grating structure was increased in 10 nm steps to a maximum groove height of 1 µm. For illumination with monochromatic red light (λ = 800 nm) the QE was calculated for each groove height, see Fig. 5.5. For d (Si) = 1.0 µm and 1.025 µm similar curves appear with a strong increase of the QE from QE ~ 10 % to QE ~ 35 % from h = 0 to h ~ 300 nm and a pronounced peak at *h* = 300 nm. For *d (Si)* = 1.05 µm the initial *QE* value for *h* = 0 starts at an already high level of *QE* = 27 % and shows no clear increase but an oscillation of the *QE* between 12 % < *QE* < 36 % around an estimated average of *QE* = 26 %. In this case an enhanced light trapping does not compensate the reflection losses due to an optically mismatched system. For *d (Si)* = 1.075 µm the flat cell exhibits a *QE* = 22 % and reaches a maximum in *QE* = 48 % for *h* = 200 nm. For *h* > 200 nm the *QE* average slowly decreases to ~35 % which is +10 % above the average in *QE* for the other examples.

a)

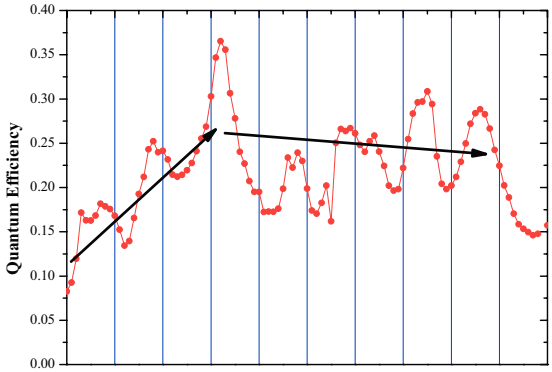
Quantum Efficiency
0.40
0.35
0.30
0.25
0.20
0.15
0.10
0.05
0.00

b)

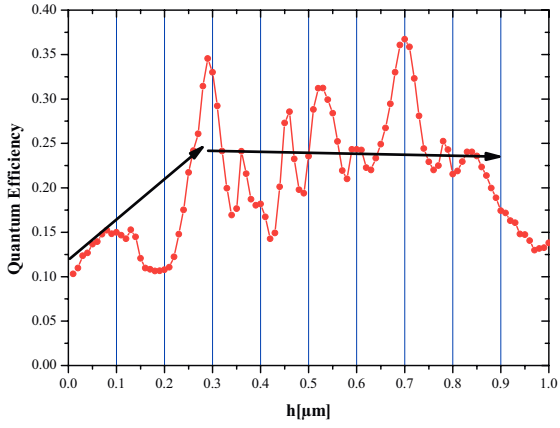
Quantum Efficiency
0.40
0.35
0.30
0.25
0.20
0.15
0.10
0.05
0.00
0.0
0.1
0.2
0.3
0.4
0.5
0.6
0.7
0.8
0.9
1.0
h[µm]

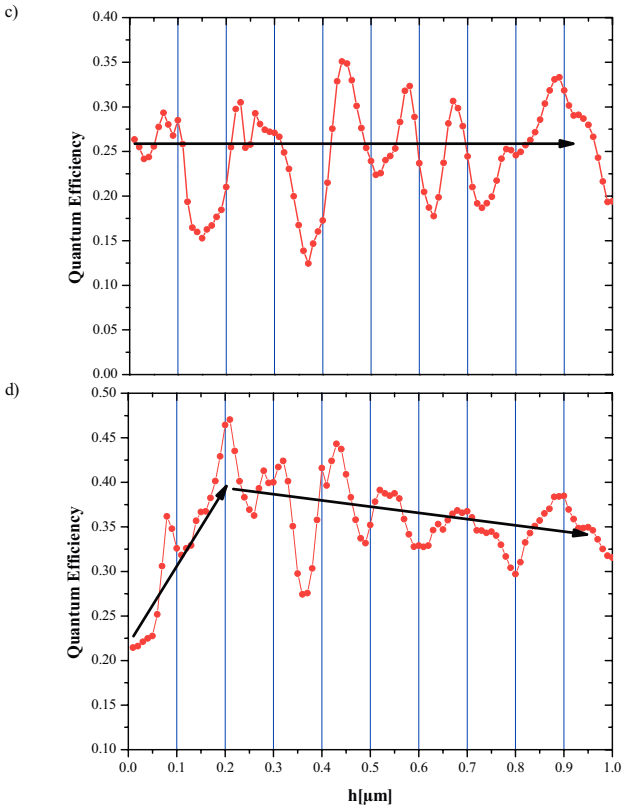

Fig. 5.5a,b,c,d: Influence of silicon layer thickness on groove height dependence for monochromatic red light (λ = 800 nm) illumination. Absorber layer thickness a) d(Si) = 1.0 µm, b) d(Si) = 1.025µm, c) d(Si) = 1.05 µm and d) d(Si) = 1.075µm were tested. Only for case c) the QE value for h = 0 starts at an already high level shows no clear increase for increasing h. The y-axis of Fig. d) starts at 0.1 and ends at 0.5 to enable a comparison with the previous Figures a) – c).

To further investigate these effects case a) and case c) are compared to a thickness variation of the untextured front TCO layer with the two different silicon layer thicknesses, see Fig. 5.6.

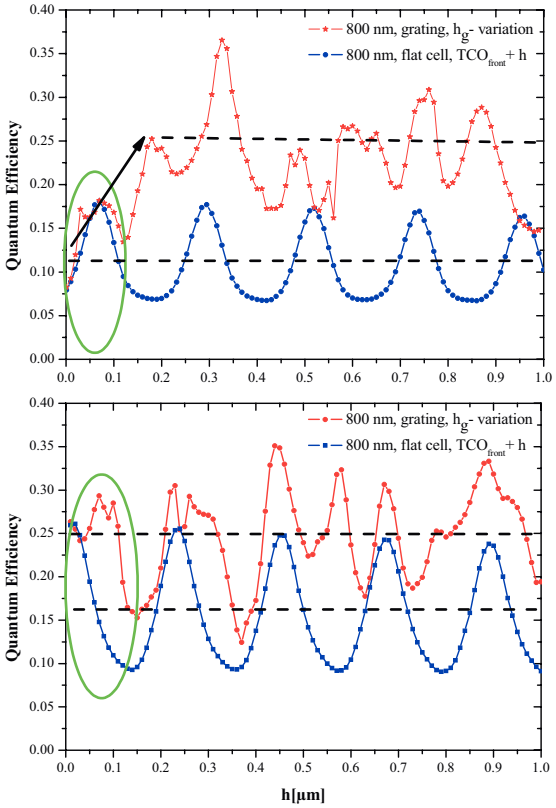

Fig. 5.6: Thickness variation of the untextured front TCO layer with the two different silicon layer thicknesses (d(Si)=1.0 µm (top), d(Si)=1.05 µm (bottom)) in comparison to a groove height dependence for monochromatic red light (λ = 800 nm).

The difference between the groove height variation and the untextured thickness variation can be attributed to the diffractive properties introduced by the grating coupler. For case a) the grating structure and the flat cell structure have almost the same *QE* values for $0 < h < 100$

nm. (indicated by the green ellipse). The blue curve shows that for h = 0 and $d(Si)$ = 1.0 µm the QE of the flat cell is in the minimum of its sinusoidal oscillation around an average value of QE = 12 %. This sinusoidal oscillation is caused by the optical matching/mismatching of the total layer-stack which is a influenced by the individual layer thicknesses and their optical constants for the incident wavelength.

In case c) a 50 nm thicker absorber layer leads to higher average values of the QE. The thickness of the front TCO, the silicon layer and the wavelength of the incoming wave determine whether an antireflection condition is satisfied and the oscillation of the QE due to a thickness variation of one of the layers of the cell is in a maximum or minimum. For h = 0 the QE oscillation in case c) is in the maximum. The difference between diffraction properties and thickness oscillation is for case c) not as pronounced as in case a). In case a) the introduction of the grating leads to an increase of the QE of + 13 %. For case c) the increase due to enhanced diffraction is only ~ 8 %. Local oscillation with a high diffraction efficiency can be found for both cases for h = 300 – 400 nm. In several cases (Case a), h = 200 nm, h = 600 nm and h = 850 nm) the grating can introduce the strongest gain in QE when the thickness of the untextured front TCO would lead to a minimum in QE. In these cases a parameter combination that would lead to a strong reflection is by the integration of a grating optically matched.

For λ = 750 nm the average in QE of the TCO front thickness variation and the grating structure variation is roughly the same (Fig. 5.7). The light trapping effect introduced by the grating is less pronounced for a shorter wavelength that has higher absorption coefficients. An optimum is found for h_g = 300 nm – 400 nm.

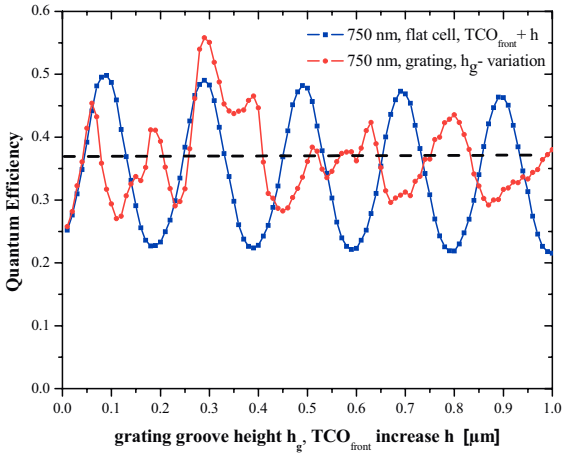

Fig. 5.7: Thickness variation of the untextured front TCO layer in comparison to a groove height dependence for monochromatic red light (λ = 750 nm).

For this absorber layer thickness a *QE* value of up to 50 % can be reached for *h* ~ 400 nm and *h* ~ 800 nm. A high *QE* for h ~ 800 nm can also be seen in Fig. 5.6 (top). This result indicates, at least for the given parameter like wavelength etc., that the general principles of diffraction are not affected by the absorber layer thickness.

For a significantly thicker absorber layer *d (Si)* = 2 µm the average of the *QE* oscillation for the front TCO layer thickness variation is shifted to $QE_{average}$ = 23 %. For *d (Si)* = 1 µm the = 12 %. Therefore, the $QE_{average}$ is almost exactly proportional to the absorber layer thickness which is an understandable result.

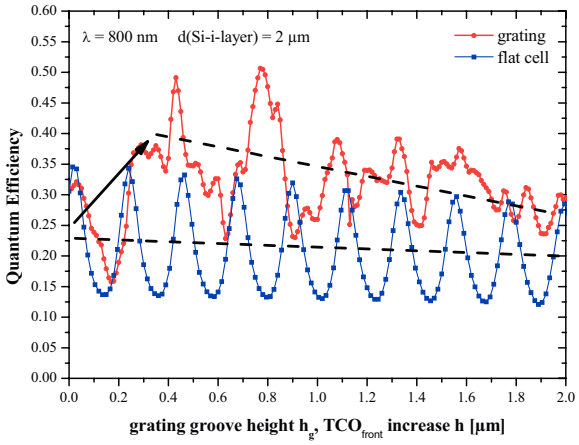

Fig. 5.8: A two times thicker absorber layer d (Si) = 2 µm shifts the average QE of the front TCO thickness variation for a flat layer stack for monochromatic red light (λ = 800 nm) to QE = 23 % and therefore doubles it roughly. The general principles of diffraction are not affected by the absorber layer thickness. The period size is as before P = 1.2 µm.

5.4 Influence of front TCO layer thickness on light trapping

In the following the base thickness of the front TCO layer was varied and the influence of the thickness of this layer on the diffraction properties is investigated and tested with the standard grating height variation. To provide the lateral conductivity in the thin-film solar cell a thickness of ~ 500 nm is needed for the front TCO. Higher aluminium content in the sputter target would lead to a higher electrical conductivity in the layer but this would also lead to a higher parasitic optical absorption. Current TCO developments are aiming to reduce the front TCO layer thickness to minimize the parasitic front contact absorption while maintaining the same electrical conductivity and shorten the deposition process time. Therefore, the influence of the front TCO thickness was tested with thicknesses *d* (TCO_{front}) = 400 nm, 450 nm and 500 nm.

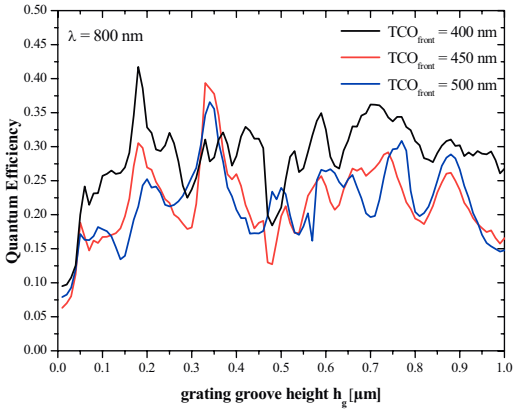

Fig. 5.9: QE calculated for a grating groove height dependence for different front TCO layer base thicknesses under monochromatic illumination (λ = 800 nm). Layer thicknesses d (TCO_{front}) = 400 nm, 450 nm and 500 nm were tested. The period size is P = 1.2 µm.

The *QE* showed a quite similar behaviour for $d(TCO_{front})$ = 450 nm and 500 nm. For $d(TCO_{front})$ = 400 nm a 5 – 10 % higher overall *QE* was calculated with a strong peak at *h* = 200 nm instead of at *h* ~ 300 – 400 nm.

The calculated absorption in the front TCO layer shows a similar curve with peaks at the same grating heights (not shown). This appears for h = 400 nm, 450 nm and h = 500 nm front TCO thickness. This result shows that the thickness of the front TCO layer can influence the light propagation and especially the grating height dependence of the *QE* and front TCO absorption, significantly. A change of the front TCO layer thickness from 500 nm to 450 nm does not change the light propagation, significantly. But a thickness reduction of -20 % (from $d(TCO_{front})$ = 500 nm to $d(TCO_{front})$ = 400 nm)) of the total front layer thickness leads to a 5 – 10 % improved *QE*.

As the absorption in all layers (µc-Si, TCO_{front} and TCO_{back}) shows a similar response to the groove height variation the conclusion can be drawn that the total reflectivity of the layer stack *(Reflectivity = 1 – Absorption (µc-Silicon, TCO_{front}, TCO_{back}))* is strongly dependent on its internal diffractive properties, in this case the structure height. In conclusion, for the investigated 1D grating structure a low reflectivity is a strong indicator for an enhanced absorption in every layer. If this is valid also for 2D / 3D periodic or random structures needs to be investigated.

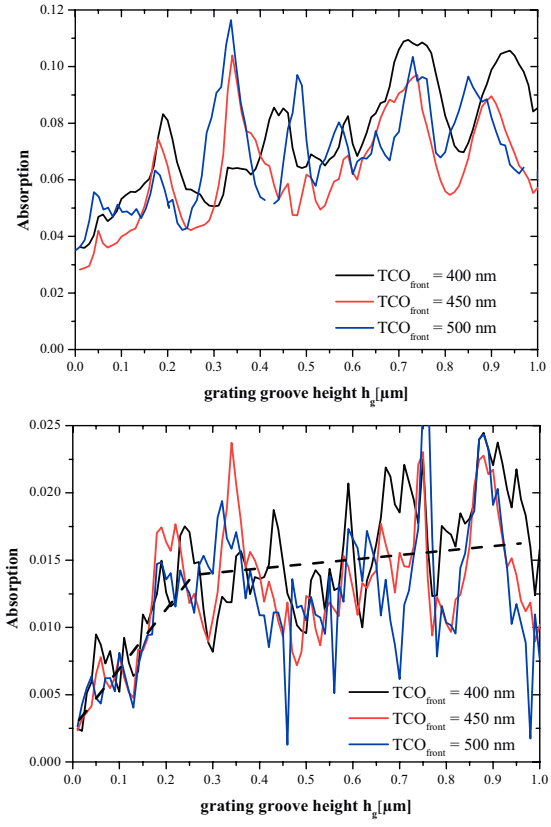

Fig. 5.10: Absorption in TCO_{front} (top) and TCO_{back} layer (bottom) calculated for a grating groove height variation for different front TCO layer base thicknesses under monochromatic illumination (λ = 800 nm). Layer thicknesses d (TCO_{front}) = 400 nm, 450 nm and 500 nm are tested. The period size is P = 1.2 µm.

5.5 Variation of the period size

In the following, the influence of *P* on the light trapping effect was investigated. h_g was set to 0.33 µm and the simulations were performed for red illumination (λ = 800 nm). The simulated *QE* as a function of *P* is shown in Fig. 5.11.

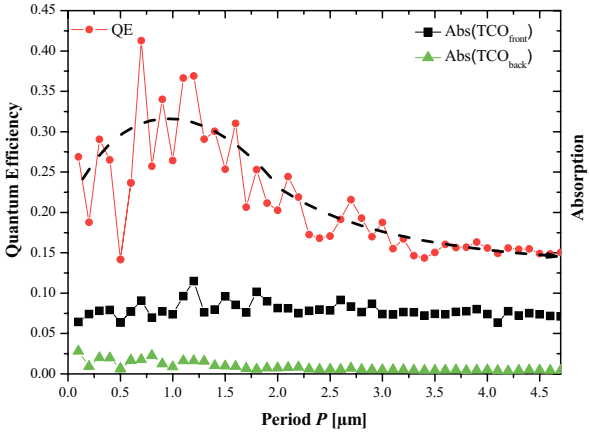

Fig. 5.11: Simulated QE as a function of the Period size P for λ = 800 nm. A maximum in QE is visible for P ~ 1µm. The structure height is constant at h = 0.33 µm.

For cells with an absorber layer thickness of 1 µm the maximum of the red response can be determined for P between 0.7 and 1.2 µm. For monochromatic illumination the *QE* reaches a maximum of 0.4 and the absorbance of the front and back TCO layers is ~ 0.08 and ~ 0.025, respectively. Towards higher and lower *P* the *QE* decreases. In accordance with eqn. 1, the diffraction angle Θ_m within the solar cells tends to very small values for large period sizes

and the structure behaves similar to adjacent flat cells with different front TCO layer thickness. For small periods the *QE* decreases since the diffraction efficiency of the gratings decreases [5.14]. Thus an optimised texture is found for a high spectral response in the long wavelength region using the optimum for *P* and h_g.

The calculated absorption losses in the front and back side TCO layer show only a weak dependence on *P*. As the TCO_{front} layer is several times thicker than the TCO_{back} layer, the absorption in this layer is also more pronounced. For $\lambda = 800$ nm and a structure with a large *P*, the absorption losses in the TCO layers are around 1/3 of the absorbed power in the whole solar cell.

To estimate the general light trapping potential for long wavelength illumination it is essential to calculate the period size dependence also for another wavelength, i.e. $\lambda = 750$ nm (see Fig. 5.12). Again, the curve shows a similar behaviour with a peak of $QE \sim 0.58$ at $P \sim 1.0$ µm. The *QE* for large period sizes $P > 5$ µm is approaching $QE \sim 0.3$. For this shorter wavelength the amount of absorption losses in the TCO layers is much smaller than in the case of $\lambda = 800$ nm, due to lower free carrier interaction probability. It is below 1/6 of the energy being absorbed in the silicon layer.

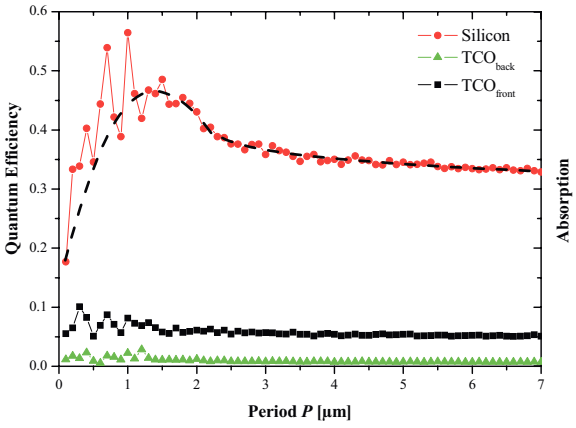

Fig. 5.12: Simulated QE as a function of the Period size P for λ = 750 nm. The structure height is constant at h = 0.33 µm.

The previous two simulations were conducted for a fixed structure height of 0.33 µm. In the chapter about the structure height variation the period size was fixed to P = 1.2 µm. The grating coupler is a "system" depending on two important parameters, P and h, that span a 2 dimensional plane of parameter choices. To be completely sure, that the few chosen parameter sets cover the physics of the whole system, it is necessary to make a test with a grating structure with a high P value, where no beneficial diffractive properties were found. It might be possible that for large P the structure height needs to be adjusted. The relation of h / P is often called the "aspect ratio" in micro optical technologies. It is reasonable that it can only be to some extent an important parameter that determines the optical properties of thin-film silicon solar cells, as the absorber layer thickness of 1 µm is the upper limits for the structure height h.

To investigate the possible role of the aspect ratio, P was fixed at P = 4.0 µm and variation of the structure height is performed. In comparison to the variation of the structure height for a fixed P = 1.2 µm the curve for P = 4.0 µm does not show significantly higher quantum efficiencies due to reduced diffraction angels.

The calculated QE curve deviates only slightly from the thickness variation of the TCO_{front} layer of the flat cell. The maximum in QE of the flat layer stack is only slightly enhanced by the grating for $h \sim 0.53$ µm. The large period size does not lead to an effective diffraction into higher angels for any tested h/p value. Only the minima in QE of the flat cell which are due to a strong refection of the whole layer stack are enhanced as a reduced reflection is generated by the grating.

The QE of the thickness variation of the flat cell is in an optimum, in case of an

odd multiple of the antireflection coating (ARC) condition:

$$kd^{ARC} = \lambda/(4n_{TCO}) \tag{5.3}$$

with the wavelength of the incident radiation $\lambda = 800$ nm and the refractive index of the coating

$$n_{TCO}(800\text{ nm}) = 1.7936$$

and k = 1, 3, 5, 7…

$$d^{ARC} = 112\text{ nm}$$

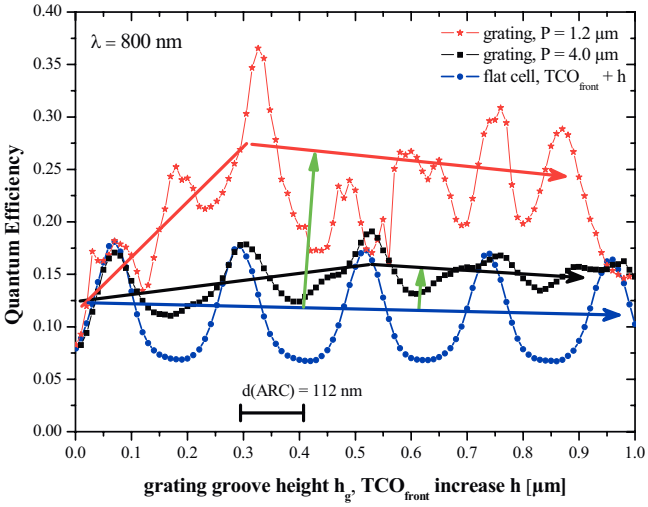

Fig. 5.13: Groove height dependence of the QE for monochromatic red light (λ = 800 nm) for P = 1.2 µm, P = 4 µm in comparison to a flat structure.

The relation of h / P is tested with two calculations with a fixed P and a variable h. For a relation of h / P ~ 1/4 two absolutely different *QE* curves are present. This strongly indicates that the "aspect ration" does not play the important role for light trapping in thin-film cells.

The period size P of the grating determines the angels of diffraction and the structure height h determines the efficiency of diffracting energy into the individual angles. An antireflection effect due to the optical response of the whole layer stack is superposed to both effects.

5.6 Calculation of short circuit current under red illumination

Next, the *QE* of the whole spectral range ($\lambda = 300$ - 1100 nm) of microcrystalline silicon p-i-n-diodes with and without grating coupler (P = 1.2 µm and h_g = 0.3 µm) was calculated and compared to experimental data. Additionally, the calculated absorption ($A = Power_{absorbed}/Power_{incident}$) in the TCO_{front} contact and TCO_{back} contact was plotted. In Fig. 5.14 (top) the *QE* and the absorbance of both TCO layers of a quasi-flat (h_g = 1 nm) solar cell is shown. The difference between experiment and simulation for blue light (350 nm < λ < 500 nm) can be attributed to recombination losses in the front part of the p-i-n structure. The assumption that all photo-generated carriers within the silicon layer contribute to the photocurrent leads to an overestimation, in particular, of the blue response. A part of the carriers photo-generated in the p-layer and p/i-interface region recombine due to the high surface recombination velocity at the TCO/Si contact and the lower lifetime in the doped layer. On the other hand, µc-Si:H solar cells with integrated gratings show an improved blue response in comparison to untextured cells although the reflectance of both diodes is comparable [5.14]. This effect can be likely explained with the collection of carriers photo-generated in the p-layer and the vicinity of the p/i-interface [5.14]. Therefore, for the following discussion of the optical properties of thin-film solar cells with gratings we have considered all the carriers photo-generated within the silicon layers. In the visible wavelength region a *QE* of up to 0.8 for the silicon layer is determined. For light with longer wavelength and a consequently deeper penetration depth a good agreement between the calculated and experimentally determined data is achieved. For $\lambda > 900$ nm the absorbance of the front TCO exceeds the *QE* indicating the dominant role of absorption losses within the TCO front contact on the cell performance. The *QE* of a flat cell with parallel interfaces (Fig. 5.14 (top)), exhibits distinct interference peaks within the simulations, while these fringes are less pronounced within the experimental data.

This can be explained as follows: the simulations are performed for individual wavelength whereas the resolution of the experimental *QE* measurement set-up is around 10 nm, which is mainly determined by the slit of the monochromator. Further spatial inhomogeneities in the sample lead also to a partial suppression of the interference fringes.

In Fig. 5.14 (bottom) the *QE* of a cell with a periodically textured grating coupler (P = 1.2 µm and h_g = 0.3 µm) is shown. As expected from the discussion performed in the previous

section, a significant enhancement of the red response of the cell can be observed in comparison to the flat solar cell (Fig. 5.14(top)).

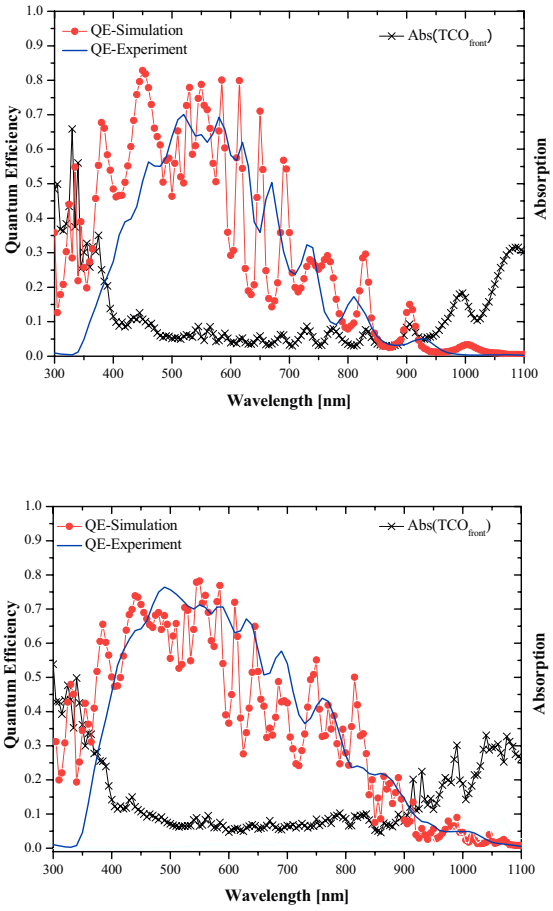

Fig. 5.14: Comparison of simulated and measured QE for a quasi-flat cell (top) and with an integrated grating with P = 1.2 µm and h_g = 300 nm (bottom).

The partial weakening of the sharp peaks shown in Fig. 5.14 (bottom) can be assigned to the diffraction of light at the grating which results in suppression of the zero-order and a diffraction of light into higher orders, which takes place in transmission (in silicon) and reflection (TCO_{front} layer), and the reflection dependence of the periodically textured solar cell as discussed before.

To illustrate the critical aspect of long wavelengths light trapping some examples of absorption profiles are given below. For the period size P = 1.2 µm and a grating groove height of h = 0.3 µm and additional for a flat cell the absorption profiles are shown for λ = 700, 820 and 920 nm. The red area indicates a strong absorption. For λ > 900 the absorption in the TCO_{front} layer both for a flat and a structured cell dominates the optical properties of the device. The "amount" of red absorption areas in each layer directly corresponds to the *QE* or absorption value in Fig. 5.14.

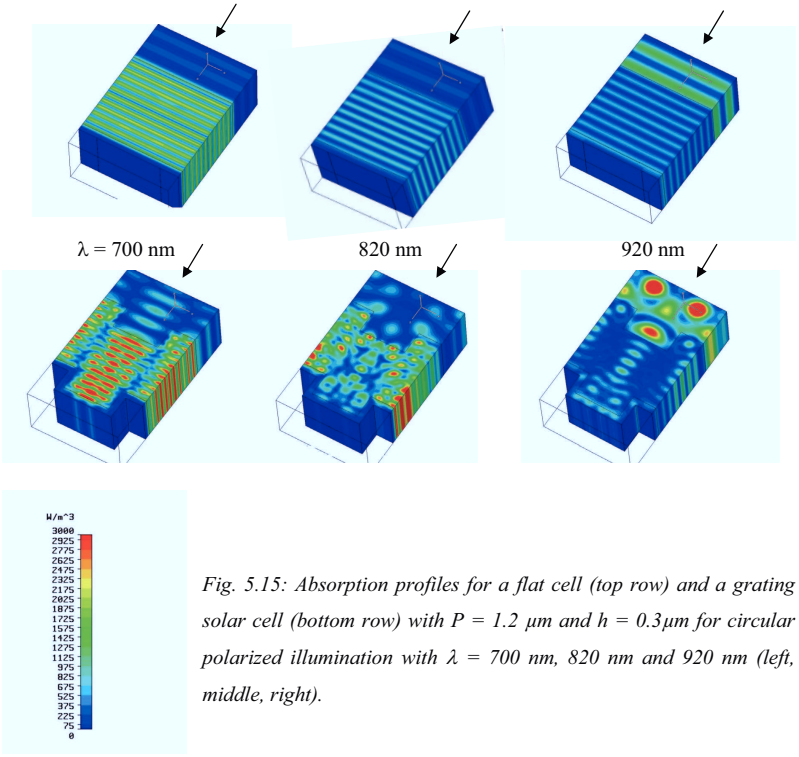

Fig. 5.15: Absorption profiles for a flat cell (top row) and a grating solar cell (bottom row) with P = 1.2 µm and h = 0.3µm for circular polarized illumination with λ = 700 nm, 820 nm and 920 nm (left, middle, right).

In order to find the optimised grating parameters for efficient light trapping of longer wavelength light (red illumination conditions) the *QE* is calculated for wavelengths between 700 and 1100 nm and the photocurrent is determined considering the corresponding wavelength dependent AM 1.5 photon flux. Fig. 5.16 shows the photocurrent as a function of the grating groove height for different periods. A similar trend of J_{sc}, as a function of the grating parameters, as discussed under monochromatic illumination conditions is exhibited.

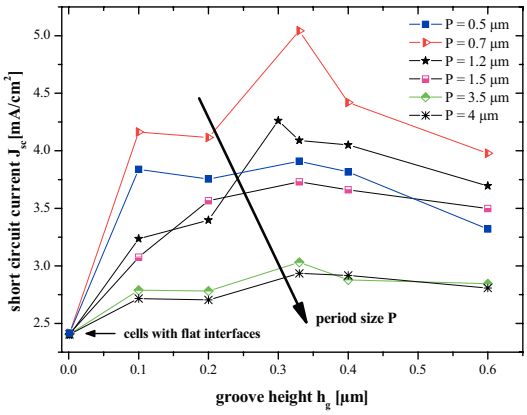

Fig. 5.16: Calculated photocurrent of solar cells with different grating parameters under red light illumination conditions (700 nm < λ < 1100 nm).

Every grating parameter set shows an increased current under red light illumination compared to cells with flat interfaces (h = 0). J_{sc} shows a maximum for h_g = 300 – 350 nm. Towards higher and lower h_g values J_{sc} decreases. For solar cells with integrated grating couplers with P = 0.7 µm and h_g = 0.33 µm the highest short circuit current J_{sc} = 16.94 mA was calculated. This is a gain of 3.92 mA/cm^2 in comparison to a cell with flat interfaces. At this point it has to be mentioned that the reduction in J_{sc} with growing P is more pronounced in the simulations than in the experiment [5.14]. This can be partly explained by scattering of the data, deviation from the rectangular shape of the gratings and a variation in the *G/P* ratio. In contrast to the red current no significant dependence of J_{sc} on the groove height and the period is calculated under blue light illumination as it is mainly absorbed in the front part of

the absorber layer (not shown). This is in good agreement with the experimental findings [5.14]. The simulations indicate that a maximum current under red light illumination conditions can be expected for 300 nm < h_g < 350 nm and 0.7 µm < P < 1.2 µm. Two examples for *QE* curves with high short circuit currents are shown in Fig. 5.17. None of the curves shows higher *QE* values than the other for a wavelength range larger than 50 nm.

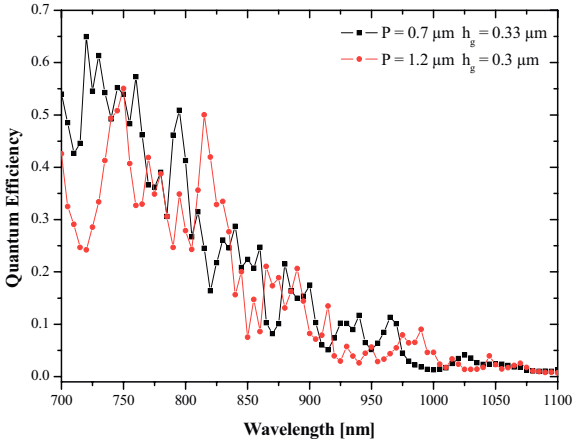

Fig. 5.17: Calculated QE for P = 0.7 µm, h = 0.33 µm and P = 1.2 µm and h = 0.3 µm.

5.7 Influence of front and back silicon / TCO interface

One important issue of cell optimization concerning light trapping is the question of the most appropriate interface texture. Since the cell thickness is in the same range as the feature size, there is no means of investigating this phenomenon experimentally. To address this question, simulations were conducted where only one TCO/silicon interface was designed as a grating coupler. The structure denoted "grating-flat" has a transparent grating at the front-side (TCO_{front} /silicon) and a flat silicon/TCO_{back}/Ag back contact. The vice versa structure "flat-grating" has a flat TCO_{front} /silicon interface and a Bragg reflector (periodically textured silicon/ TCO_{back}/Ag) as a rear contact, as shown in Fig. 5.18.

a) grating at front side **b) grating at back side**

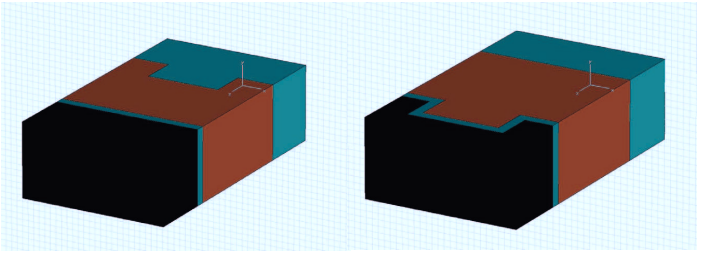

Fig. 5.18: Investigation of modified cell design with a front side grating structure and untextured back reflector (a) in comparison to a flat front side interface a grating structure at the back reflector (b). In the following these structures are called "grating-flat" and "flat-grating" denoting the "front-back" interface morphology.

The performances of these cells are compared with the previously investigated structures containing a transparent grating coupler at the front side and a Bragg reflector at the rear side of the solar cell. This structure is denoted as "grating-grating". Within these simulations, we took care that the absorber volume was kept constant. For all diodes J_{sc} is calculated as a function of P for two selected h_g of 100 and 300 nm under red illumination conditions (λ = 700 – 1100 nm). Within all simulations the current density increases with groove height (Fig. 5.19). Further, with increasing P the calculated current density tends towards the value of the flat structure. For cells with large grating period and equal height similar current values are calculated independent of the position of the grating. The results demonstrate that, in particular, a grating coupler with h_g = 300 nm positioned at the front side of the solar cell has a significant influence on the optical properties of the cell, because comparable current densities are achieved from the simulations of the structure "grating-grating" and "grating-flat".

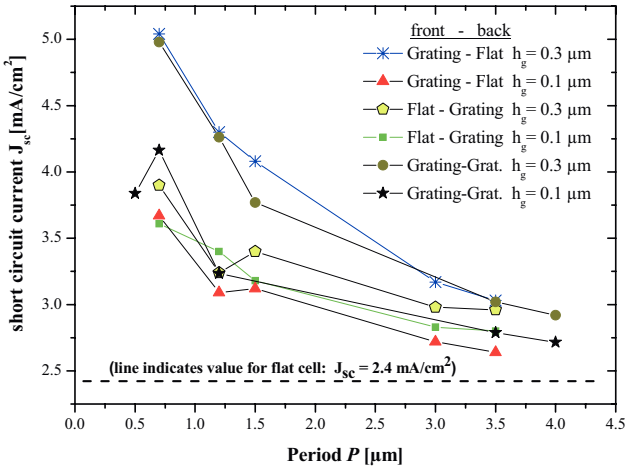

Fig. 5.19: Influence of the front and back side morphology on the short circuit current (J_{sc}) for 700 nm < λ < 1100 nm.

Furthermore, the influence of the back side TCO thickness has been tested (not shown). For the "grating-grating" structures with a strong light trapping effect (P = 1.2 µm, h_g = 300 nm) an increase of the TCO back contact thickness from 80 nm to 360 nm, which corresponds to an optical thickness of $\lambda/4$ and λ (for a wavelength of around 700 – 800 nm), respectively, has no significant effect on the calculated red response. The red response decreases by -0.1ma/cm^2 for TCO_{back} thickness > 200 nm. Performing this calculation for cells with a smaller groove height (h_g = 100 nm), an increase in the red current of 13% is calculated for a larger TCO_{back} side layer (360 nm) in comparison to a thin one (80 nm) although this layer has increased absorption losses with growing thickness. Thus, the diffraction efficiency of the Bragg reflector can be improved by increasing the back side TCO layer thickness for solar cells with insufficient light diffraction efficiency at the front side. For a flat front interface, the so called "flat – grating" structure the importance of the diffraction at the front side texture is evident if the red current is compared with the "grating-grating" structure red current. A missing diffraction at a grating coupler textured front interface can lead to losses in red current of > 1 mA/cm^2. For a "flat – grating" structure with h_g = 100 nm the calculated red

current is ~ 0.3 mA/cm^2 lower for the standard TCO_{back} side thickness of 80 nm and up to 1mA/cm^2 lower for TCO_{back} > 250 nm than the "grating-grating" structure with h_g = 100 nm. For the "flat – grating" structure with h_g = 300 nm an increase in the red current of 18 % is calculated for a larger TCO_{back} side of 360 nm in comparison to a thin one. Therefore, certain parameter and interface setups can result in higher currents for increasing TCO_{back} side thicknesses. This increase can also be caused by a better optical adaption of the whole layer stack. It occurs only if the previous diffraction at the front side interface was insufficient. If the front side texture is well adapted the red light absorption cannot be increased with a thicker TCO_{back} contact layer. Thus, the optimization criteria of a back contact depend strongly on the scattering properties of the front contact.

To separate the two important light trapping properties: (i) antireflection and (ii) diffraction of light into the absorber, the AR effect of a grating shaped interface between 2 materials is discussed.

5.8 Antireflection effect of grating shaped interface

Using rigorous coupled-wave analysis Gaylord and co-workers [5.12] calculated the antireflection condition for high spatial-frequency rectangular shaped surface-relief phase gratings. Their derivation considers the filling factor, groove depth and polarization. They found that these corrugated surfaces may act as antireflection coatings. For several ratios of incident wavelength to grating period as a function of filling factor, groove depth, angle of incidence and polarization they calculate the reflected power. It is demonstrated that the use of triangular or sawtooth structure is not the only way to obtain an antireflection behavior as previously suggested [5.13].

The basic surface relief grating is shown in Fig. 5.20. The grooves are periodically spaced in *x*-direction with period *P*. The grating vector $\vec{K}$ is thus given by

$$\vec{K} = (2\pi / P)\vec{x} \tag{5.4}$$

With $\vec{x}$ being the unit direction vector. An electromagnetic wave incident on the grating is producing the forward-diffracted and backward-diffracted waves.

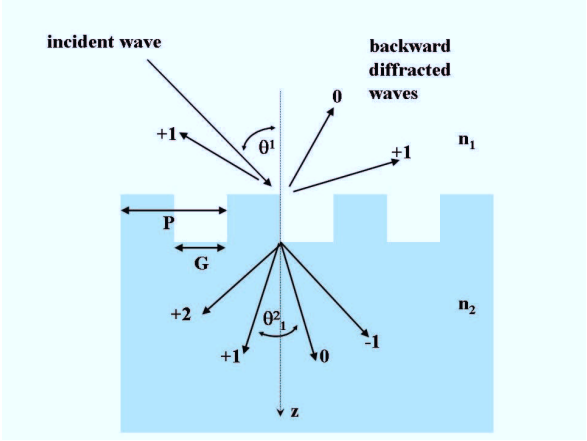

Fig. 5.20: Diffraction geometry of a surface relief grating. The period size (P) is two times the width of the groove (G).

For the forward-diffracted (transmitted) waves the grating equation from the phase matching requirement gives:

$$i\lambda = (n_1 \sin\theta^1 + n_2 \sin\theta_i^2) \tag{5.5}$$

with i as the diffraction order, λ the wavelength, θ^1 the angle of incidence in the dielectric of refractive index n_1, n_2 the refractive index of the grating material, and θ^2_i is the angle of diffraction in the grating material of the i-th order forward-diffracted wave. The backward-diffracted-order diffraction angles θ^1_i are given by the corresponding grating equation

$$i\lambda n_1 = P(\sin\theta^1 + \sin\theta_i^1) \tag{5.6}$$

for the case that the wavelength and angle of incidence satisfy the Bragg condition

$$m\lambda / n_1 = 2P\sin\theta^1 \tag{5.7}$$

where m is an integer, the diffraction efficiency is generally maximized for the i-th diffracted order, where $i = m$.

For antireflection purposes the primary interest is to define gratings with all orders, other than $i = 0$, to be evanescent. Thus, in the above equations there are no real solutions for the diffraction angles θ^1_i and θ^2_i for i other than $i = 0$. In this case the $i > +1$ and $i < -1$ orders are all cut off, and only the $i = 0$ transmitted order and the $i = 0$ reflected order are propagating.

In the Rigorous Coupled Wave-Analysis (RCWA) the field inside the grating is expanded in terms of space-harmonic components that have variable amplitudes in the thickness direction z of the grating. This field expansion together with the periodicity condition (Floquet condition) is then substituted by the appropriate TE and TM polarized wave equations resulting in an infinite set of coupled-wave equations. The space harmonic amplitudes are then solved for in terms of the eigenvalues and eigenvectors of the differential equation coefficient matrix. After applying boundary conditions for the electric and magnetic field across the boundaries (i.e. the tangential component is continuous) a set of linear equations is formed. Finally, the amplitudes of the propagating orders and the evanescent orders can be determined [5.12].

The calculated results showed clearly that the ratio of the incoming wavelength to the structure size determines whether orders other than the 0-order (in transmission and reflection) are able to propagate. For $\lambda / P = 1$ such orders exist, whereas for $\lambda / P = 1.5$, $\lambda / P = 2.5$ and $\lambda / P = 10$ orders other then the 0-order in transmission and reflection are not able to propagate. This also depends on the values of n_1 and n_2.

For the case of $n_1 = 1$ and $n_2 = 1.5$ Gaylord et al. found that the minimum reflected power at normal incidence as a function of the filling factor can be significantly reduced with the right choice of groove depth. For $\lambda / P = 1$ both linear polarized plane waves can reach zero (at different filling factors though) but the random polarization does not reach zero reflected power and the reflectivity remains at ~ 1 %. For a higher λ / P - factor the minima of the reflected power of both polarizations and the random polarization approach the filling factor of 50 % and reach for $\lambda / P = 10$ and the given example almost zero reflectivity.

Consequently, a grating structure is more sensitive to the polarization of the incoming wavelength if the wavelength has quasi the same size as the period of the structure.

In the limit of long wavelength ($\lambda >> P$) the antireflective behavior for light in a dielectric of refractive index n_1 which is normally incident on a dielectric of refractive index n_2 occurs for a grating groove with $G/P = ½$ and a filling factor following the conditions:

$$grating\ groove\ depth = \lambda\ /\ 4\ (n_1\ n_2)^{1/2} \tag{5.8}$$

$$filling\ factor^{perpend.Pol.} = n_1 / (n_1 + n_2) \tag{5.9}$$

$$filling\ factor^{parallel.Pol.} = n_2 / (n_1 + n_2) \tag{5.10}$$

For the perpendicular (parallel) polarization the electric field is perpendicular (parallel) to the grating vector. The reflection/incoupling properties of thin-film silicon solar cells are mainly determined by the ZnO / silicon interface as this has a larger difference in the refractive index than the glass / ZnO interface. To estimate the grating dimensions and shape of the interface that are necessary for a reduced reflection the above equations can be used to calculate the filling factor and the grating groove depth for both polarization. This is only valid for the limit of long wavelength ($\lambda >> P$), though.

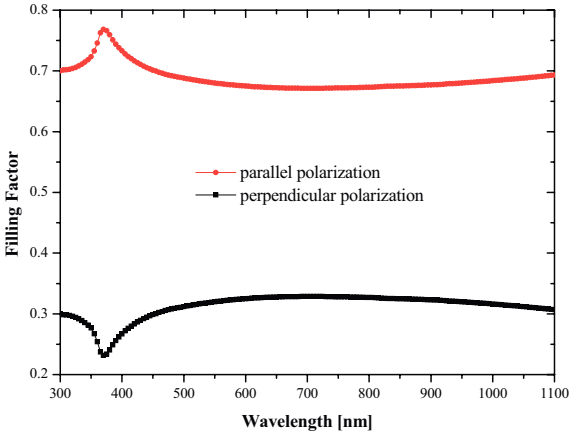

Fig. 5.21: The graph shows the filling factor of a ZnO / silicon interface depending on the wavelength for both polarizations. It is only valid for the limit of long wavelength ($\lambda >> P$).

Further, the equivalence of antireflection grating layers to homogenous AR coatings at long wavelength leads to the conclusion that a stair-step surface relief profile of *N* steps can be used to replace a coating of *N* individual homogenous layers. In every step of the stair-step surface relief grating a different filling factor can be used. A multi layer thin-film coating could thus be replaced by a stair-step grating fabricated directly on the substrate.

For thin-film silicon solar cells the anti reflection properties are important but less critical than a sufficient diffraction of the light at the silicon /TCO interface(s) into higher angles to overcome the weak absorption of the thin silicon absorber layer. Therefore, the period of the grating (or other interface texture) structure has to be in the range of the incoming wavelength to support transmission orders $i > 0$ and $i < 0$, i.e. a diffraction into large angles.
Besides a binary grating a stair-step grating structure is of interest that could combine a continuous multilayer AR coating effect that incouples a complete wavelength range and has additionally diffractive properties.

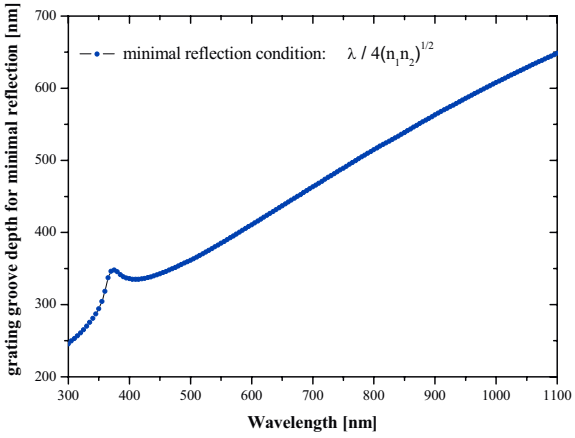

Fig. 5.22: Grating groove depth calculated for a minimal reflection depending on the wavelength. This is only valid for the limit of long wavelength ($\lambda >> P$).

5.9 Variation of groove width to period size ratio

In the next chapter the shape of the grating structure was investigated. In the previous solar cells with grating couplers the groove width to period ratio G / P = ½ was chosen. In chapter 3.1 AR coatings realised by grating structures are introduced. There, this variable is called "filling factor". To keep the solar cell comparable the absorber layer volume and TCO front layer volume was kept constant.

a) $G / P = 3 / 4$ **b)** $G / P = 1 / 4$

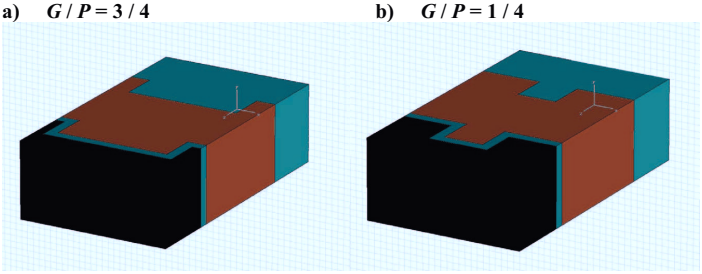

Fig. 5.23: The groove width to period size ratio G/P is investigated in the following. In case a) G/P = ¾ and in case b) G/P = ¼.

The parameters structure height h and period size P is the same as used before. The general difference between the two cases is whether the small (feature) area at the front TCO / silicon interface is upright or inverted. For $G / P = 3 / 4$ a small feature area of silicon is upright on the silicon layer and for $G / P = 1 / 4$ a small feature area of front TCO is positioned inverted into the silicon layer.

To understand the diffractive properties of the two different interface shapes the previously analysed groove height variation under monochromatic long wavelength illumination was performed. The TCO_{front} layer thickness variation and the groove height variation are calculated for G / P = ¼, ½, and ¾ under monochromatic, circular polarized illumination with $\lambda = 800$ nm. The G / P = ¾ case with the upright silicon feature shows a similar QE dependence for increasing groove height as for the G / P = ½ case. A significant increase in

QE can be seen for small groove height values $h \sim 0.1$ µm. Here, the *QE* values are almost doubled.

For the case of $G / P = ¼$ the curve deviates strongly from the other two cases. It's total *QE* oscillation is approximately as strong as in the TCO_{front} thickness variation of the flat cell. This is understandable as for $G/P = ¼$ exactly ¾ of the TCO / silicon interface is at the same height as for the flat cell. The small TCO inclusion leads to an additional diffraction and increases the *QE* especially for the minima of the flat cell oscillation.

For $h \sim 0.15$ µm and $h \sim 0.4$ µm, thus contrary to the *QE* maxima of TCO_{front} thickness variation curve the $G / P = ¼$ case shows the highest *QE* values.

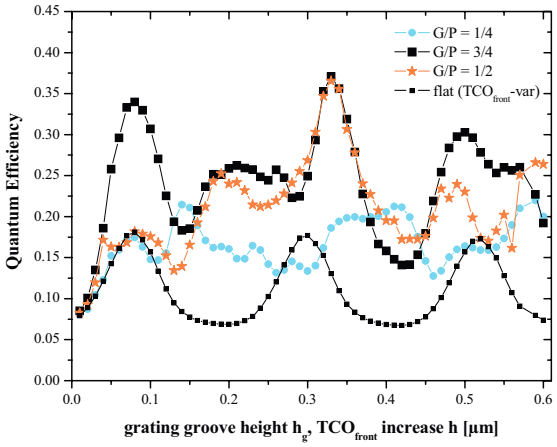

Fig. 5.24: Groove height dependence of the QE for monochromatic red light (λ = 800 nm) for P = 1.2 µm for groove height to period size ratio G/P = ¼, ½ and ¾. For a G/P = ¾, i.e. a small upright silicon feature at the TCO_{front} / silicon interface, a strong increase of the QE is calculated for small structure height h ~ 0.1 µm.

To make sure that this calculation for a single wavelength is not caused by an interference effect due to the geometry of the unit cell; also for $\lambda = 850$ nm and $\lambda = 750$ nm the simulation

was repeated. For $\lambda = 850$ nm the *QE* values of $G / P = ¾$ in relation to the QE values of $G / P = ½$ showed the same behaviour. For $\lambda = 750$ nm the effect of higher *QE* values for the $G / P = ¾$ case is also visible but not as pronounced as for longer wavelengths. (Figures for $\lambda = 850$ nm and $\lambda = 750$ nm are not shown)

To identify the meaning of these calculations for single wavelength for the short circuit current the red light J_{sc} was calculated for $\lambda = 700$ nm – 1100 nm. The period size values $P = 0.7$ µm and $P = 1.2$ µm were selected as they showed promising high red currents for groove heights $h \sim 0.3$ µm for $G / P = ½$. Fig. 5.25 shows the calculated J_{sc} for $G / P = ¼$, ½ and ¾ for $P = 0.7$ µm and 1.2 µm und groove heights $h = 0.1$ µm, 0.2 µm, 0.3 µm and 0.4 µm. The highest calculated current is almost doubled compared to the red current of a flat cell. (J_{sc}(*flat*) ~ 2.4 mA/cm^2).

Only for the $G / P = ¾$ ratio the J_{sc} is not increasing with higher groove height. As calculated for the single wavelength calculation for $\lambda = 800$ nm and $\lambda = 850$ nm the $G / P = ¾$ ratio is beneficial for a light trapping effect of textures with small groove heights $h = 0.1$ µm. This is also valid for the red J_{sc}.

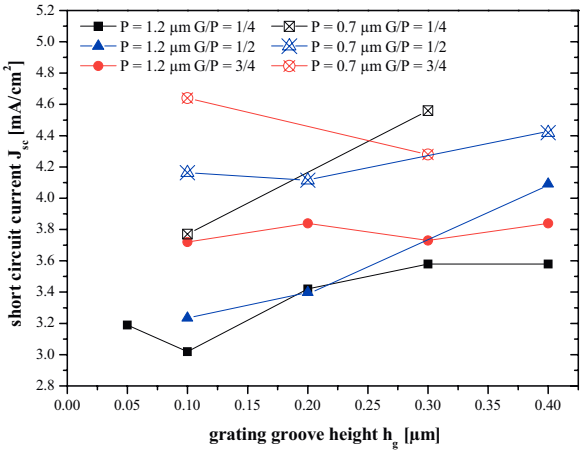

Fig. 5.25: Calculated short circuit current J_{sc} for $\lambda = 700$ nm – 1100 nm. Only for G/P = ¾ a small height h = 0.1 µm is supporting the light trapping properties.

To test the influence of the changed interface shape on the incoupling properties of short wavelength illumination a simulation with λ = 400 nm and an increasing groove height for G/P = ½ and ¾ was performed and compared to flat cell with increasing structure height.
For the chosen P = 1.2 µm a G/P = ¾ results in a lateral size of the upright silicon element of 300 nm. Fig 5.26 shows that the QE shows the previously seen oscillations due to an antireflection effect present for all three curves. The curve for the flat, untextured structure has the steepest decrease in QE for higher h values as it has the highest volume of the TCO_{front} layer. The average QE value of the G/P = ¾ structure (black solid line) is ~ 3 % higher for small groove heights then for the G/P = ½ structure (red solid line). With increasing groove height this small improvement of the blue light incoupling properties is decreasing and equals to zero for h = 500 nm.

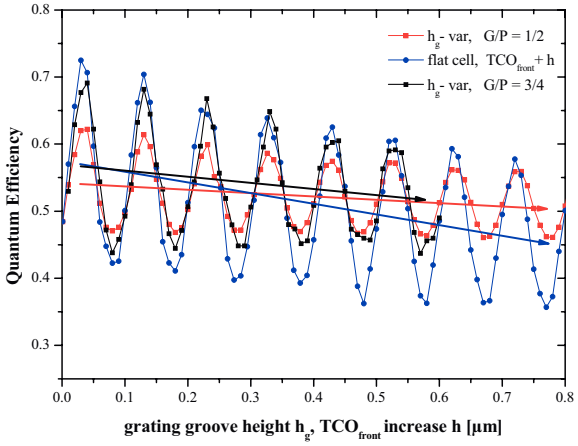

Fig. 5.26: Variation of front TCO layer thickness in comparison to a groove height variation for blue light illumination for λ = 400 nm to investigate the influence of the factor G/P on the incoupling properties of the solar cell. For G/P = ½ and ¾ the QE is oscillating around an almost identical average.

A smaller lateral feature at the TCO_{front} / silicon interface thus improves the blue wavelength incoupling properties only slightly.

5.10 Prototype preparation of thin-film silicon solar cells with line gratings

The gratings were prepared by sputtering of ZnO, photolithography and a lift-off process. First, a ZnO layer of around 500 - 600 nm thickness was rf-magnetron sputtered on a glass substrate at elevated temperature. Afterwards, photo resist was applied and developed using a standard exposer and chromium masks for patterning. Then, a second ZnO layer was deposited at room temperature all over the substrate. Finally, the unwanted ZnO regions were removed by a lift-off step. The thickness of the second ZnO layer determines the groove height of the grating. P and h_g were varied from 1 to 4 µm and 100 to 600 nm, respectively. The length of the grooves G was intended to be half the length of the period (G/P = 1/2). The value (G/P = 1/2) is also investigated within the simulations. Scanning electron microscopy (SEM) and atomic force microscopy (AFM) were used to characterize the morphology of the gratings. As an example, Fig. 5.27 shows selected scanning electron microscopy and atomic force microscopy images of ZnO gratings with a period size of 1.2 µm for a groove height of 200 nm (top), 400 nm and 600 nm (bottom). However, due to technical reasons (lift-off process) the realized G/P ratio can slightly deviate from 1/2. More details regarding the prototype preparation can be found in reference [5.14].

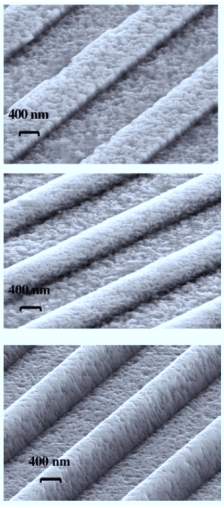

Fig. 5.27: Scanning electron microscopy (SEM) images of ZnO gratings with a period size of 1.2 µm and a groove height of 200 nm (top), 400 nm (middle) and 600 nm (bottom). The plotted scale is valid only along the horizontal axis due to the oblique perspective.

State-of-the art p-i-n solar cells with a µc-Si:H i-layer thickness of 1 µm were then deposited on top of the gratings by plasma enhanced chemical vapor deposition (PECVD). The fill factors (*FF*) of the µc-Si:H p-i-n-diodes with different periods and h_g of 100 nm and 300 nm were around 72 % and 69 %, respectively. The decrease of *FF* with increasing h_g is attributed to an increase of the series resistance R_s caused by the low conductivity of the ZnO strips and to shunting problems. An complete experimental study of a-Si:H and µc-Si:H solar cells based on a p-i-n structure with grating coupler is given in Ref. [5.14].
The measured short circuit current densities of a-Si:H and µc-Si:H solar cells show most of the trends that have also been found in the simulation study. Fig. 5.28 shows the current of both cell types for blue, red and AM1.5 illumination conditions. A detailed discussion can be found in Ref. [5.14].

Within this paper it is shown, that a strong variation in specular transmittance and haze function of gratings with different period sizes and groove heights is not reflected in their quantum efficiencies.

The haze is often taken as the ideal parameter to evaluate the scattering properties of substrates. It is defined as the ratio of diffuse transmitted light to total transmitted light.

Haze = Diffuse Light / Total transmitted light

A high haze value of 80 % means that 80 % of the light is propagating diffuse after entering the cell whereas 20 % is propagating in a direction not deviated from the angle of incidence.

Fig. 5.29 shows the measured haze of the gratings for different period sizes in comparison to the haze of a random texture. The results clearly show that the haze is not useful for the investigation of light trapping in thin-film devices with periodic structures. Therefore, a straight-forward discussion of data derived from far-field measurements in ambient air and its contribution to the understanding of near field phenomena within a thin-film solar cell is critical.

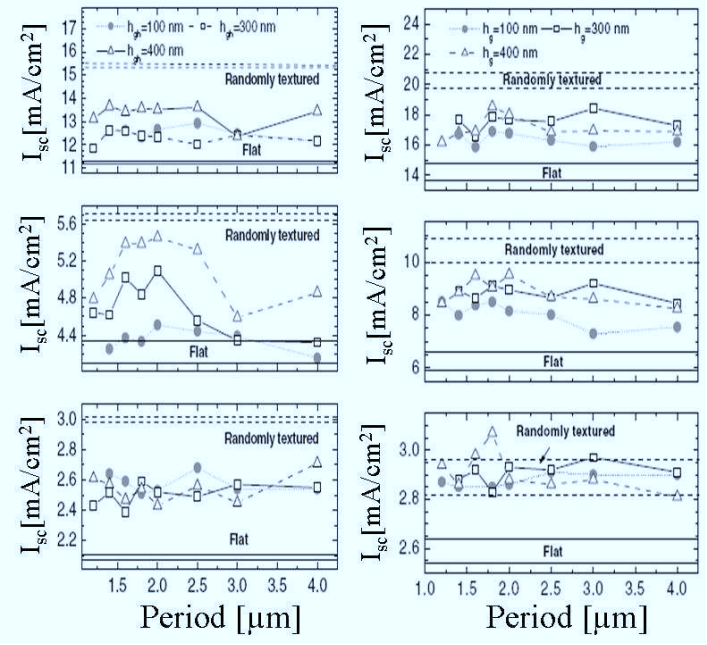

Fig. 5.28: Short-circuit current density of a-Si:H solar (left) cells measured under AM1.5 illumination (top), red illumination (middle) and blue illumination (bottom) conditions as a function of period in comparison with cells deposited on flat and randomly textured substrates. Short-circuit current of µc-Si:H solar cells (right) measured under AM1.5 (top), red (middle) and blue (bottom) illumination as a function of period in comparison to cells deposited on flat and randomly textured substrates. The horizontal lines indicate the upper and lower limit of the scattering of data of "good cell results" for randomly textured (dotted line) and flat cells (solid line).

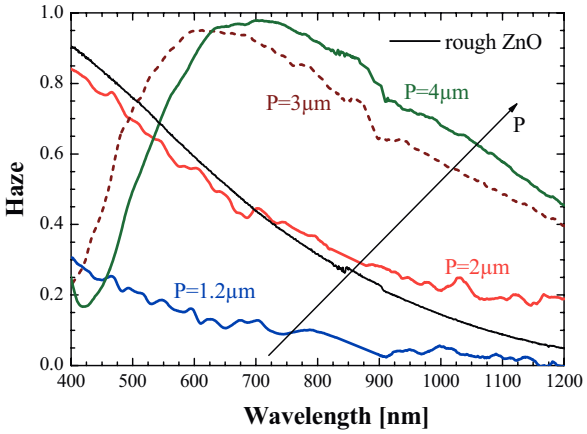

Fig. 5.29: The haze measured for prototype grating structures as a function of the incoming wavelength. For increasing period size the haze is enhanced. The black line shows the haze of a randomly rough textured ZnO. For P = 3 and 4 µm a high haze is found but a direct correlation to high short circuit currents is not found.

References Chapter 5:

[5.1] R. H. Morf, H. Kiess, C. Heine, Diffractive Optics for Industrial and Commercial Applications, **361**, (Akademie Verlag, WILEY VCH, Berlin, 1997).

[5.2] J. Zimmer, H. Stiebig, H. Wagner, Proceedings of the Second WCPEC, 944, (Vienna, 1998).

[5.3] C. Eisele, C. E. Nebel, M. Stutzmann, J. Appl. Phys. **89**, 7722 (2001).

[5.4] N. Senoussaoui, M. Krause, J. Müller, T. Brammer, H. Stiebig, Thin solid films **397,** 451–452 (2004).

[5.5] Y. Mai, S. Klein, R. Carius, H. Stiebig, X. Geng, F. Finger, Appl. Phys. Letters **87**, 073503 (2005).

[5.6] H. Stiebig, T. Brammer, T. Repmann, O. Kluth, N. Senoussaoui, A. Lambertz, H. Wagner, Proceedings of 16th European Photovoltaic Solar Energy Conference, 549 (Glasgow, 2000).

[5.7] K. H. Jun, R. Carius, H. Stiebig, Physical Review B, **66**, 115301, E02 (2002).

[5.8] K. H. Jun, E. Bunte, H. Stiebig, IEEE Transactions on Electron Devices, **52**, 1656 (2005).

[5.9] J. Zimmer, H. Stiebig, H. Wagner, J. Appl. Phys. **84**, 01611 (1998).

[5.10] H. Stiebig, A. Kreisel, K. Winz, N. Schultz, C. Beneking, T. Eickhoff, H. Wagner, M. Meer, Proceedings of the 1st WCPEC, 603-606 (Hawaii, 1994).

[5.11] T. Weiland, Electronics and Communication AEU, **31**, 116 (1977).

[5.12] T. Gaylord, W. Baird, M. Moharam, Appl. Optics, **25**, 456224 (1986).

[5.13] R. C. Enger, S. K. Case, Appl. Optics, **22**, 3220 (1983).

[5.14] H. Stiebig, N. Senoussaoui, C. Zahren, C. Haase, and J. Müller, Prog. Photovoltaics **14**, 63813 (2006).

6 Investigation of 2D and 3D multi-step structures

6.1 Microcrystalline solar cells with integrated blazed grating coupler

In one of the first detailed studies presented by Morf et al. [6.1] a reflecting mirror, a rectangular grating and an unsymmetrical grating are placed at the backside of a thin-film silicon solar cell. In contrast to a flat reflecting mirror a diffraction grating at the backside diffracts the incoming light into higher order modes with large angles of reflection. This leads to the desired path length enhancement.

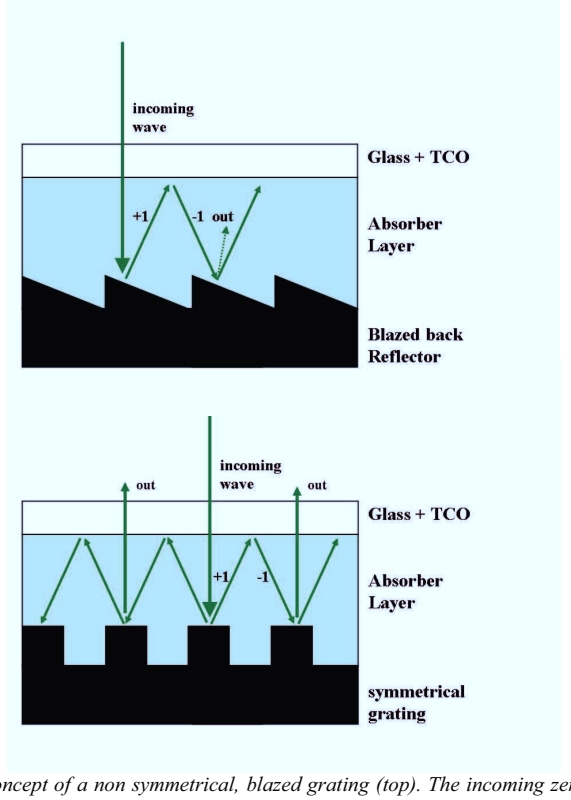

Fig. 6.1: Concept of a non symmetrical, blazed grating (top). The incoming zero-order wave (big arrow) is diffracted by the grating in the right direction. A left-moving wave and a coupling to the zero-order outgoing wave is suppressed. A symmetrical grating (bottom)

allows according to the reciprocity theorem the minus first order (-1) to couple to the zero-order outgoing wave the same way the zero-order incident couples to the plus first order (+1).

Morf states that symmetric gratings might not be the most effective structure for light trapping, as by symmetry left- and right-moving diffracted waves are generated by the grating with equal magnitude.
After total reflection at the absorber layer to TCO interface this left/right-moving wave will impinge again on the grating. According to the reciprocity theorem, a wave being generated by a zero-order wave can also couple to an outgoing zero-order wave. If the -1 order impinges on the blazed grating the tilting of the unsymmetrical structure leads to much smaller probability of a coupling to the zero-order outgoing wave. Thus the light trapping by symmetric structures is limited. For non-symmetric or blazed structures the coupling to the outgoing zero-order can be, in theory, negligible small. Figure 6.1 (top) shows an unsymmetrical back reflector design, with a suppressed left-moving and only right-moving wave, as proposed by Morf. After a total reflection at the front surface there is only a small chance that a zero-order outgoing wave is generated (dotted arrow).

In Figure 6.1 (bottom) a symmetrical grating leads according to the reciprocal theorem to an out-coupling of the minus first order (-1) to the zero-order wave the same way the zero-order incident wave couples to the plus first order (+1) wave. This should lead to partial out-coupling within each period.

Morf showed the potential of the 3 different back reflector designs by calculating the absorption depending on the cell thickness for single polarization and perpendicular incidence of the incident light. The upper limit of the absorption of this device is limited by the front side reflection at the flat interface. It is $A \sim 98$ %. For an absorber thickness of $d \sim 2.5$ µm Morf calculated the absorption $A \sim 59$ % for a planar reflector, $A \sim 75$ % for a rectangular structure and $A \sim 87$ % for a blazed, unsymmetrical grating. For increasing cell thickness the absorption of all 3 back reflector designs leads to similar values, i.e. for $d = 100$ µm the absorption $A \sim 88$ % for a planar reflector, $A \sim 93$ % for a rectangular structure and $A \sim 95$ % for a blazed grating.

The limitation of the unsymmetrical back reflector design is, of course, that this concept works only for a small deviation from the perpendicular angle of incidence. If the angle of

incidence is outside of the necessary incidence cone then left- and right-going diffracted waves are created. In addition only polarized light was used.

The FIT simulations of a flat TCO_{front} / silicon interface with a rectangular grating at the silicon / TCO_{back} interface in comparison to the vice-versa case have shown that especially the reflection at the front interface (TCO_{front} / silicon) have to be as low as possible to reach high quantum efficiencies. For different periods and structure heights the influence of a textured or flat interface at the front or back side were tested and the highest currents were calculated for a textured front interface. This comparison was performed for red light 700 nm < λ < 1100 nm. For comparable grating parameters the current of a structure with a flat front interface was up to 1 mA/cm^2 (~ -25 %) lower than for a structure with a textured front interface and a flat or textured back interface.
A minimal outgoing wave can be realized by choosing the optimal grating structure, as shown in the chapter about the grating theory, but this is only valid for a polarized wave.

6.2 Reflection at flat interfaces

To understand and estimate the origin of the reduction in *QE* and short circuit current for a solar cell structure with a flat front interface between the TCO and silicon layer a geometrical optical calculation of the partial reflection at this interface can be taken into account.

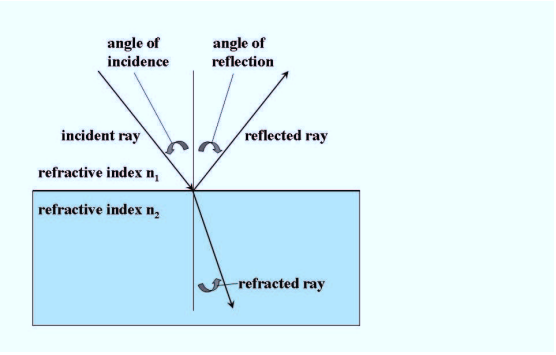

Fig. 6.2: Angles for reflection and refraction at flat interface of two adjacent media with different refractive indices given by the Snellius law of refraction.

The Snellius law of refraction [6.2] for two adjacent media with different refractive indices gives the angular relation between the incoming and the diffracted ray. With n_1 and n_2 being the refractive index of each layer and α and γ the propagation angle in each layer, respectively.

$$\sin(\gamma) = (n_1 / n_2) \cdot \sin(\alpha) \tag{6.0}$$

In Fig. 6.3 the angles for reflection and refraction of light at an interface of silicon and ZnO calculated by the Snellius law are shown for 3 selected wavelengths. Shorter wavelength (λ = 400 nm) are stronger refracted than longer wavelengths.

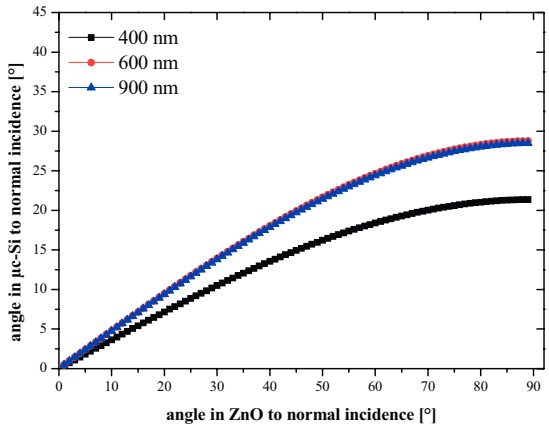

Fig. 6.3: Angles for reflection and refraction of light at an interface between silicon and ZnO calculated by the Snellius law.

In case that the right term is smaller than 1 partial reflection occurs. The light ray is diffracted and partly reflected. If the right term is bigger than 1 no solution for γ exists and total reflection occurs. For the partial reflection case the quantity of reflected and diffracted light can be derived by the Fresnel equations [6.2].

The quantity of the partial reflection depends on the polarisation of the incoming wave and the angle of incidence and the refractive index of the adjacent layers. R_p stands for a

polarisation of the incoming wave parallel to the plane of incidence and R_s for the perpendicular case.

$$R_S = [\sin(\alpha-\gamma)/\sin(\alpha+\gamma)]^2 = [(n_1\cos\alpha - n_2\cos\gamma)/(n_1\cos\alpha + n_2\cos\gamma)]^2 \quad (6.1)$$

$$R_P = [\tan(\alpha-\gamma)/\tan(\alpha+\gamma)]^2 = [(n_2\cos\alpha - n_1\cos\gamma)/(n_2\cos\alpha + n_1\cos\gamma)]^2 \quad (6.2)$$

For circular polarized light the reflection is given by: $R = (R_S+R_P)/2$ (6.3)

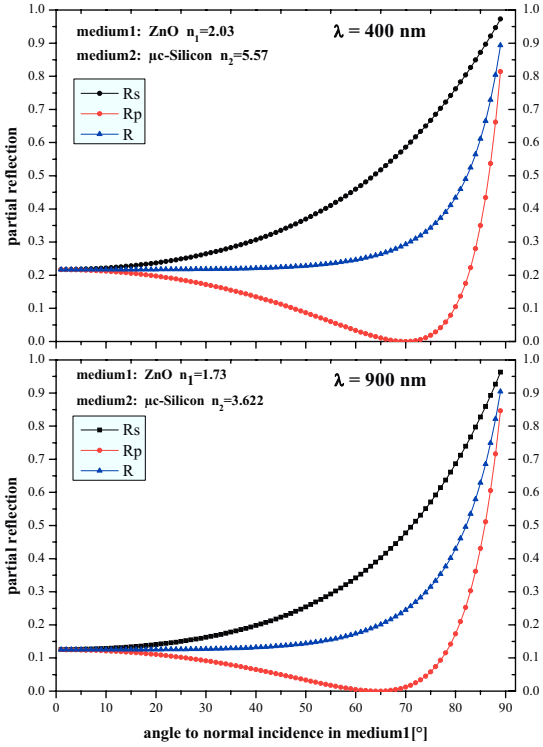

Fig. 6.4: Partial reflection of a flat ZnO / silicon interface for 2 linear polarisations (R_s, R_p) and circular polarized light for λ = 400 nm (top) and λ = 900 nm (bottom) under variation of the angle to normal incidence.

To understand the influence of a flat interface between the TCO_{front} and the silicon layer, the partial reflection is calculated for the case that the light enters through the ZnO and impinges on the silicon layer. This is done for λ = 400 nm and λ = 900 nm the precise refractive index for both materials and both polarizations.

6.3 Comparison of blazed and rectangular structure

For λ = 400 nm the reflection value for normal incidence (0°) of both polarisations is quite high with R ~ 22 %. For λ = 900 nm the reflection for perpendicular incidence is R ~ 12 %. For both wavelengths R remains for α = 0 - 60° on the almost same level and increases strongly to R ~ 100 % for α ~ 90°. For α ~ 70° R_p reaches a minimum of R_p ~ 0 whereas R_s increases without a minimum with higher angles.

Especially for short wavelength this geometrical calculation shows the limitation of an optical design with a flat TCO_{front} / silicon interface as due to the significant difference in refractive index the reflection is quite high (R = 22 %). This can only be minimized with a smoother gradient on the refractive index of both materials. Therefore, every interface shape that has a filling factor of around 0.5 and a thickness of preferably ~ $\lambda/4$ will lead to a reduction of this interface reflection.

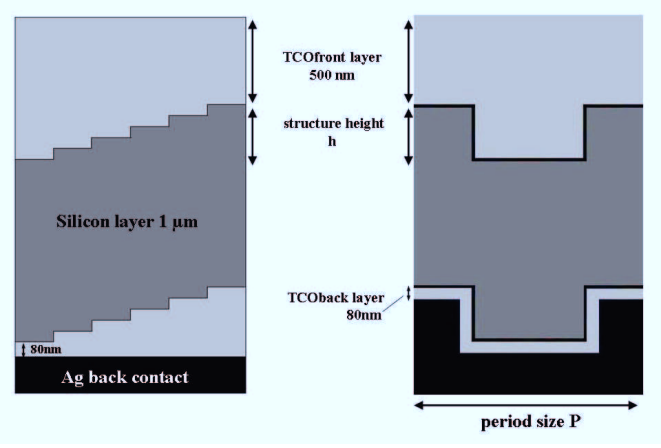

Fig. 6.5: Simulation unit cell of an unsymmetrical, blazed diffraction grating structure.

To investigate the proposed unsymmetrical texture, test its potential and at the same time try to overcome its incoupling limitation an unsymmetrical, blazed structure with 6 discrete levels as in Fig. 6.5 was implemented in the thin-film silicon solar cell model.

To be able to compare the results to the previous rectangular grating simulation the volume of the TCO_{front} contact layer was kept constant. The microcrystalline silicon absorber layer has again a uniform thickness of 1 µm. The minimum layer thickness of the TCO_{back} contact layer is 80 nm (on the lower left side of the unit cell).

Both solar cell textures have a period P = 1.2 µm and structure height h = 0.3 µm.

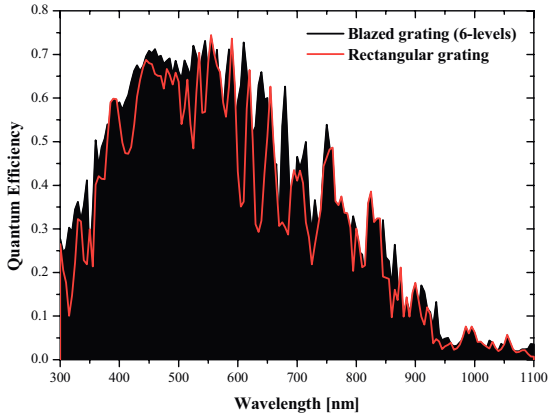

Fig. 6.6: Calculated quantum efficiency of a rectangular grating and a blazed 6-level texture integrated in a thin-film silicon solar cell. In the short wavelength range λ < 550 nm the blazed texture (black area, used only for illustration reasons) has significantly higher QE values than the rectangular grating (red line). For λ > 550 nm especially the high peaks are not as pronounced and also lower QE values are found.

The *QE* calculation in figure 6.6 shows a clear improvement in the blue spectral region 300 nm < λ < 550 nm for the blazed cell design. Also, between 600 nm < λ < 700 nm the *QE* of the blazed design is superior to the binary grating design.

In comparison to a flat structure the total short circuit current increases by 28.2 % under AM 1.5 illumination conditions, whereas the rectangular grating gave only an increase of 18.7 % in J_{sc}.

As investigated by Morf [6.1] an unsymmetrical, blazed grating represented by 3 discrete levels can enhance the absorption of a-Si:H thin-film solar cells by 30 % compared to a flat cell, whereas in his calculation a rectangular shaped grating (consisting of 2 discrete levels, i.e. groove height = 0 and = *h*) increases the absorption by only 20 % (under AM 1.5 illumination conditions).

In our simulations for µc-Si:H thin film cells, though, a quite similar result was achieved. Figure 6.7 shows the increase in short circuit current in relation to a flat cell specified for three spectral regions.

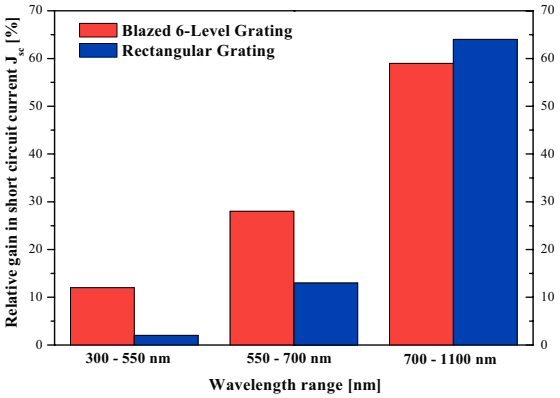

Fig. 6.7: Comparison of relative gain in J_{sc} of cells with a blazed grating (6-levels) and a rectangular shaped grating compared to a flat cell for different wavelength ranges. Both grating coupler have P = 1.2 µm and groove height h_g = 0.3 µm.

In contrast to Morf's calculation where the gain of a-Si:H solar cells is caused by an equal contribution of a reduced reflection in the blue & green wavelength region and an improved

absorption in the red range, we calculated a strong gain in the red and near infrared light current and a smaller gain for the blue / green part of the light spectrum for µc-Si:H diodes.
For near-infrared light with a wavelength between 700 and 1100 nm (in this range the spectral sensitivity of a-Si:H is very low due to the a-Si:H bandgap of 1.74 eV) the photocurrent increases in comparison to a flat cell value by 59.4 % and 63.8 % for a blazed grating (6 levels) and rectangular grating, respectively. Under red illumination conditions (λ = 550 - 700 nm) the photocurrent of the blazed grating is increased by 28.5 % and for the rectangular shaped grating by 13.2 % compared to the flat cell value. In the blue light range λ = 300 - 550 nm the blazed grating shows ~ 6 times higher gain in the photocurrent than the rectangular shaped grating, with 12.9 % versus 1.9 % in comparison to a flat structure. The cell with a blazed grating coupler shows an improved light in-coupling and thus reduced reflection for blue and red light but a slightly weaker light trapping ability in the near infrared light region than the rectangular blazed grating. For 400 nm < λ < 430 nm the blazed grating shows a significantly higher *QE* (Fig. 6.6) than the rectangular grating with ΔQE between + 5 % and + 15 %.
A thorough examination of the shape of the *QE* spectra shows a reduction of the 2 strong interference peaks between λ = 400 - 500 nm for a blazed grating in comparison to the rectangular shaped grating. The peak height of the interference fringes depends on the phasing of the light within the individual discrete levels. For a flat structure the interference modulations are the strongest. Interference fringes in the *QE* are observed when the optical thickness of the height of the discrete levels corresponds to a multiple of $\lambda/4$. For other configurations the optical propagation within the discrete levels leads to a different phasing and consequently the two distinct fringes disappear. For blue light illumination the absorption gain is not as pronounced as in Morf's results. This can be likely explained by using different grating parameters *P* and *h* and a 1 µm thick microcrystalline absorber layer compared to a 310 nm thick amorphous silicon layer as in Morf's work that is more sensitive in the blue spectral range.

A reduction of the number of discrete blaze levels from 6 to 3 gives an interesting result. For λ = 300 - 700 nm the 6-level blazed grating leads to higher *QEs* than the 3-level blazed grating due to an improved light in-coupling, but for λ = 700 – 1100 nm the vice versa case occurs *(QE(3-level) > QE(6-level))*. This behaviour indicates a better long wavelength light trapping for the 3-level blazed grating. The calculated blue response of the cell considering a 3-level blaze grating is similar as for cells with rectangular shaped gratings.

This result indicates that light incoupling is mainly determinated by the shape of the texture.

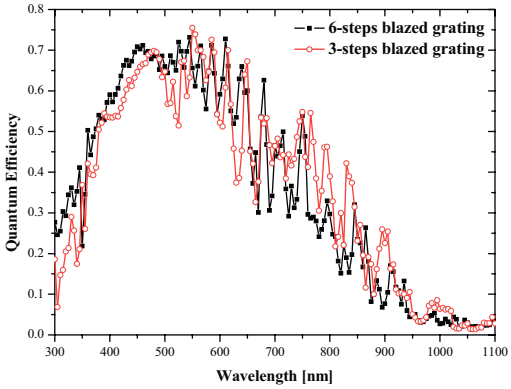

Fig. 6.8: Quantum efficiency of an unsymmetrical, blazed texture with 6- or 3-steps integrated in a thin-film silicon solar cell. The 6-step structure exhibits a better blue light incoupling but a weaker red-light trapping than the 3-step structure.

6.4 Symmetrical 2D structure

To understand the influence of the asymmetry of the blazed structure on the light propagation a truly symmetrical, pyramidal structure was implemented in the unit cell, as shown in Figure 6.9. The layer sequence is in accordance with the previous simulations.

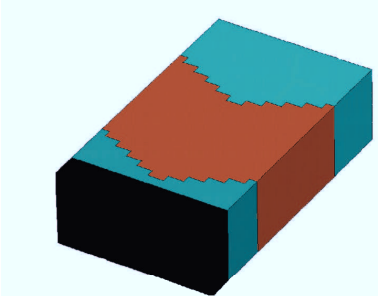

Fig. 6.9: Unit cell of a symmetrical 2D structure.

For the symmetrical 6-step pyramid texture we found an overall gain in J_{sc} of 33.2 %, comprising a gain of the blue response (300 nm < λ < 550 nm) of 13.1 %, the red response (550 nm < λ < 700 nm) 30.6 % and a strong gain of 79.9 % for the near-infrared region (700 nm < λ < 1100 nm) all compared to a flat cell. The short circuit current amounts to 16.9 mA/cm^2. This is a gain of 4.2 mA/cm^2 compared to flat, untextured cell.

Examples for absorption profiles are shown in the following (Fig. 6.10). For λ = 400 nm the absorption takes place in the first ~ 100 nm. At every step of the structure a flame-like region of strong absorption can be found. For the same period and height values a triangular structure was simulated to investigate the absorption profile for short wavelength for different interface features. It turn out that the absorption profile for the flat interface of the triangular structure does not show the separated individual flame-like loss regions. A profile with broad red absorption regions is visible that has a similar intensity distribution in *z*-direction.

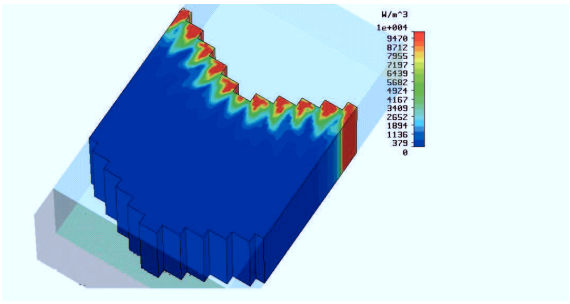

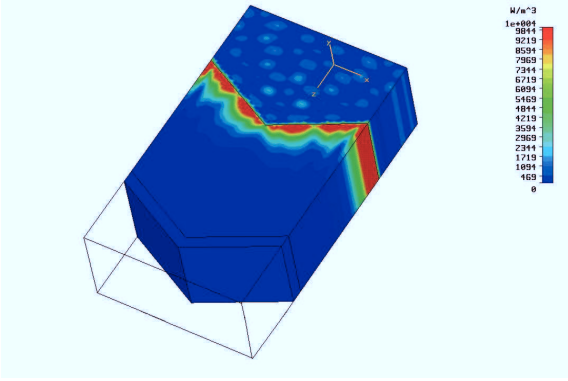

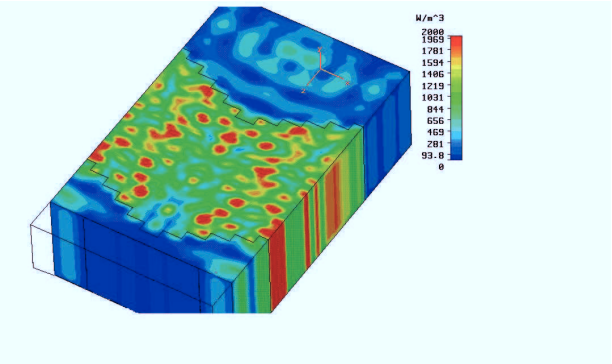

Fig. 6.10: Comparison of absorption profiles for a symmetrical, pyramidal 6-step structure (top) and a pyramidal structure with a flat interface (middle) for λ = 400 nm. In the bottom absorption profile the illumination is performed with λ = 700 nm. The small pyramid steps have a lateral size of 120 nm and a vertical size of 60 nm resulting in a period of P = 1.2 µm and structure height h = 300 nm.

For λ = 700 nm regions of strong absorption (red coloration) are uniformly distributed over the microcrystalline silicon absorber layer.

For the high energy case (400nm) the maximum of absorber power is 35100 W/m^3 for the 6-step pyramidal case and 23207 W/m^3 for the pyramidal structure with flat interfaces. The low energy case (λ = 700 nm) has a maximum in absorption with 3800 W/m^3. For both wavelength the quantum efficiency (*QE = Power (incoming) / Power (absorbed)*) is in the range of 50 %. As the absorption of the blue light mainly takes places in the TCO_{front} / silicon interface region and not like in the red light case distributed all over the absorber layer an advanced discussion and optimization needs also consider the non uniformity of the recombination at the front contact. This is given by the shorter life time for generated carriers in the p-doped layer and at the heterogeneous material interface.

6.5 Multi step pyramids with variation in step size and step number

Next, the influence of the number of steps is investigated for the symmetrical multi-step pyramid. For a constant period size P and structure height h the total step number N leads to the following individual step size of the lateral and vertical steps, following the equations:

$$lateral-step-size = P/((N-1)\cdot 2) \tag{6.4}$$

$$vertical-step-size = h/(N-1) \tag{6.5}$$

For a pyramid with P = 1.2 µm and h = 300 nm the investigated pyramid structures have the following lateral and vertical step-sizes:

number of steps	3-steps	4-steps	5-steps	6-steps
lateral step-size	300 nm	200 nm	150 nm	120 nm
vertical step-size	150 nm	100 nm	75 nm	60 nm

Fig. 6.11 shows the relative gain in J_{sc} of the multi-step pyramid structure in comparison to a flat structure that is dependent on the number of used steps. The rectangular (which is 2-step binary grating) structure and 2D pyramids with 3, 4, 5 and 6 steps are investigated. The spectrum is again divided in 3 region of interest.

For the blue response (300 nm < λ < 550 nm) a very clear trend is visible. The higher the number of steps of the pyramid, the higher is the gain in J_{sc}. This can also be seen for the red response (550 nm < λ < 700 nm) with an exception of the 4-step pyramid. For the near-infrared region (700 nm < λ < 1100 nm) the structure with 4, 5 and step show a high gain of ~ 80 – 90 %. The 3-step structure shows an even lower gain than the binary grating structure.

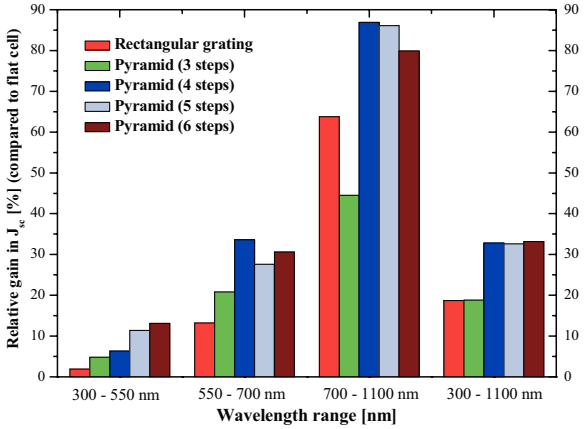

Fig. 6.11: Comparison of relative gain in J_{sc} of cells with a 2D pyramidal multi-step structure with 3, 4, 5 and 6 steps and a rectangular shaped grating. The gain in short circuit current is compared to a flat cell for three different wavelength regions. The multi-step pyramid and the rectangular grating have P = 1.2 µm and h = 0.3 µm.

The general trends can be clearly seen in the illustration. A local interference effect or a shift of a peak within the QE graph from one spectral region into the adjacent spectral region can be the reason for irregularities in the observed results. This local interference effect can be for example introduced by a destructive or constructive interference of the individual diffracted waves that are starting at the small steps. Therefore, the vertical step-size in relation to the wavelength of the incoming wave can be the critical parameter.

The following table summarizes the calculated gain in J_{sc} compared to a flat, untextured design for the three spectral regions.

For all structures the period size is P = 1.2 µm and the structure height h = 300 nm.

Gain in J_{sc} [%] Spectral range	flat design without texture	6 – blaze un-symm. (2D)	3 – blaze un-symm. (2D)	rectangular grating (1D)	6 - step pyra-mid (2D)	5 - step pyra-mid (2D)	4 - step pyra-mid (2D)	3 - step pyra-mid (2D)
300 – 550 nm	0	13	2.9	1.9	13.1	11.4	6.3	4.8
550 – 700 nm	0	28.5	26.9	13.2	30.6	27.6	33.6	20.8
700 – 1100 nm	0	59.4	100.96	63.8	79.9	86.1	86.9	44.5
Total-Gain [%]	**0**	**28.2**	**31.9**	**18.7**	**33.2**	**32.6**	**32.8**	**18.8**
J_{sc} total [mA/cm^2]	12.69	16.27	16.75	15.07	16.90	16.83	16.85	15.08

Tab. 6.1: Gain in current for different spectral regions and structures with the same period and structure height. (P = 1.2 and h = 300 nm).

Next, the step number dependence was investigated for a changed P/*h* ratio.

The period size is P = 0.7 µm and h = 300 nm. For the rectangular grating structure this parameter set exhibited high currents.

Gain in Jsc [%] Spectral range	3 - step pyramid (2D) P = 0.7 µm	4 - step pyramid (2D) P = 0.7 µm	5 - step pyramid (2D) P = 0.7 µm
300 – 550 nm	8.97	10	13.3
550 – 700 nm	26.7	29.7	35.9
700 – 1100 nm	64.9	80.4	84
Total-Gain[%]	**26.9**	**31.6**	**36.1**
J_{sc} total [mA/cm^2]	16.11	16.71	17.27

Tab. 6.2: Gain in current for different spectral regions and structures with 3, 4 and 5-steps with the same period and structure height. (P = 0.7 and h = 300 nm).

The trend that was observed for multi-step pyramids with P = 1.2 µm, h = 300 nm that with increasing number of steps of the pyramid the gain in J_{sc} is higher is also found for the P = 0.7 µm structures. Here, the trend is similarly present in all three wavelength regions.

In Fig. 6.12 the relative gain in J_{sc} compared to a flat cell for the short wavelength region 300 nm < λ < 550 nm is illustrated in relation to the vertical step size. It shows a very similar curve for both period sizes. Both curves show a higher gain for smaller vertical step sizes. For the incoupling process the vertical step size is an important parameter as small steps lead to a smother change in refractive index. The lateral step size also plays a role (lateral step size shown in brackets in Fig. 6.12) as for comparable vertical step size a smaller lateral step always exhibits a higher gain. For comparable lateral steps sizes (120 nm and 117 nm) a smaller vertical step size is beneficial.
Thus the incoming plane wave experiences an antireflection effect that clearly depends on the lateral and vertical size of the used steps.

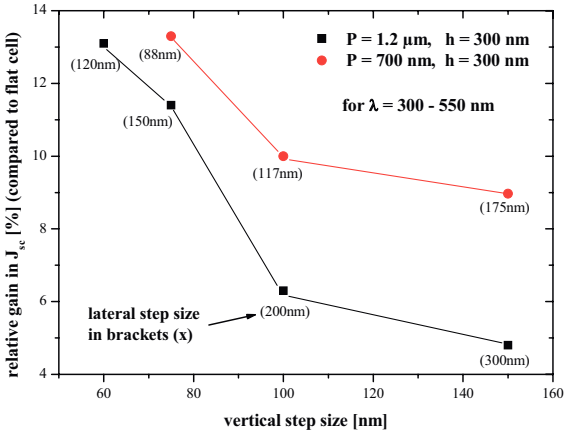

Fig. 6.12: The relative gain in J_{sc} for blue light is shown in relation to the vertical steps size of the structure. For both period sizes P =1.2 µm and 0.7 µm a similar shape is visible indicating the importance of the vertical step size for the light incoupling.

6.6 Investigation of blue light incoupling

To understand the fundamental aspects of light incoupling the *QE* was calculated for a large variety of 2D structures. The period, height and number of steps were varied independently. In the following study period sizes between 500 nm and 2 µm and pyramid heights of 75 nm up to 1 µm were investigated. The resulting opening angle of the pyramid is determined by *P* and *h* lies between 70° and 157°. The step number of the multi-step 2D pyramids was chosen to be 6, 8, 10 or 11. The back reflector design was either conformal shaped TCO/silver or the flat TCO/ silver interface.

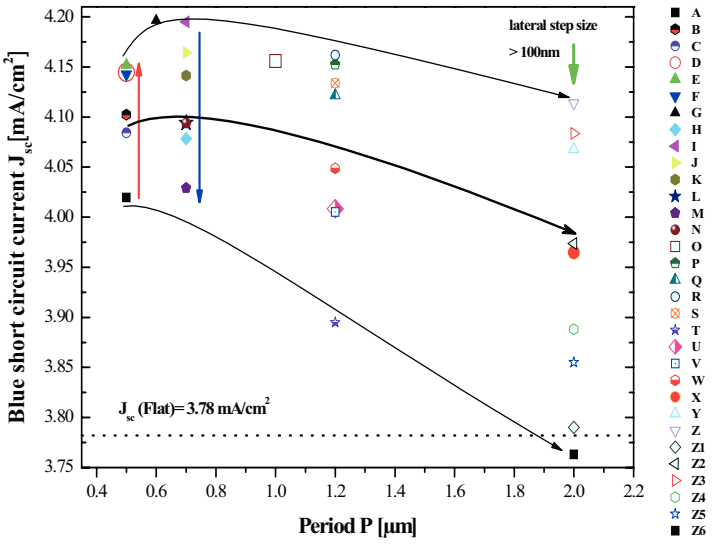

Fig. 6.13: Calculated blue current of 2D multi-step pyramids with a variation in period, structure height, number of steps, opening angle of the pyramid and back reflector design. For small periods < 1 µm and pyramid steps of ~ 30 – 70 nm the highest blue currents were calculated. The sample names and the detailed structure parameters are given in the table below. The dotted line indicates the blue current of a flat, untextured structure.

Although the blue spectrum generates only a short circuit current of around 4 mA/cm^2 it allows to investigate the fundamental properties for the incoupling of light. Figure 6.13 shows the calculated J_{sc} over the period size for the blue spectrum and more than 30 different P and h parameter combinations.

The following observations have been made:

- The general observed trend is indicated by the black arrows. High current values are found for smaller lateral and vertical features (i.e. steps of ~ 30 – 70 nm). With higher total period (and thus larger lateral features with constant step size between 6 and 11) the blue current decreases. The thick black arrow in Fig. 6.13 indicates the average J_{sc}-value and the thin back arrows indicate the spreading of the J_{sc}-values for the given period size. For smaller period size the spreading of data point is much smaller than for larger periods.
- For P = 0.5 µm the samples with a lateral step size of 50 nm show an increase in current with higher vertical step size of 15 nm, 25 nm, 35 nm, 42 nm (samples A, B, C, E, F) (red arrow)
- For P = 0.7 µm all samples have a lateral steps size of 70 nm and they show the highest current value for a vertical steps size of 35 nm and a lower current value for higher or lower vertical step sizes (sample I and J). (blue arrow)
- For P = 1.2 µm the parameter combinations with lateral/vertical steps with: 86nm/43nm, 120nm/35nm, 67nm/33nm and 120nm/60nm show the highest blue currents.
- The samples with P = 2.0 µm do all have lateral step sizes > 100 nm. They also show the highest blue current for small vertical step sizes of 30 nm (sample Z). If the lateral step is too large (200 nm) a small vertical step size of 40 nm doesn't lead to a high current anymore (sample X).
- The highest blue current was calculated for P = 0.6 µm, h = 200 nm and 6 steps with a 60 nm lateral step size and 40 nm vertical step size. The gain in J_{sc} is +10.97 % in comparison to a flat cell.
- The opening angle is not generally correlated to the blue current. Steeper structures are usually better for an enhanced light incoupling but the individual step size is more important than the opening angle. For longer wavelength (red light illumination) this trends would reverse as the small features or step sizes are much smaller than the

incident light. For red light the total structure size or structure angle determines the incoupling properties.

The following table summarizes the structure parameter of each sample in Fig. 6.13 via the sample name. Samples mentioned in the text before are highlighted.

Sample name	Period size P [µm]	Structure height h [nm]	Opening angle [°]	Blue short circuit current J_{sc} [mA/cm^2]	Lateral step size [nm]	Vertical step size [nm]
A	0.5	75	147	**4.02**	**50**	**15**
B	0.5	125	127	**4.10**	**50**	**25**
C	0.5	175	110	**4.14**	**50**	**35**
D	0.5	175	110	4.08	36	25
E	0.5	210	100	**4.15**	**50**	**42**
F	0.5	210	100	**4.14**	**50**	**42**
G	0.6	200	113	4.20	60	40
H	0.7	100	148	4.08	70	20
I	0.7	175	127	**4.19**	**70**	**35**
J	0.7	175	127	**4.16**	**70**	**35**
K	0.7	300	100	4.14	70	60
L	0.7	300	100	4.09	70	60
M	0.7	500	70	4.03	70	100
N	0.7	500	70	4.09	70	71
O	1.2	175	147	4.15	120	35
P	1.2	300	128	4.12	120	60
Q	1.2	300	128	4.16	86	43
R	1.2	300	128	4.13	67	33
S	1.2	500	100	3.89	120	100
T	1.2	500	100	4.01	86	71
U	1.2	500	100	4.01	67	56
V	1.2	600	90	4.05	60	60
W	1.0	300	118	4.16	100	60
X	2.0	200	157	**3.96**	**200**	**40**
Y	2.0	300	147	4.07	200	60
Z	2.0	300	147	**4.11**	**100**	**30**
Z1	2.0	500	127	3.79	200	100
Z2	2.0	500	127	3.97	143	71
Z3	2.0	500	127	4.08	100	50
Z4	2.0	830	100	3.89	200	166
Z5	2.0	830	100	3.85	100	83
Z6	2.0	1000	90	3.76	100	100

Tab. 6.3: The table summarizes the investigated structures for the calculation of the blue response as in Fig. 6.13.

From every individual step of the multi-step pyramid an individual diffracted light wave starts. These individual waves can for a given constellation of incoming light wave and vertical and horizontal step size lead to a local constructive or destructive interference that can supports an improved light incoupling into the absorber layer.

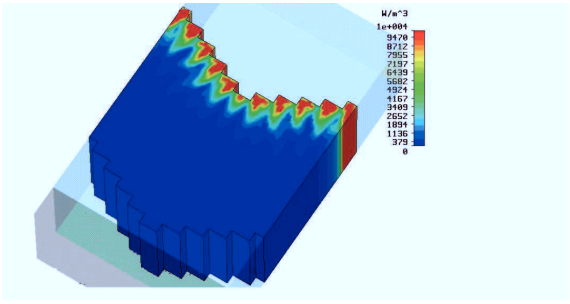

Fig. 6.14: Absorption profiles for a symmetrical, pyramidal 6-step structure for λ = 400 nm. The small pyramid steps have a lateral size of 120 nm and a vertical size of 60 nm resulting in a period of P = 1.2 µm and structure height h = 300 nm. From every step of the pyramid an individual diffracted light wave starts.

General trends observed for the blue response of pyramidal multi-step structures:

1. The ideal feature for a high blue response is a small vertical step size of 30 ~ 50 nm. (With lateral step sizes of 50 – 100 nm). Vertical steps > 60 nm clearly lower the blue response. They lead to a discontinuity of the local (from one step to the other) refractive index gradient.

   A few simulations showed that vertical steps < 30 nm (for the same lateral size) also lead to a lower current if the total structure height of the pyramid is too small (h < 175 nm). This is the consequence of a too abrupt change of the total (over the whole interface regarding the z-axis) refractive index of the structure.
2. The opening angles resulting from P and h for the highest blue response deviate between V = 100°, 118° or 127/128°.
3. The gain in J_{sc} is ~ 10.97 % in comparison to a flat cell (a rectangular grating showed a gain in J_{sc} of only ~ 3 % in comparison to a flat cell).

6.7 Comparison of 2D and 3D light trapping structures

The previous chapters have focused on 1D and 2D periodic light trapping structures. Fundamental properties and design criteria for thin-film silicon solar cells have been found.

However, in comparison to cells with randomly textured substrates the calculated short circuit current of these 2D structures is lower. Therefore, 3D structures, as present in the random concept need to be investigated.

In analogy to the previous 2D calculations the 3D pyramid was discretized by 6 steps. For a 3D pyramid with $P = 0.7\mu m$ and a structure height of 300 nm the QE was calculated for 300 nm < λ < 1100 nm. A comparison to the calculated QE of the 2D pyramid showed an almost identical blue response (300 nm < λ < 500 nm). For λ > 500 nm the 3D pyramidal structure has a significantly higher QE. The short circuit current was calculated to be J_{sc} = 20.45 mA/cm^2 which is 3.5 mA/cm^2 higher than for the corresponding 2D pyramidal structure. This result shows the necessity of a 3D interface texture as it is used in the standard randomly rough texture concept.

The higher current is generated by a prolonged light path in the absorber layer as the light is diffracted in x- and y- direction (for an incidence along the y-axis). For a 2D structure the light was only diffracted in x- direction whereas in y-direction the shortest possible path is possible. Therefore, the 2D structures have a constant absorption profile in y- direction.

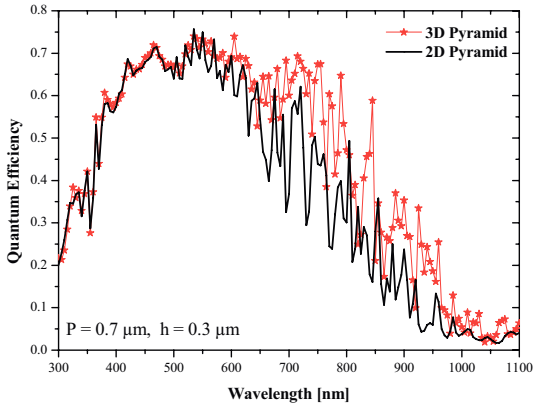

Fig. 6.15: Comparison of the QE of a 2D and 3D pyramidal interface with 6 discretization steps. The blue response is identical and for the 3D pyramid the red response is significantly enhanced.

This result gives an indication why the thin-film µc-Si solar cells with 1D line grating couplers had a red current that was enhanced in comparison to a flat cell but that was not as high as for the random textures.

As for thin-film solar cells based on amorphous silicon mainly the incoupling properties play the important role for this cell type a 2D texture might be sufficient to fulfil the optical requirement. As the total performance of a solar cell is determined by morphological, electrical and optical properties that influence each other strongly a 2D structure with an optimized design might have advantages compared to a 3D texture, in the case of amorphous silicon.

6.8 Comparison of inverted and upright pyramids

The approach of a randomly rough texture used at our institute exhibits predominantly crater-like structures, which can be simplified in a model by inverted pyramids. To understand its functionality a comparison of a solar cell with an inverted pyramid and an upright pyramid is performed by numerical modeling.

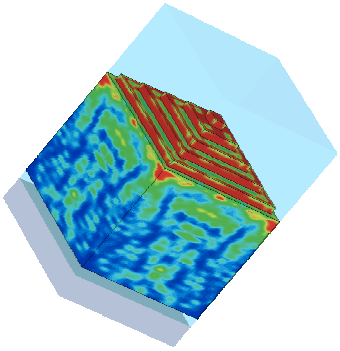

Fig. 6.16: Absorption profile of an upright 6-step pyramid interface texture for λ = 500 nm. The lateral step size is 100 nm the vertical step size is 60 nm. Only the absorption in the silicon layer is shown. The silicon layer has the shape of an upright pyramid. The TCO_{from} layer is coloured in a transparent light blue.

Within the simulations we take care that both structures have the same silicon absorber volume and the same front TCO volume. The calculated *QE* of the upright pyramid is about 5 % higher than for cells with an inverted pyramid structure for a wavelength of 300 nm > λ > 500 nm as shown in Fig. 6.17.

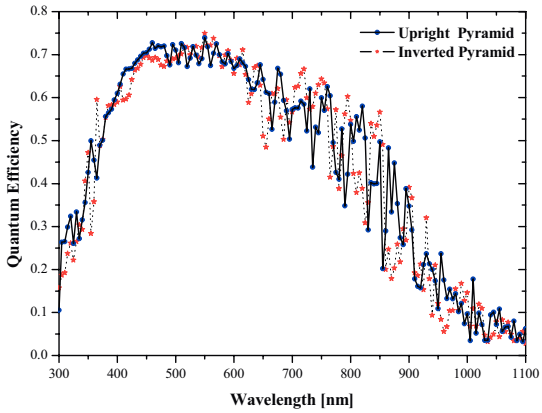

Fig. 6.17: Comparison of inverted and upright pyramidal texture with P = 1.0 µm and h = 300 nm with flat silver back contact. The short circuit current of the inverted and upright pyramid was calculated to be J_{sc} = 20.44 mA/cm^2 and 20.63 mA/cm^2, respectively.

The reason for this might be a higher reflectivity of the inverted-pyramid as the volume fraction of the silicon layer increases (in direction to the back contact) more rapidly. Thus, the incident light propagates through a layer with a stronger change in the effective refraction index n_{eff}, consequently the reflection enhances. The enhanced blue response is in good agreement with the data determined for crystalline silicon cells with a 300 times thicker absorber layer. The lower reflectivity of upright pyramids compared to inverted pyramids was also calculated by Sai et al. [6.3] for infinite crystalline silicon absorbers. For thin-film silicon solar cells only the wavelengths below 500 nm can be considered to be incident on an "infinitely" thick absorber. While for c-Si also an enhanced red response was predicted by the simulation thin-film cells with upright and inverted pyramids show in our simulation comparable values. For any wavelength > 500 nm it is not possible to clearly separate the optical effects of in-coupling, out-coupling and light trapping within the quantum efficiency calculation as they are a superposition of each other. An evaluation of their individual contribution can only be conducted with experiments like for instance a variation of absorber layer thickness or the interface design.

The change of the effective refractive index can be calculated in the following way. For the case of an inverted pyramid structure (as seen from the light incident side) the pyramid is filled with TCO.

$$n_{eff}(z) = \frac{P(z)^2}{P^2} \cdot n_{TCO} + \frac{(P^2 - P(z)^2)}{P^2} \cdot n_{Si} \tag{6.6}$$

This equation calculates the refractive index of the pyramid at the position z, see Fig.6.18.

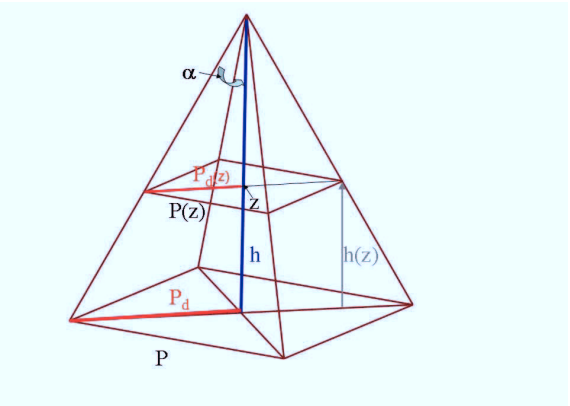

Fig. 6.18: Sketch of a pyramid used for the calculation of the effective refractive index of an inverted TCO pyramid interface between the TCO_{front} and silicon layer.

For a point z close to the pyramid base the area given by $P(z)^2$ is almost as big as the pyramid base (P^2) and the effective refractive index $n_{eff}(z)$ is dominated by the pyramid material (in this case TCO). For a point z close to the pyramid tip the material outside of the pyramid (here the surrounding silicon) gives the main contribution to $n_{eff}(z)$.

With the Pythagorean Theorem the following relations are given:

$$P^2 = P_d^{\,2} + P_d^{\,2} \tag{6.7}$$

$$P^2(z) = P_d^{\,2}(z) + P_d^{\,2}(z) \tag{6.8}$$

$$P = P_d \cdot \sqrt{2} \tag{6.9}$$

$$P(z) = P_d(z) \cdot \sqrt{2} \tag{6.10}$$

Via the angle α at the pyramid tip the equation is given:

$$\tan\alpha = \frac{P_d}{h} = \frac{P_d(z)}{h(z)} \tag{6.11}$$

This leads to

$$n_{eff}(z) = \frac{h(z)^2}{h^2} \cdot n_{TCO} + \left(\frac{h^2 - h(z)^2}{h^2}\right) \cdot n_{Si} \tag{6.12}$$

$$h(z) = h - z \tag{6.13}$$

$$n_{eff}(z) = \frac{(h-z)^2}{h^2} \cdot n_{TCO} + \left(1 - \frac{(h-z)^2}{h^2}\right) \cdot n_{Si} \tag{6.14}$$

Next, the effective refractive index is plotted for the wavelength dependent materials TCO and silicon ($n_{TCO}(\lambda)$ and $n_{Si}(\lambda)$) for blue and red light with λ = 400 nm and λ = 900 nm, respectively. For blue light the difference in n of silicon and TCO is much larger than for red light and thus a smooth change of n is more important for the reduction of reflection. The case of an upright silicon pyramid can be derived as above. For both wavelengths this n_{eff} curve is much flatter at the start of the pyramid and much steeper at the end.

Both structures (inverted or upright, as in Fig 6.19) have the same refractive index value at their start and their end. This is not the important fact, though. The shape of the structure determines whether the slope of the curve in Fig. 6.20 at the start of the interface texture (here a pyramid) is smooth or steep and thus reflecting less or more, respectively.

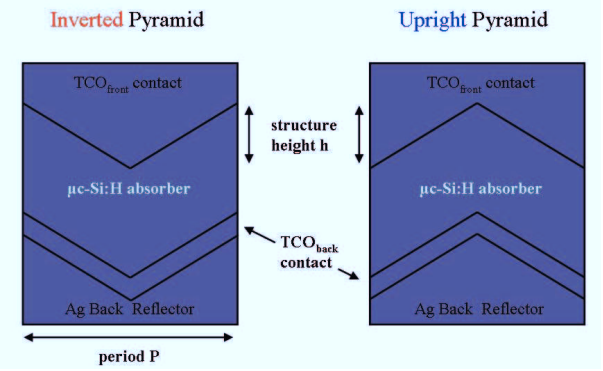

Fig. 6.19: Scheme of inverted and upright pyramid configuration.

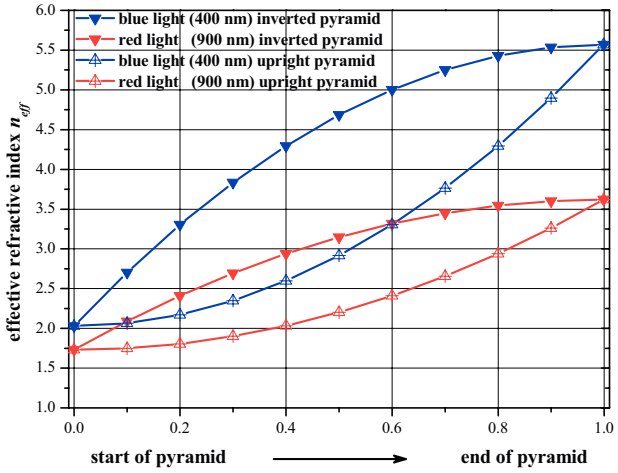

Fig. 6.20: The effective refractive index of a pyramidal interface between TCO and silicon in upright or inverted configuration is plotted from the start of the pyramid to its end for blue light (λ = 400 nm) and red light (λ = 900 nm) illumination. The inverted TCO pyramid leads to steeper slope of the curve at the start of the pyramid and the consequence is a stronger reflection and a lower QE in the Maxwell simulation.

6.9 Influence of back contact design on short circuit current

Next, we investigate the influence of the back contact design on the optical properties of the device. The common thin film solar cell developed at our institute has an 80 nm thick TCO_{back} layer made of ZnO followed by a sputtered silver back contact. The TCO_{back} layer is sputtered on the silicon layer and has a conformal shape with a roughness similar to the absorber layer. Our studies have shown that this is the preferable back contact design in terms of electrical properties and damp heat and high temperature stability [6.4]. In this numerical study the standard back contact concept was compared to a back contact with a flat interface between the TCO_{back} layer and the silver layer. The short circuit currents for both device designs is calculated for period sizes from 0.5 µm to 1.2 µm and absorber layer thicknesses of 1µm,

1.5µm and 2µm. For a period size of P = 0.7µm (where for 2D structures good red light trapping was achieved) the short circuit current of cells with flat back contact design is about 2.5 mA/cm^2 higher than for structures with the conformal back contact design independent of the i-layer thickness investigated.

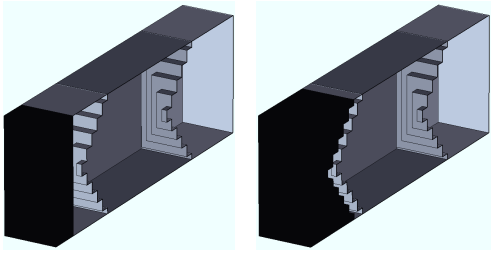

Fig. 6.21: Cross-section scheme of a thin-film silicon solar cell with 3D pyramid texture. A back contact with a flat interface between the silver and TCO back layer (left) and a conformably shaped TCO and silver back layer (right) are investigated.

In case of a 1µm thick absorber the difference in current of both structures decreases with increasing period size. For the conformably shaped back contact structure cell J_{sc} increases and the J_{sc} value of the flat shaped interface cell remains on a high level (> 20 mA/cm^2). The blue response (300 nm > λ > 500 nm) of both shapes is identical and equals J_{sc} ~ 4.3 mA/cm^2 independent of the period size (see Fig. 6.22). Both shapes were also tested with different absorber layer thicknesses of 1.5 µm and 2 µm. For P = 0.7 µm and P = 1.2 µm the relative gain in J_{sc} through the flat back interface remains nearly constant.

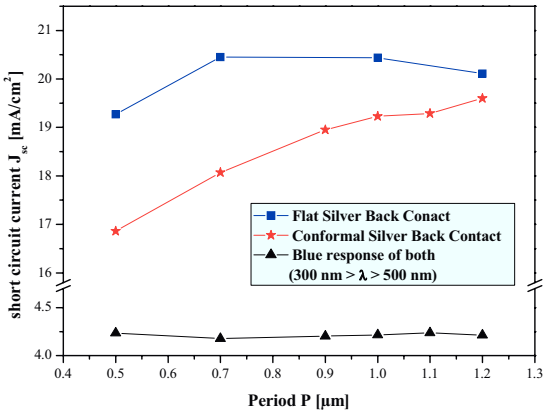

Fig. 6.22: Short circuit current of cells with different back contact designs (Fig. 6.21). Additionally, the blue response is shown, which is identical for both structures. The structure height is h = 300 nm.

A gain of 1 - 1.5 mA/cm^2 and 2.5 - 3 mA/cm^2 in case of increasing the absorber layer thickness from 1 µm to 1.5 µm and from 1 µm to 2 µm thick absorber layers, respectively, is observed for the structure with a flat back contact design. This result indicates that the difference in current of both structures can be explained by the influence of the back contact design on the light propagation within the structures. The higher J_{sc} values for the flat back contact design cell can be attributed to an improved light trapping, likely caused by an optical retardation of the light rays after passing through the inhomogeneous thick TCO_{back} layer. For both devices the incoupling angles at the front side are the same but the angles of diffraction after the first transition through the cell must have been beneficially altered in case of the flat back contact design and a stronger waveguide effect is supported. The conformal TCO_{back} layer structure is more sensitive to the period size and a period size around 1.2 µm seems to be necessary to reach high J_{sc} -values.

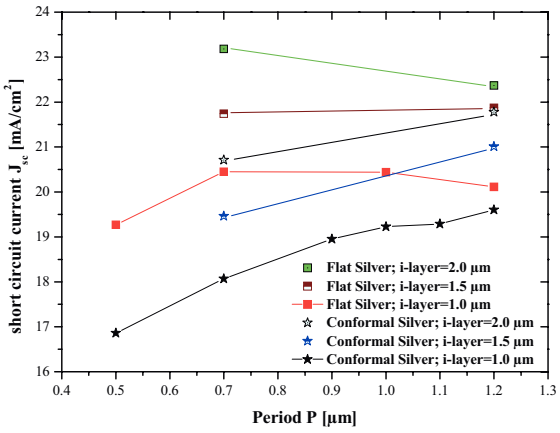

Fig. 6.23: Short circuit current for different back contact designs (as shown in Fig. 6.21) for silicon absorber layer thicknesses of d = 1 µm, 1.5 µm and 2 µm. The structure height is h = 300 nm.

In addition to the improved light trapping of the structure with the flat silver back reflector it is generally recognized that a macroscopic roughness of the silver back reflector can lead to significant absorption losses in the visible range due to interference-enhanced plasmonic absorption effects [6.5]. This effect is not considered within the simulations as an ideal metal (Ag) layer was implemented in the model. Thus, a flat silver back reflector might have potential to increase the overall light trapping properties of thin film silicon solar cells.

References Chapter 6:

[6.1] R. Morf and J. Gobrecht, Optimized structures for light trapping, Proceedings of the 10th Workshop on Quantum Solar Energy Conversion - (QUANTSOL'98), March 8-14, 1998, Bad Hofgastein, Austria

[6.2] Optik, Eugene Hecht, Oldenbourg Verlag, 1999

[6.3] H. Sai, K. Tsuji, H. Fujii, K. Arafune, Y. Ohshita, Y. Kanamori, H. Yugami, and M. Yamaguchi, Toyota Technological Insititute, Anti-Reflective Subwavelength Structures for Crystalline-Si Solar Cells Fabricated by Porous Alumina Mask and Fast Atom Beam Etching, 15th International Photovoltaic Science & Engineering Conference (PVSEC-15) Shanghai China 2005
[6.4] H. Stiebig, W. Reetz, C. Haase, T. Repmann, and B. Rech, Stability of non-encapsulated thin-film silicon solar cells in damp heat tests, 15th International Photovoltaic Science & Engineering Conference (PVSEC-15) Shanghai China 2005
[6.5] Stiebig H, Kreisel A, Winz K, Schultz N, Beneking C, Eickhoff Th, Wagner H, Meer M., Proceedings of the 1st World Conference on Photovoltaic Energy Conversion, Hawaii, 1994; 603–606.

7 Investigation of inverted pyramids

7.1 Three dimensional square based pyramids with flat interfaces

In the previous chapter comparable high blue currents were calculated for square based, 6, 8, 10, 11-step pyramids with period size between 400 nm and 700 nm. But also for a period size of 2 µm (with structure height of 300 nm and a higher number of 11 pyramid steps) a high blue response was found.
These results lead to the conclusion that the lateral and vertical distance between the individual pyramid steps can result in destructive or constructive interferences.
Consequently, the short circuit current is depending on more parameters than in the line grating case (1D line grating*:* $J_{sc} = J_{sc}(P, h)$. The short circuit current of a multi-step pyramid depends on 4 parameters: $J_{sc} = J_{sc}(P, h, dx, dy)$ with dx and dy denoting the size of the small steps of the multi-step pyramid in lateral (dx) and vertical (dy) direction.

In chapter 7 square based pyramids with flat interfaces are investigated instead of the multi-step pyramid.

For the flat silver / TCO interface design in Fig. 7.1 the distance between the silicon pyramid tip and the silver layer is 80 nm and the maximum TCO_{back} layer thickness is 80 nm + h.

It is also possible to calculate and plot the spatial absorption profile within a 2D cutting layer in the cell, as shown in Fig. 7.1. For λ = 400 nm the spatial absorption profile is plotted in a xy-cutting plane in the middle of the absorber layer. The 4 symmetric peaks are “modes” that are determined by the optical confinement of the cell design.

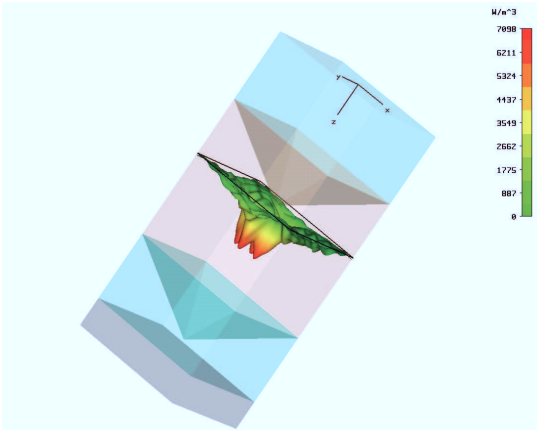

Fig. 7.1: Power loss profile for illumination with λ = 400 nm is plotted in a xy-cutting plane in the middle of the absorber layer. The 4 symmetric peaks, red areas of strong absorption represent "modes" that are determined by the optical confinement of the cell design.

The *QE* and absorption in the TCO layers is shown in Fig. 7.2 calculated for a pyramid with parameters P = 850 nm and h = 400 nm and a flat silver / TCO back reflector design. For this structure the calculated current is J_{sc} = 21.02 mA/cm^2.

This value is in the range of experimental values determined for cells with 1µm thick microcrystalline silicon absorber layers and deposited on randomly textured substrates.
The parasitic absorption of the TCO_{front} layer remains in the wavelength range λ = 500 - 900 nm on a high level of ~7 %. Increasing the transparency of the TCO layer is thus of great importance to reach higher photocurrents.

In the *QE* calculation the whole silicon absorber layer is considered. In all simulation results presented in this thesis higher defect densities in the p - and n - doped layers are neglected.

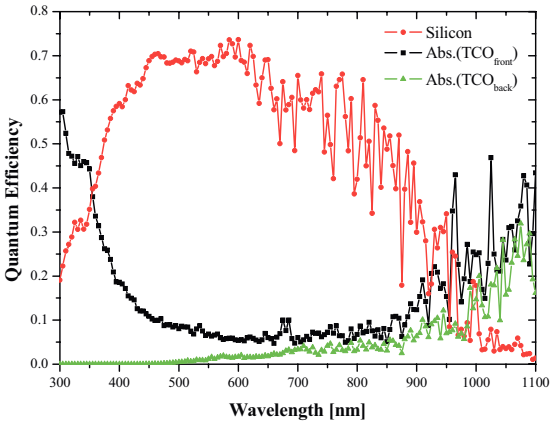

Fig 7.2: Calculated QE of the silicon layer and absorption in the front and back TCO layers of a 3D inverted square based pyramid. The highest short circuit current J_{sc} = 21.02 mA/cm^2 was calculated for P = 850 nm and h = 400 nm.

In this study a variation of *P* and *h* of the 3D pyramid is performed and the results are plotted as a function of the period P or the pyramid opening angle α. In the notation of the previous multi-step pyramid study the flat pyramid interfaces have an $N \sim \infty$.

Again, for 300 nm < λ < 1100 nm the unit cell is illuminated with a circular polarized plane wave, which enters under normal incidence. The calculated J_{sc} values are the maximum possible short circuit current density. A *QE* value below one implies that the incident radiation has not been completely absorbed within the photovoltaic active region. It can be reflected at the front side of the cell, absorbed in the TCO_{front} or TCO_{back} layer or it might have escaped from the cell after multiple reflections within the cell. Especially for $\lambda > 620$ nm, the absorption coefficient *a* multiplied with the layer thickness *d* is $a * d < 1$. Thus light has to be multiple reflected within the cell until it is absorbed. Considering the sun spectrum and the calculated *QE*, J_{sc} can be calculated. Fig. 7.3 shows the calculated J_{sc} of cells with textured substrates in comparison to a flat, untextured structure as a function of *P* (right axis).

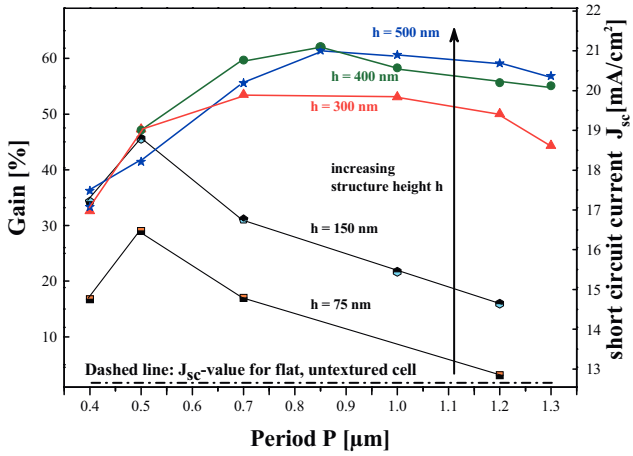

Fig. 7.3: Calculated J_{sc} of cells with square based pyramids for a variation of P and h in comparison to a flat, untextured structure (Gain = 0 %). For structure height h > 300 nm high currents are calculated. The results are determined for the flat back reflector design as shown in Fig. 7.1.

The following parameters were used within the simulation: P = 400 nm – 1300 nm, h = 75 nm – 500 nm and the resulting pyramid opening angle α = 44° – 166°. The J_{sc} curves for h = 300 nm, 400 nm and 500 nm show similar high current values with a broad maximum for P = 700 – 1000 nm. For lower periods J_{sc} strongly decreases and a weaker decrease in J_{sc} is observed for P above 1000 nm. The highest values were calculated for P = 850 nm and h = 400 nm. The short circuit current of J_{sc} = 21.03 mA/cm^2 shows a gain of + 62 % compared to an untextured device with an absorber thickness = 1 µm (left axis). For h = 75 and 150 nm and P > 500 nm J_{sc} is strongly reduced due to the insufficient light trapping and light scattering properties of these structures.

7.2 Investigation of pyramid opening angles

To analyse the effect of light trapping, light incoupling and their superposition two parts of the sun spectrum are discussed in the following (spec.1 = 300 – 500 nm, spec.2 = 700 – 1100 nm). Due to the small penetration depth for blue light, a light trapping effect is negligible for spec.1. Although the total amount of J_{sc} generated by spec. 1 is only in the range of 4 mA/cm^2, it is the spectral part that allows for identifying the principle of light incoupling into the device. The calculated J_{sc} using spec. 1 is plotted in iso-lines (same structure heights) as a function of α (Fig. 7.4).

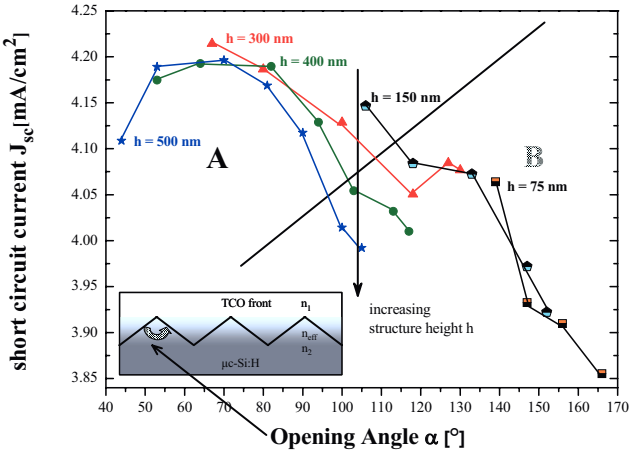

Fig. 7.4: Calculation of the optimum opening angle of the pyramid structure for an ideal incoupling of the blue spectrum. The ideal opening angle of the pyramid is $\alpha \sim 53° - 82°$.

The highest values are reached for small angles ($53° < \alpha < 82°$) and h = 300 – 500 nm, denoted as region **A**. Steep structures result in a high blue response as observed in concepts with naturally rough grown ZnO [7.1]. For a fixed $\alpha \sim 100°$ the blue response decreases with increasing lateral structure sizes, as indicated by the arrow in Fig. 7.4. With increasing lateral structure size the optical properties of the interface change from improved light incoupling due to effective refractive index matching to the regime where bulk optical properties prevail.

For light with shorter wavelength (spec.1) the light incoupling properties of the cell mainly determines J_{sc}. According to the effective refractive index grading approach a complex geometrical structure with materials of different refractive indices can be approximately described by an effective refractive index n_{eff}. An interface reflection is in general reduced by a continuous change in refractive index. The insert in Fig. 7.4 shows, simplified to 2D, the principle change in refractive index that is introduced by the pyramids. Large P leads to a discontinuous lateral intermixing of the two refractive indices and the plane wave is thus reflected by a more abrupt change in n. Region **B** has in relation to the incident waves too large period sizes that inhibit a good light incoupling.

The front TCO also leads to absorption losses. To enable the lateral current flow the TCO is comprised by a 500 nm thick flat layer and a textured region with inverted pyramids. Caused by this approach, the absorption losses within the TCO_{front} contact should be more pronounced for TCOs with higher h. The front contact layer absorbs at least 5 % and even up to 50 % for 300 nm < λ < 400 nm. The integration of a larger TCO pyramid with h = 300 – 500 nm (for P = 0.7 µm) would result in a decrease of the J_{sc} by about ~ -0.1 mA/cm^2 in comparison to a small pyramid with h = 75 nm and P = 0.7 µm. However, this increased parasitic absorption is over-compensated by the improved incoupling properties of the optimized texture. A total gain in J_{sc} of ~ +0.4 mA/cm^2 is found.

In Fig. 7.5 the red response is plotted with regard to the opening angle α. The curves for h = 300, 400, 500 nm have a similar shape. The J_{sc} maximum is shifted to smaller angles for higher h. For h = 75, 300, 400 and 500 nm it is at around 147 - 156°, 100 - 127°, 90 - 103° and 81 - 100°, respectively. A broad distribution of high values of J_{sc} = 6.8 – 7.7 mA/cm^2 is generally found for angles between 70 - 113° and h = 400 nm and 500 nm. The iso-lines for the same structure height have for increasing α a similar decrease in J_{sc} as the resulting angles of diffraction are getting too small. The light is not diffracted ideally into the silicon layer. The chance for an escape of the light from the structure is high and the desired waveguide effect is not efficient. For decreasing α no efficient light trapping occurs as the propagation of higher order modes is not supported. Structures with h = 75 nm and 150 nm are in general too small to induce a sufficient diffraction for long wavelength light and consequently their light trapping potential is low.

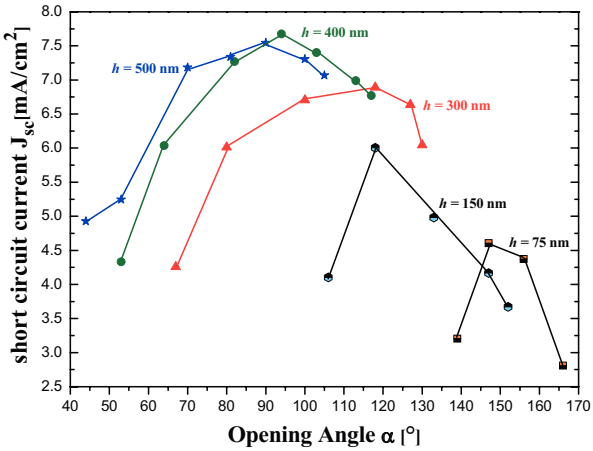

Fig. 7.5: Calculation of the red current for a solar cell with a pyramid structure over the opening angle of the pyramid. The ideal opening angle of the pyramid is $\alpha \sim 90°$.

The presented data corresponds to a back contact that has a flat silver / TCO_{back} interface. Previous studies have shown that this back contact system exhibits a higher red light trapping potential than a conformal interface, especially for small periods. The optimum for incoupling and light trapping occurs at different angles. This results in a relative broad maximum for the choice of texture parameters with good optical properties which are also influenced by the scattering and reflection properties of the back contact. Within the simulations an ideal metal back contact was considered. In conclusion, light trapping can be to a certain extend insensitive to slight changes in α, h and P. In contrast to conventional gratings and macro optical devices the investigated sub-wavelength gratings/structures perform more consistently over a broader range of wavelengths than conventional gratings.

In Fig. 7.6 the spatial absorption profile within a 2D cutting layer in the solar cell is shown for a variation of the z-position of the xy-cutting plane. The illustrated absorption profiles of a single wavelength (λ = 400 nm) represent the spectrum used in Fig. 7.4. The red areas are regions with a high power loss. The formation of mode-like regions of high absorption is symmetrical with regard to the z-axis. Such spatial information about the 3D distribution of

the power loss profile can be extremely valuable in the design of thin-film solar cells. Being able to control the texture shape and thus the distribution of high absorption areas it might be possible to avoid that a high generation rate is concentrated in areas with a high recombination rate, like the defect-rich p- and n-doped layers or areas with a low electrostatic field (valleys), which determines the carrier collection.

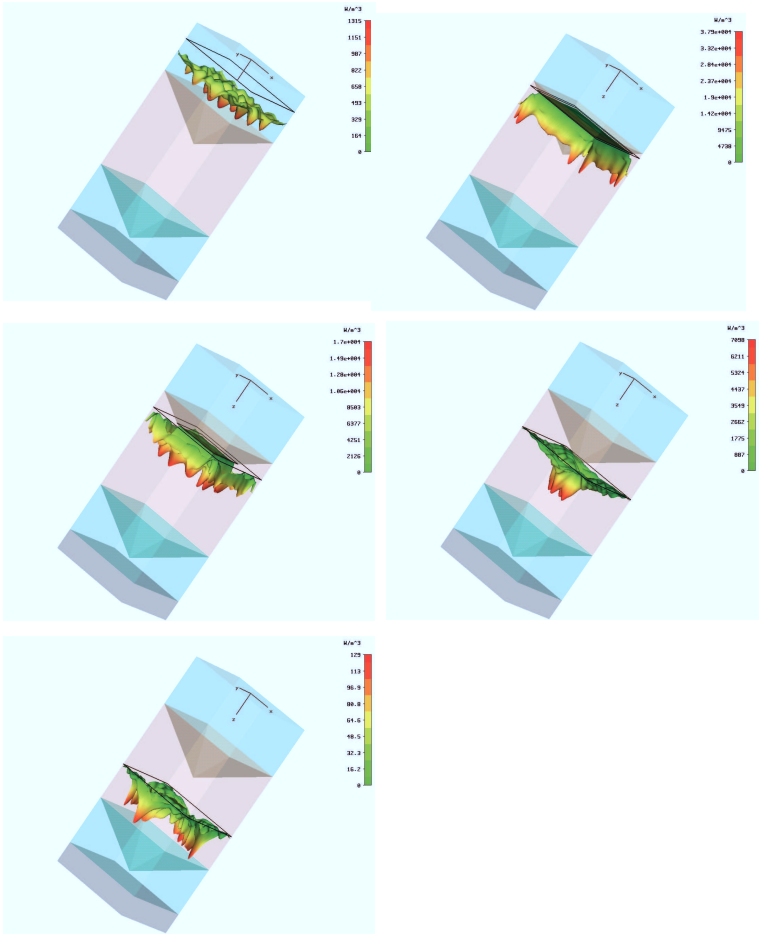

Fig. 7.6: Projection of the power loss profile in a xy-plane at different z-positions within the thin-film silicon solar cell for λ = 400 nm. The red areas are regions with a strong

absorption. For this high energy blue light the main absorption takes place in the front part of the absorber layer. The maximum of the scale is normalized to the peak intensity for visibility reasons.

In addition, microcrystalline material is not a homogenous material but a mixture of amorphous silicon and columnar grown silicon crystallites with different carrier lifetimes. In all our calculations a homogeneous absorber and TCO material is parameterized by the optical constants. However, for a study that also considers the electric inhomogeneities the presented power loss profiles and their spatial distributions must be intensively investigated for all wavelengths.

7.3 Limit estimation and comparison to established limit theories

The theoretical maximum cell current density for λ = 650 – 1100 nm was determined by Tiedje et al. [7.2] (using the idealized Yablonovitch light trapping-limit) to be 16.8 mA/cm^2. Vanecek et al. [7.3] calculated a limit of 14.0 mA/cm^2 considering nearly idealized conditions such as AR coating, high TCO_{front} transparency, Lambertian scattering and high back contact reflectivity. The cell current determined for the presented periodic structures (P = 0.85 µm, h = 400 nm) for λ = 650 – 1100 nm is J_{sc} = 10.0 mA/cm^2. However, this structure exhibits strong TCO_{front} and TCO_{back} absorption losses in the range of 5.8 mA/cm^2. Increasing the optical transparency of the TCO layers has in conclusion a great potential to substantially increase the cell current. Within our simulations we do not consider a glass sheet. Thus the entering plane wave experiences an abrupt change from n_{Air} to n_{TCO} instead of a smoother change in refractive index with the glass sheet present. Therefore, the overall reflectivity of our unit cell is approximately 5 % too high. We estimate the maximum current that can be reached by the presented periodic light trapping structures to be J_{sc}^{max} = 1.05 * (10.0 mA/cm^2 + 5.8 mA/cm^2) = 16.6 mA/cm^2. This is close to the Tiedje limit and above the value determined by Vanecek. A fine tuning of P, h and the structure shape in addition to the use of AR coatings could lead to even higher values.

The good agreement between these simulations, investigated prototypes with periodic line grating texture and our experience with various random texture designs proves the reliability and versatility of the performed Maxwell simulations.

This numerical 3D analysis of a periodic pyramid texture gives clear design criteria for efficient light incoupling and light trapping textures. For this investigated solar cell design the

periodic structure has to be in the range of P = 0.7 – 1.2 µm, h = 300 – 500 nm and pyramid opening angles α = 60 - 130°, respectively.

7.4 Comparison of 6-step pyramid and flat pyramid

The following table lists the calculated short circuit currents of a 6-step pyramid in comparison to a pyramid with flat interfaces for the same period size and structure height parameters. The 6-step pyramid always shows a current that is ~ (0.6 – 0.8) mA/cm^2 higher than for flat pyramid interfaces. This difference might originate from a) a different light trapping property and/or b) from the influence of the meshing used in the simulation. The mesh cells are hexahedral and for flat pyramid interfaces an intersection of the meshcells takes place that can influence the result.

Structure parameters:	P = 0.7 µm h = 0.3 µm	P = 1.0 µm h = 0.3 µm	P = 1.2 µm h = 0.3 µm
6-step pyramid	20.45 mA/cm^2	20.44 mA/cm^2	20.11 mA/cm^2
flat pyramid	19.83 mA/cm^2	19.77 mA/cm^2	19.35 mA/cm^2
difference	0.62 mA/cm^2	0.67 mA/cm^2	0.76 mA/cm^2

Tab. 7.1: Comparison of current between a 6-step and a flat interface

7.5 Comparison of different back reflector designs

In addition to the parameters period size P and pyramid height h, the assembly of the back reflector is of great importance for the light trapping. The first assembly in Fig. 7.7 (left) has a flat interface between the TCO and the silver layer. The second assembly in Fig. 7.7 (right) has a conformal 80 nm thin layer of TCO in between the silicon and the silver back contact. In general the back reflector has a strong influence to the optical properties. If an electromagnetic wave is travelling in a medium with a lower refractive index like silicon or TCO and then is incident on a larger refractive index medium like a metal (silver) this always leads to wave node of the electric and magnetic fields at the metal layer. This is comparable to the classical analogy of wave node that is present at the fixed end of the string of a musical instrument. The smaller refractive index of TCO in comparison to silicon leads in case of a

large angle of incidence to a total reflection and a trapping of the light within the silicon layer. Both assemblies use the principle of total reflection at the TCO to silicon interface but a have a different reflection behavior due to the shape of the silver layer.

The common assembly in industrial concepts consists of 80 nm thick conformably shaped TCO layer. This design is the consequence of a quasi-conformal deposition of thin-films. Both designs correspond to the structures in the multi-step pyramid investigation. The base thickness of the front TCO was kept to 500 nm comparable to previous studies with line gratings and other structures. The absorber layer consists of a 1 µm thick microcrystalline silicon layer.

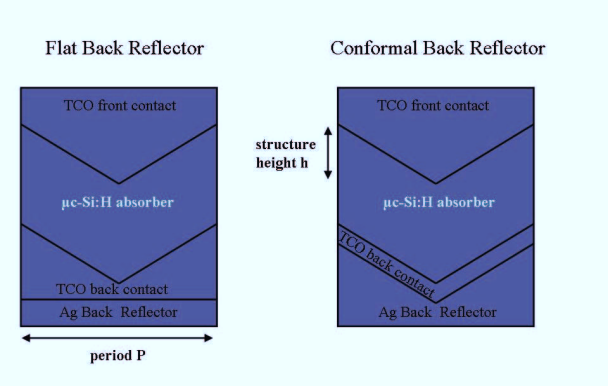

Fig. 7.7: Scheme of the simulation unit cell of a pyramid texture with a conformal back reflector design. For visibility reasons the 3D calculation unit cell is projected to 2D.

For the short wavelength range $\lambda \sim 300$ - 500 nm the *QE* for the conformal back reflector design is identical to the *QE* of the flat silver TCO_{back} interface. Fig. 7.8 and Fig. 7.9 show spatial absorption profiles within lateral or vertical cross section planes. Fig. 7.8 shows the appearance of a strong absorption mode within the front TCO layer localized under the pyramid tip. In Fig. 7.9 the absorption profile within a vertical cross section is illustrated. A diffraction pattern with a strong absorption area in the centre is visible.

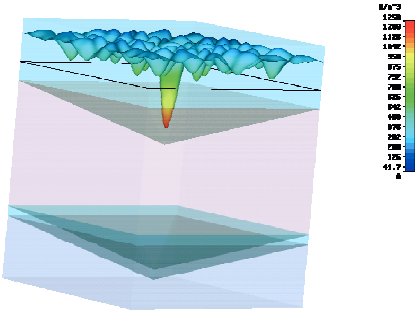

Fig. 7.8: The absorption profile shows the appearance of a strong absorption mode within the TCO layer that is confined by the square based pyramid directly below the pyramid tip. The simulation parameters are P = 1.7 µm, h = 400 nm and λ = 500 nm.

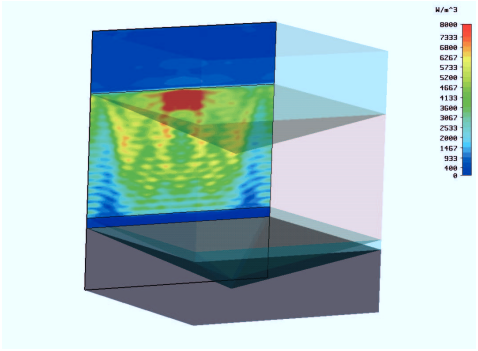

Fig. 7.9: Calculated absorption in the xz-cutting plane. The red colour is an area of strong absorption. Parameters are chosen as in Fig. 7.8.

Information about the spatial distribution of the power loss profile can be extremely valuable in the design of thin-film solar cells. Being able to control the structure and the consequent distribution of high absorption areas it might be possible to avoid that a high generation rate is concentrated in areas with a high recombination rate, like the defect rich p- and n-doped layers or areas with a low electrostatic field (valleys), which determines the carrier collection [7.4]. In addition, microcrystalline material is not a homogenous material but a mixture of

amorphous silicon and columnar grown silicon crystallites with different carrier lifetimes. However, for a study that also considers the electric inhomogeneities the presented power loss profiles and their spatial distributions must be intensively investigated for all wavelengths.

Fig. 7.10 shows the period size dependence of J_{sc} of the two investigated back reflector designs for a structure height h = 400 nm. The conformal shaped reflector design has its maximum in J_{sc} for P = 1.7 µm. The flat reflector design has its optimum in J_{sc} at P = 0.85 µm.

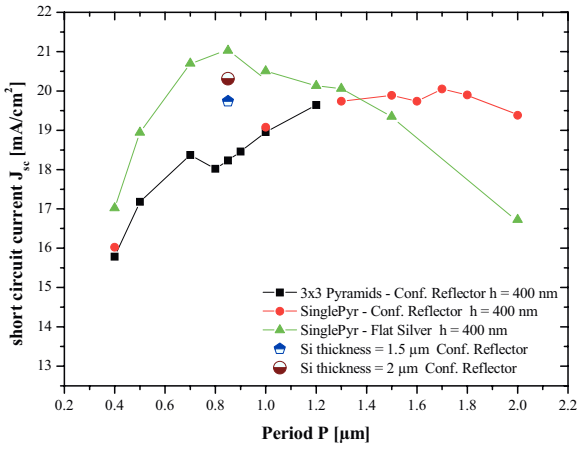

Fig. 7.10: Comparison of short circuit current depending on the period size for h = 400 nm and two back reflector designs. For the blue and brown symbol the absorber layer thickness was increased to 1.5 µm and 2.0 µm. The red and black symbols are a comparison of a single to multi-pyramid unit cell.

From P = 0.4 µm – 0.7 µm the increase in current of both structures is similar. Afterwards for the conformal structure the current increases further to its maximum. The slope of the curve shows a quite broad peak/plateau, whereas the slope of the flat reflector exhibits a sharp maximum and then a quite linear decay. For the chosen period scale both curves have a clear trend without a strong scattering. This can be explained with the broad spectrum that is incident on the solar cell.

An increase of the absorber layer thickness (for the case of the conformal reflector type) from 1 µm to 1.5 µm or 2 µm, indicated by the blue or the brown data point in Fig. 7.10, respectively, enhances the J_{sc} value but the high value (J_{sc} ~ 21 mA/cm^2) of the flat reflector design was not reached. This result indicates the importance of back reflector design for the wave propagation within the structure and consequently on the light trapping properties of the device. A thinner absorber layer with an optimized light trapping structure can be a superior solar cell than a cell with a thicker absorber layer and a not optimized light trapping texture.

In Fig. 7.11 the *QE* of both peaks of the two different back reflector systems of Fig. 7.10 is shown. The structure P = 0.85 µm with the flat back reflector has for 500 nm < λ < 650 nm a 5 % higher *QE* than the P = 1.8 µm pyramid with the conformal reflector. This is due to the better blue incoupling properties of steeper structure, as investigated before. For λ < 650 nm the average of both *QE* curves is quite comparable. The diffraction and scattering properties of both structures lead to an equivalent light trapping.

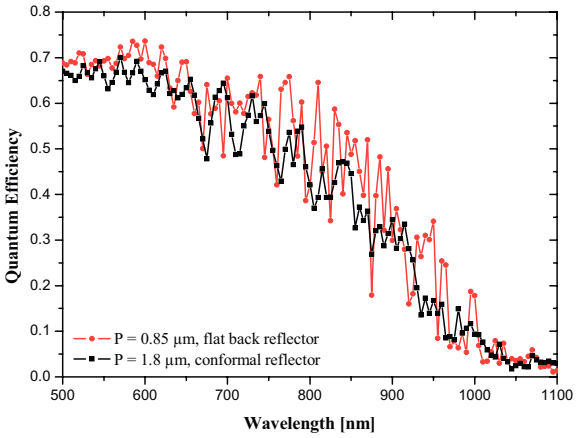

Fig. 7.11: The two structures with the highest short circuit current in Fig. 7.10 and their corresponding quantum efficiencies are displayed. For λ > 650 nm the average of both QE curves is comparable but for λ < 650 nm the incoupling properties of steeper structures lead to higher QE values.

For a waveguide or antenna array with a single or sharp spectral selectivity the design parameters are generally much more critically. A broad range of period sizes, as present in random textures, seems therefore, in a first conclusion, to be suitable for light trapping. But our study is only valid for a periodic unit cell with the investigated period sizes and not a composition of a individual varying period sizes.

In general this investigation shows the sensitiveness of the light propagation and trapping on the back reflector system. ***A development of light trapping textures and TCOs must be adapted to the properties of the back reflector***. For a random TCO structure it is likely that a texture with a large amount of light being diffracted at the front TCO needs a rather flat back reflector that maintains the generated diffraction angles. For a strong diffraction at the front TCO the presence of a strongly scattering back reflector might lead to en enhanced out coupling of the light. This is evident for a conformal back reflector and $P < 1.2$ µm.

7.6 Comparison of single pyramid unit cell and multiple pyramid unit cell simulation

In the testing phase of the simulation tool a small error was detected for a very small unit cells. A flat solar cell stack showed for a single wavelength and a small unit cell period $P <$ 0.2 µm not the same absorption results as for a wide unit cell with $P > 1$ µm (results not shown in detail). This tendency is more pronounced for larger wavelength ($\lambda > 900$ nm) than for smaller wavelength as the total propagation path through the calculation domain increases for longer wavelengths. With this experiment in mind and the plan to replace the unit cell composed of single periodic pyramids by a larger unit cell with pyramids of varying period size the following experiment was conducted: For $P = 0.4$ µm and $P = 1.0$ µm a single pyramid was compared to a 3 x 3 array of pyramids. In Fig. 7.10 the red circle symbol indicates that a unit cell with a single pyramid was used. The black square symbol indicates that a 3 x 3 array of single pyramids was used as unit cell. Both simulations are set up in a periodic simulation unit cell (either with one or 3 x 3 = 9 single pyramids inside). As expected, only for the small period $P = 0.4$ µm a little deviation in J_{sc} was found. For $P = 1$ µm both data point are almost equivalent.

In Fig. 7.11 the absorption profile for a structure with P = 850 nm and h = 400 nm and a 2 µm thick absorber layer is shown. The usual absorber thickness is *d (Si)* = 1 µm. The absorber layer thickness was increased to visualize the formation of absorption peaks (modes) that are not disturbed by the influence of the back reflector (this is only the case for λ = 500 nm, though.) For all investigated wavelength (λ = 500 nm (top), 600 nm (middle) and 890 nm (bottom)) the main absorption peaks are centred above the pyramid tips and above the pyramid centres. The main modes are quite similar and at the same position within the absorber layer independent of the wavelength.

The difference between the profile for λ = 500 nm and λ = 600 nm is that the strong (red) absorption modes are not continuous in direction of the back reflector. This can be explained with the investigations made with the flat solar cell that shows the appearance of in direction of light incidence alternating maxima and minima due to constructive interference of incoming wave and waves that have been reflected at the back contact. Therefore, the profiles in Fig. 7.11 show the presence of a light that is still travelling with the original (vertical) direction of incidence.

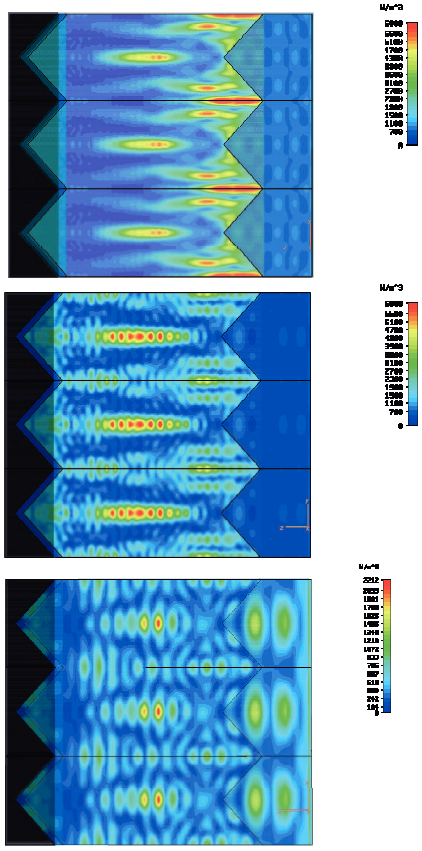

Fig. 7.12 a, b, c: The power absorption profiles are shown for a 3 x 3 pyramid array and conformal back reflector design. The thickness of the absorber layer was increased to 2 μm in order to identify the incoupling properties (modes) for λ = 500 nm (top). Below are the absorption profiles for λ = 600 nm (middle) and λ = 890 nm (bottom). The period size is P = 850 nm and the structure height h = 400 nm. The top and middle profiles are normalized to the same power density (6000 W /m^3). The bottom profile is normalized to 2212 W / m^3.

7.7 Investigation of cone type structure

A 1D (rectangular grating) or 2D (multistep-2D pyramid) structure only leads to diffraction of light along one axis that is perpendicular to the direction of incidence (*z*-axis). The absorption profile along the other axis remains constant. The change from a 2D to a 3D pyramid structure results in a strongly enhanced red light trapping. This was explained by a diffraction along the *x*- axis AND also the *y*-axis.

For a square based pyramid the incident plane wave is only diffracted in 4 preferential directions. A cone shaped structure with a circular base could due to its rotation symmetry, in theory, enable many (radial) directions for diffraction, which might be beneficial for the light trapping properties.

To investigate the optical potential of a cone shaped structure, it was integrated in the unit cell, as shown in Fig. 7.13. The parameters *P, h* and also the opening angle α remain the same as for the pyramid. The setup of the computational unit cell is based on a periodic system with planar sides. It is not easy to simulate a single periodic unit cell with a cone structure without having flat interface parts.

The ratio of textured cone interface to texture interface area is:

Interface area (Cone) / square unit cell area (Pyramid base)

$$= \pi (P/2)^2 / (P^2) = 1/4\pi \approx 0.785 \qquad (7.1)$$

This means for the simulation that about 21.5 % percent of the interface between the silicon and the TCO_{front} layer is a flat, untextured area that can enhance the reflection.

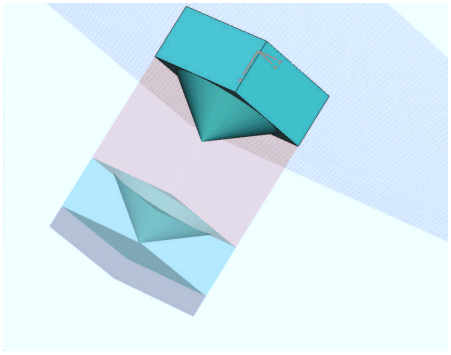

Fig. 7.13: A cone shape is integrated instead of a square based pyramid in the simulation unit cell.

A simulation of a solar cell with a cone structure was performed and the *QE* was compared to the simulation of a 6-step pyramid structure with the same parameters *P, h* and a flat back reflector design. The 6-step pyramid was taken as a reference instead of a flat pyramid as it was calculated with exactly the same meshing, stability factor and settings of the Maxwell solver. Generally, the changes in solver settings lead to small changes of the *QE* spectrum. Within one parameter study the settings are retained as much as possible.

The difference between the J_{sc} of a 6-step pyramid and a pyramid with flat interfaces is < 0.5 mA/cm^2.

Both structure show similar trends but due to the use of differing model settings the difference in quantum efficiency has to be neglected.

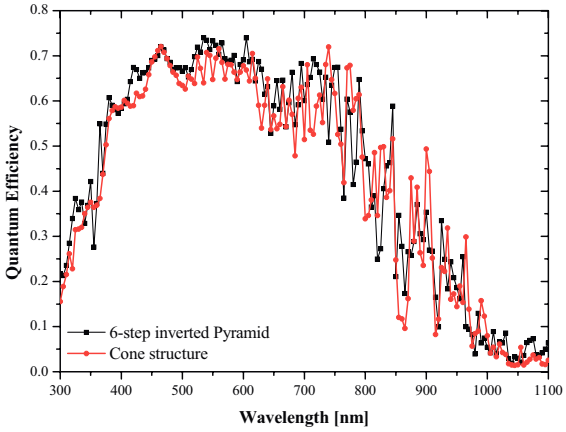

Fig. 7.14: Calculated quantum efficiency of a cone structure and a 6-step pyramid. Both structures have P = 0.7 µm and h = 300 nm and a flat silver back reflector design.

The cone structure has lower *QE* values for almost all wavelengths $\lambda < 750$ nm. For $\lambda > 750$ nm the *QE* spectrum is quite similar. The calculated J_{sc} = 19.75 mA/cm^2 is – 0.71 mA/cm^2 lower than for the comparable 6-step pyramid.

The reflectance of a flat TCO / silicon interface (with the light being incident perpendicular from the TCO side) for short wavelength (λ = 400 nm) is $R \sim 22$ %. As for longer

wavelengths (λ = 900 nm) R is reduced to R ~ 12 % the large amount of flat interface area (21.5 %) in the cone structure makes a stronger impact in the short wavelength region.

Next, a variation in the period size was performed for a constant h = 300 nm. The short circuit current of the cone is compared to the 6-step pyramid and the pyramid with flat interfaces. Both pyramid structures show the same trend in J_{sc} for increasing period size, i.e. a small decrease in J_{sc} for P = 1.2 µm (see Fig. 7.14). For the Cone structure a larger P leads to a strongly reduced current. For P = 1.2 µm the current of the cone structure is reduced by ~ 3 mA/cm^2 in comparison to the pyramid structures. For a higher h = 400 nm a similar strong gain in J_{sc} of ~ 1 mA/cm^2 is visible for the cone and the pyramid structure.

The amount of flat, untextured interface remains unchanged independent of P. So this cannot be the reason for the strongly reduced J_{sc} of the cone structure for increasing periods. The gradient of the refractive index in the direction of light incidence is also the same but the lateral intermixing of the two materials is disrupted at the flat interface parts in the case of the cone structure and this is more pronounced as the lateral dimensions become larger (P increases).

Structure parameters:	P = 0.7 µm h = 0.3 µm	P = 1.0 µm h = 0.3 µm	P = 1.2 µm h = 0.3 µm	P = 1.2 µm h = 0.4 µm
Cone: J_{sc}	19.75 mA/cm^2	18.24 mA/cm^2	16.85 mA/cm^2	17.90 mA/cm^2
6-step pyramid	20.45 mA/cm^2	20.44 mA/cm^2	20.11 mA/cm^2	
pyramid	19.83 mA/cm^2	19.77 mA/cm^2	19.35 mA/cm^2	20.14 mA/cm^2

Tab. 7.1: Comparison of current between a 6-step pyramid and a pyramid with flat interfaces and a cone structure.

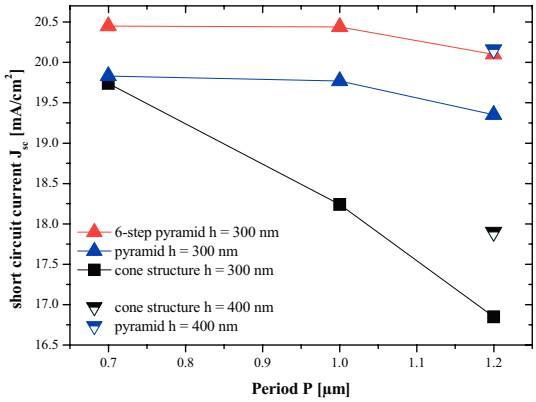

Fig. 7.15: Short circuit current of a cone structure is compared to a 6-step pyramid and a pyramid with flat interfaces. The current of the cone structure suffers from a strong decrease for increasing period sizes.

References Chapter 7

[7.1] A. Shah, H. Schade, M. Vanecek, J. Meier, E. Vallat-Sauvain, Progress in Photovoltaics 2004; 12(2-3): 113–142

[7.2] T. Tiedje, E. Yablonovitch, G. D. Cody, B. G. Brooks, IEEE Trans. Electron Devices 31, 711, (1984)

[7.3] M. Vanecek et al., Proceedings of the Third WCPEC, Osaka, Japan (IEEE, New York, 2003), Vol. B, p. 1527

[7.4] J. Zimmer, H. Stiebig, H. Wagner, Proceedings of the 2nd World Conference on Photovoltaic Solar Energy Conversion, Vienna, 1998; 944.

8 Photonic Crystals as possible band filters

A photonic crystal (PC) consists of periodically structured dielectric materials that influence the propagation of electromagnetic waves through them if the incident wavelength is in the order of the periodicity of the structure [8.1-2]. A PC is often called a photonic bandgap (PBG) material as the existence of an optical bandgap inhibits the propagation of light of specific frequencies. This is in analogy to an electrical band structure in semiconductors and PCs have "optical semiconductor" properties.

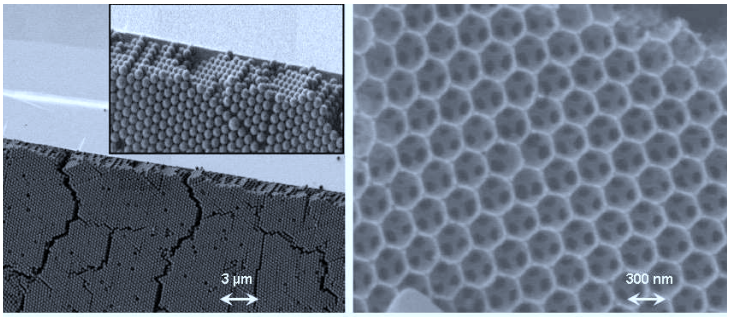

Fig. 8.1: SEM micrographs of a 3D opal template made of PMMA. Fabricated as a thin film on a silicon wafer (left); and an inverted replica made of TiO_2 with higher magnification (right). Such self-organized opal samples often appear in the close packed (fcc) structure. The template images show the appearance of drying cracks and defects at the samples surface. Photographs reprinted from Bielawny et al. [8.3].

In nature there are colourful examples for PC structures such as cristobalit opals, bird feathers or butterflies. For telecommunication the unique optical properties are considered to make novel devices possible. Proposed or already realized on lab scale are waveguides with a curvature radius that lies in the micrometer range, perfect dielectric mirrors, optical chips for high speed optical computers, filters, multiplexer and other optoelectronic devices. An example for a 3D opal template made of PMMA (left) and an inverted replica made of TiO_2 (right) can be seen in Fig. 8.1. Simple 2D and 3D structures can be made by high resolution lithography. For commercial applications self-organizing structures are of great interest. They don't require time consuming lithography process steps and are much easier and less expensive in production. To predict the optical bandgap behaviour for PC structures their

dispersion relation for light propagation can be calculated by several numerical methods [8.3]. In the spectral region of the photonic band gap the density of states is zero. The propagation of light in the plane of structure periodicity with these frequencies is forbidden for a photonic crystal. A simple method for the experimental verification of the existence of this predicted photonic bandgap would be a transmission measurement along this prohibited direction of light propagation.

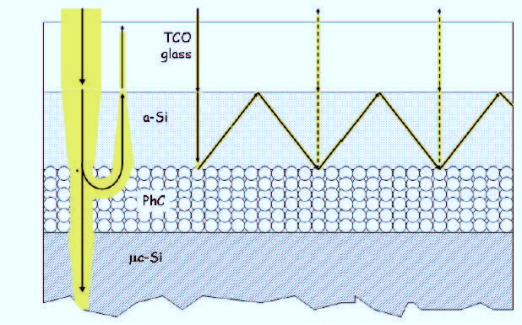

Fig. 8.2: schematic layer concept of a 3D photonic crystal for thin-film silicon tandem cells and expected optical path inside the a-Si:H layer. The zero order is reflected back into the top cell, first order of diffraction backscatters into the top cell (left) internal reflection keeps light inside the high-index silicon layer, surrounded by low-index materials (substrate glass and the PC. Reprinted from [8.3].

As proposed by Bielawny et al. [8.3] a 3D PC structure is currently investigated as intermediate reflector layer for thin-film silicon tandem solar cells. By adjusting the lattice constant the optical properties are supposed to be matched to a silicon tandem structure. The layer is supposed to be energy selective and diffractive and enhance the pathway of incident light within an amorphous silicon top cell. The amorphous top cell suffers strongly from the Staebler-Wronski effect and therefore needs to be as thin as possible.

For the region of spectral overlap of $\lambda = 580 – 700$ nm of a tandem silicon solar cell, photons need to be absorbed in the amorphous cell, which leads to an increase in the short-circuit current of the current limiting top cell. From their simulations they expect a current increase of +1.44 mA/cm² for an amorphous/microcrystalline silicon tandem cell. This is in the range of the increase of top cell current by the integration of intermediate TCO layers in the simulation study of [8.4]. The reflectance spectrum in Fig. 8.3 shows a strong reflection of

around 90 % in the wavelength range of 580 – 700 nm. A second reflectance peak is located at 800 nm. This is the part of the spectrum that needs to be absorbed in the bottom cell! The PC introduces a large angle of diffraction for wavelength between 500 nm and 800 nm. The desired internal reflection is thus satisfied. The integration of PC structures in tandem solar cells has, so far not been demonstrated on the lab scale. Single 3D spherical PC layers have been fabricated with several techniques but they have a high number of defects.

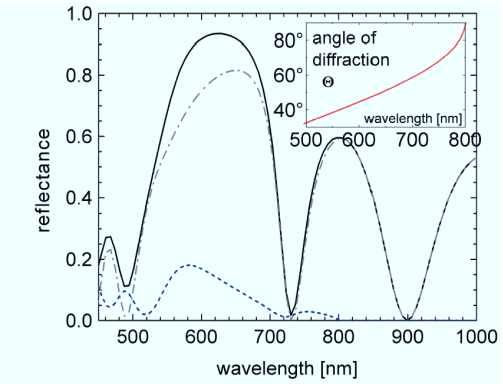

Fig. 8.3: The reflectance spectrum of the PBG material is shown and the angle of diffraction for the first orders: the diffraction angle remains above 30°, even for short wavelengths, and is thus sufficient for total internal reflection. Reprinted from [1.9].

We consider the integration of 3D spherical photonic crystal structures in thin-film silicon solar cells not to be easy on the near tear-time scale, due to the following reasons:

Problems that are possibly occurring for photonic crystals as intermediate reflector layers in tandem concepts:

1. Simulations are performed for ideal / defect free pc and consequently the band filter properties are not as sharp as calculated but have a smoother shape. Most 3D PC have a lattice error every 10 spheres
2. It is not clear if a pc can be tuned to ideally have ~ 90 – 100 % reflectance in the wavelength range of λ = 580 – 700 nm and additionally a very high transmission of ~ 80 –

100 % for λ = 700 - 1100 nm. So far additional reflectance peaks in this region have always been present.

3. Present concepts proposed spheres of ~ 250 nm. Thus a whole PC layer with ~ 10 spheres layers would be thicker than 2.5 µm. This is in the range of the absorber layer thickness and the optical behaviour of the complete layer stack will differ significantly from previously established optimizations.
4. An additional layer can change the damp-heat and high temperature degradation behaviour of the cell with massive consequences for all solar cell parameters.
5. For damp-heat treatments it is known that non compact layers, as present at the edges of sputtered, quasi porous Ag back contact layers suffer significantly from decomposition by water. Several connected stacking faults can therefore, lead to the intrusion of water (humidity) inside the solar cell.
6. The intermediate layer needs to be conducting. This is proposed to be realized by the integration of conductive channels within the PC. At the position where such a conductive channel is integrated in the PC the optical band gap properties are probably disadvantageous altered.
7. If the PC spheres are filled with air (low cost dip coating (assembling) process under normal atmosphere) an in-diffusion of gas species, especially hydrogen, from the spheres into the electrically active solar cell layers can be a consequence that might lead to the degradation of cell performance. A thorough investigation by effusion of gas species from PC spheres into the cell needs to be performed.
8. For PC spheres filled with high quality vacuum or other inert, high purity gases the specific gas environment for this process step needs to be provided.
9. The optical band gap structure is strongly dependent on the direction of light incidence on the pc. Thus, the band filter function will be drastically reduced or even completely lost for light that is not within the acceptance angle of the PC like diffuse light.
10. A flat interface between the glass substrate and the front TCO leads to strong reflection due to an abrupt change of the refractive index.
11. Any additional layer in the solar cell requires another process step that must be justified in terms of benefit for the cell properties in economical relation to process costs, process time and process compatibly.

References Chapter 8

[8.1] E. Yablonovitch, Physical Review Letters, **58**, 2059 (1987).

[8.2] S. John, Physical Review Letters, **58**, 2486 (1987).

[8.3] A. Bielawny, P. T. Miclea, R. B. Wehrspohn, A. von Rhein, C. Rockstuhl, Proceedings of SPIE, **6651**, 665106 (2007).

[8.4] P. Obermeyer, C. Haase, H. Stiebig, Appl. Phys. Letters **92**, 181102 (2008).

9 Quasi Random light trapping structures

All commercial thin-film silicon solar cell concepts today make use of a randomly rough TCO. The main advantage of this concept is the generation of a higher photocurrent with rough structures than with flat structures.

To understand the difference of the optical properties between a periodic and a random structure the following simulation was conducted. Instead of a periodic structure the unit cell consists of a combination of 17 individual pyramids with 8 different period sizes. This unsymmetrical unit cell was calculated with periodic boundary condition as used for the periodic (symmetrical and single) pyramid structures before. This way the simulation of an infinite solar cell is pretended. Different period sizes with the same structure height provide a distribution of opening angles within the structure as present in random textures. The total unit cell area A of

$$A = 3.02\ \mu m \times 3.02\ \mu m = 9.1204\ \mu m^2$$

and

$$A = 4.228\ \mu m \times 4.228\ \mu m = 17.88\ \mu m^2$$

was simulated for this quasi random structure. Between some of the pyramids small gaps with flat interface texture are located. They account up to only 6.3 % of the total area. To fit the pyramids into the unit cell area, there is a very small, in comparison to the total texture area, negligible overlap between some pyramids.

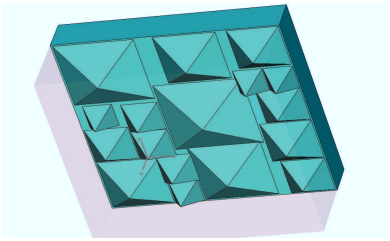

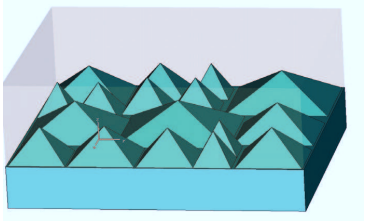

Fig. 9.1 (left): Top view of the Quasi-Random structure with a distribution of different period sizes. The period size varies between P = 0.4 µm - 1.2 µm. The pyramid structure height in this illustration is for all pyramids uniformly set to h = 400 nm.

Fig. 9.2 (right): Side view of Quasi-Random structure.

Fig. 9.1 and 9.2 in combination with Table 9.1 give all relevant information about the number of pyramids, their period size, the distribution and the percentage of the total area that each pyramid size covers. For period size of 1 µm, 1.1 µm and 1.2 µm only one pyramid is integrated in the structure. For smaller period sizes up to 4 pyramids are used.

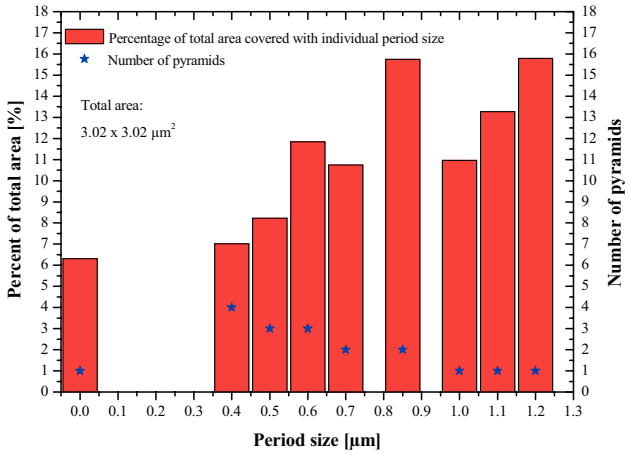

Table 9.1: The illustration shows the percentage of the total texture area that is covered by each individual pyramid period size. The total area of the unit cell is ~ 9 µm².

The position of the pyramids within the simulation unit cell is chosen arbitrarily. A local concentration of periods of the same or a similar size is avoided. Also, a preferential direction of the structure, i.e. an alignment of small or big pyramids along an axis, is not intended. The period size and number of pyramids for each period size is chosen to cover more than 90 % of the total area with a pyramid texture.

Due to the volume of the unit cell and especially the asymmetry of the quasi random structure the computation time is increasing significantly in comparison to single pyramid cell stacks or 3x3 multi pyramid cell arrays. For the used computer hard and software system this quasi random unit cell system with the size dimensions of the computational domain as given above is the limit of complexness for the performed simulations.

Table 9.2 summarizes the period size distribution of the integrated pyramids. Period sizes between 0.4 µm and 1.2 µm and for simplicity reasons a uniform structure height of 400nm are used. This parameter range covers the period size values of interest as investigated for the case of the periodic pyramid structure. For the flat back reflector design within this period size range the maximum short circuit current was found.

Quasi Random Structure:

Period Size P_i [µm]	Area of each period size: $P_i^2 \times N$ [µm^2]	Total Area A [µm^2]	Number of pyramids N	Percentage $(P_i^2 \times N)/ A$ [%]	Pyramid height h [nm]	Opening Angle [°]
flat part	0.5754	9.1204	-	6.31	400	-
0.4	0.64		4	7.02		53
0.5	0.75		3	8.22		64
0.6	1.08		3	11.84		74
0.7	0.98		2	10.75		82
0.85	1.445		2	15.74		94
1	1		1	10.96		103
1.1	1.21		1	13.27		108
1.2	1.44		1	15.79		113

Tab. 9.2: Data of the Quasi Random structure.

For each period size the percentage of the total area that one or more pyramids of this individual period size cover is calculated. The percentage varies between 7 % and 15.8 %. For simplicity reasons the first calculations were set up for a period size distribution with a uniform pyramid height h = 400 nm.

Table 9.3 summarizes the data given above and gives for each period size the short circuit current that was calculated for the single periodic pyramid structure. For the case of a flat back contact design and a pyramid height of h = 400 nm the short circuit currents have been calculated for a complete set of period sizes as for this structure height promising high J_{sc} values have been found.

To verify if a random structure can be described by a superposition of the optical properties of the individual pyramids the area weighted J_{sc} of the quasi random structure is calculated. This approach would allow developing a very simple design rule to estimate the light trapping quality of a thin-film solar cell texture.

The ***area weighted short circuit current*** is calculated with the following formula:

$$J_{sc}^{\,area-weighted} = \sum_i P_i \times N / A_{total} \times J_{sc}(P_i) + A_{flat} / A_{total} \times J_{sc}^{\,flat} \tag{9.1}$$

The number of pyramids N, the percentage that each pyramid size covers with total area ($P_i \times N/A(total)$) and the short circuit currents of the periodic pyramids $J_{sc}\ (P_i)$ are given in the following table.

Flat Silver Back Reflector, uniform pyramid height h = 400 nm:

Period Size P_i [µm]	Percentage $(P_i^2 \times N) / A$ [%]	Number of pyramids N	Short circuit current of single periodic pyramid $J_{sc}(P_i)$ [mA/cm^2]	Area weighted J_{sc} of period structure [mA/cm^2]
flat part	6.31	-	13.0	19.51
0.4	7.02	4	17.018	
0.5	8.22	3	18.945	
0.6	11.84	3	19.291	
0.7	10.75	2	20.699	
0.85	15.74	2	21.025	
1	10.96	1	20.50	
1.1	13.27	1	20.296	
1.2	15.79	1	20.13	

Tab. 9.3: Current calculated for the periodic pyramid design and the area weighted current of the Quasi Random structure.

The area weighted short circuit current calculated with the formula (8.1) and the quasi random structure as described by Tab. 9.3 gives a J_{sc} = 19.51 mA/cm^2.

The calculated quantum efficiency for the quasi random texture and a uniform h = 400 nm is shown in Fig. 9.4. The short circuit current J_{sc} = 16.04 mA/cm^2 is calculated for λ = 500 nm – 1100 nm. For simplicity reasons the blue current was estimated with ~ 4.1 mA/cm^2 as the blue response of the investigated quasi random structure is expected to be a superposition of the blue response of the individual pyramids as it is mainly depending on the incoupling properties of the texture. At the boundary of the base of two pyramids the incoupling properties might be altered (in comparison to a periodic texture) as different period sizes lead to a different side steepness of the pyramid. Therefore, the formation of propagating modes is changed as the interface texture is the boundary condition for the formation of the electromagnetic modes. But for a distribution of pyramid sizes and different neighbouring pyramids this effect might equal out. For these reasons the calculations of a quasi random structure are performed for λ > 500 nm to focus on the important light trapping properties of the thin-film silicon solar cell.

A total J_{sc} = 20.14 mA/cm^2 is calculated. The blue current was estimated from the periodic pyramid approach as pyramids with h = 400 nm show for the investigated period sizes J_{sc} values between 4.0 mA/cm^2 and 4.2 mA/cm^2.

Thus, the simulation of the quasi random structure leads to a short-circuit current that is 0.63 mA/cm^2 higher than the one estimated by the area weighted single pyramid J_{sc} calculation.

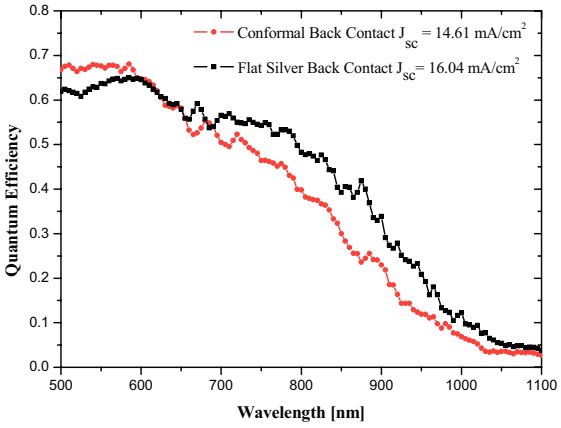

Fig. 9.3: QE of Quasi Random structure with both back reflector types with h = 400 nm.

For the conformal back reflector design the above procedure is repeated and a short circuit current J_{sc} = 14.61 mA/cm^2 is calculated for λ = 500 nm – 1100 nm. Again an estimated blue current of ~ 4.1 mA/cm^2 is added leading to a J_{sc} = 18.71 mA/cm^2. The *QE* of this structure can be found in Fig. 9.3. The current calculated by the area weighted single periodic pyramids is J_{sc} = 18.03 mA/cm^2 and thus 0.68 mA/cm^2 lower than the simulated quasi random structure.

Conformal Silver Back Reflector, uniform pyramid height h = 400 nm:

Period Size P [µm]	Percentage $P_i^2 \times N / A$ [%]	Number of pyramids N	Short circuit current of periodic (J_{sc}) [mA/cm^2]	Area weighted J_{sc} of period structure [mA/cm^2]
0	6.31	1	13.0	18.03
0.4	7.02	4	15.785	
0.5	8.22	3	17.183	
0.6	11.84	3	17.776 (Interpol.)	
0.7	10.75	2	18.370	
0.85	15.74	2	18.229	
1	10.96	1	18.954	
1.1	13.27	1	19.287 (Interpol.)	
1.2	15.79	1	19.642	

Tab. 9.4: Current calculated in the periodic pyramid design and the defined area weighted J_{sc} of the Quasi Random structure.

A very similar difference between calculated current and the area weighted current value is observed for both back reflector designs. Whether the superposition of individual texture features and their optical properties can be used to assess the optical properties of every structure needs to be tested with several structure morphologies. In the two investigated cases the differently sized features of the quasi random structure add between 0.63 mA/cm^2 (flat back reflector design) and 0.68 mA/cm^2 (conformal back reflector design) compared to the super positioned currents of the single pyramid structure.

The quasi random structure shows like in the single periodic pyramid case, that a flat back reflector design is beneficial for light trapping. The flat back reflector design leads to a significantly (plus ~1.5 mA/cm^2) higher J_{sc}.

The absorption in the front TCO for both back reflector designs amounts to 7 % up to a wavelength λ = 800 nm. For increasing wavelength the absorption in the front TCO of the flat reflector design case is significantly enhanced (5-10 %) compared to the conformal reflector design. For λ = 1100 nm both front TCOs absorb more than 30 %. The much higher volume of the back TCO in the flat reflector design absorbs up to 15 %, whereas the 80 nm thick conformal back TCO only absorbs up to 7 % for λ = 1100 nm. The higher absorption in the silicon and the TCO layers is in conclusion an indicator for a better light guiding in the whole layer stack. The total reflectivity from the solar cell stack is higher for the conformal design. Like in the periodic structure investigation an additional scattering from a textured silver back reflector is not beneficial for the light trapping quality. Especially for small periods P < 1.2 μm it leads to a higher reflectivity of the total cell. The generated higher order angles for long wavelength light are conserved for the flat back reflector and the probability for an out-coupling of the light from the cell is reduced.

The h = 400 nm case was investigated in detail as the currents for many individual period sizes for this structure height have been calculated in the periodic pyramid study. Also, the structure height of 400 nm showed very high currents for many period sizes.

Nevertheless, the morphology of this structure might have too steep structures (P = 400 nm, h = 400 nm with a small pyramid opening angle α = 53°). This might lead to shunts in the solar cell.

Next, the spectral response of the quasi random texture is simulated for a uniform pyramid height h = 300 nm. In the periodic pyramid calculation for h = 300 nm the J_{sc} currents are 1-2 mA/cm^2 lower (for all P > 500 nm) than for h = 400 nm (flat back reflector case). In comparison to the h = 400 nm case the QE of the h = 300 nm structure shows pronounced interference fringes of ~ 5 % magnitude for 500 nm < λ < 900 nm, see Fig. 9.4.

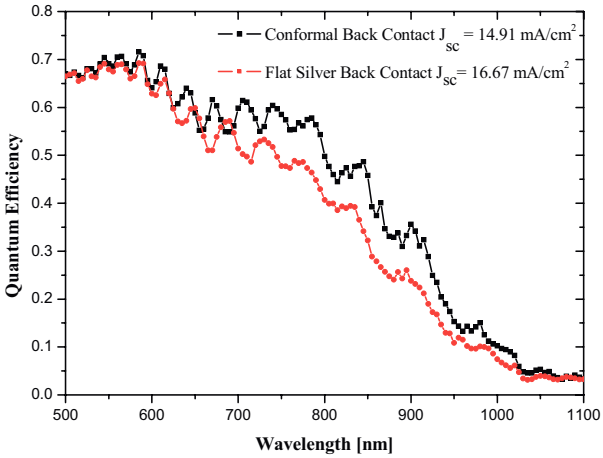

Fig. 9.4: QE calculation of Quasi Random structure with both back reflector types with h = 300 nm. The period size varies with P = 400 nm – 1.2 µm.

For the conformal back reflector design J_{sc} = 14.91 mA/cm^2 was calculated. This is ~ +0.3 mA/cm^2 higher than for the h = 400 nm case. For the flat design the *QE* is significantly enhanced to J_{sc} =16.67 mA/cm^2 by a reduction of the uniform structure height from h = 400 nm to h = 300 nm. In both cases the Quasi Random structure does not show the same structure height dependence of the short circuit current as in the case of periodic textures. For periodic structures h = 400 nm is clearly better for the light trapping properties than h = 300 nm for all P > 500 nm.

A possible explanation for a shifting of the optimum in J_{sc} to lower structure heights could be that for a random distribution of scattered light (in a Quasi Random structure) all light rays that are propagating in the x-y-direction (perpendicular to the direction of light incidence on the solar cell) travel through an absorber layer that has an effective layer thickness that is reduces by the height of the pyramids.

I.e. the absorber layer thickness d = 1 µm is reduced to

$$d_{eff} = d - h \tag{9.2}$$

with d_{eff} = 600 nm for h = 400 nm and d_{eff} = 700 nm for h = 300 nm.

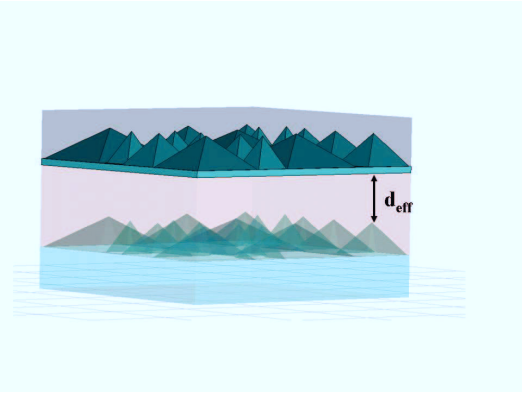

Fig. 9.5. Definition of effective absorber layer thickness d_{eff}.

This effective thickness allows all waves to propagate until absorption or until they are incident on a pyramid of the front or back side of the silicon.

The influences of the reflector design on the absorption in the front TCO is as described in the h = 400 nm case.

A further reduction of the uniform texture height to h = 200 nm is performed. This leads to an increase in magnitude of the interference fringes. Especially for 600 nm < λ < 900 nm the magnitude of the neighbouring interference fringes exceeds 10 % on the *QE* scale, see Fig. 9.6.

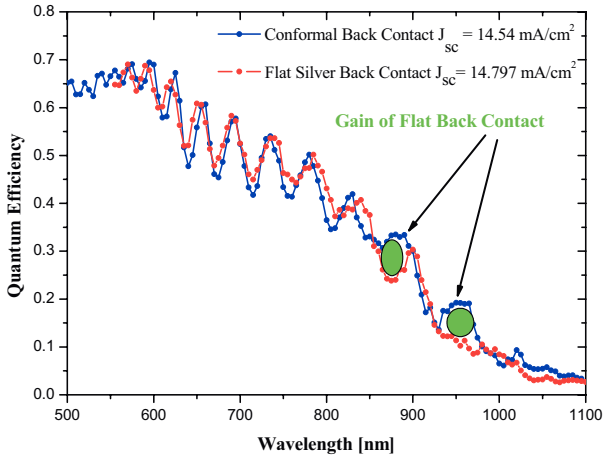

Fig. 9.6: QE calculation of Quasi Random structure with both back reflector types with h = 200 nm. For this small structure height both designs show similar short circuit currents.

For a flat, untextured solar cell the appearance of very strong interference fringes within the *QE* can be attributed to a constructive or destructive superposition of incoming and reflected plane waves leading to pronounced interferences. In case of a grating solar cell with non ideal parameters for light trapping ($P > 3$ µm) a high percentage of undiffracted, specular light also leads to strong interferences. This can be seen in the chapter about the line grating structure. The three calculated short-circuit currents of the Quasi Random structure are summarized the following table (reduced spectrum for simplicity is 500 nm < λ < 1100 nm):

structure height *h*	conformal back reflector	flat back reflector
200 nm	14.54 mA/cm^2	14.797 mA/cm^2
300 nm	14.91 mA/cm^2	16.67 mA/cm^2
400 nm	14.61 mA/cm^2	16.04 mA/cm^2

Table 9.4: Calculated short-circuit currents of the Quasi Random structure for different uniform structure heights.

In conclusion it can be mentioned that as in the periodic approach the flat back reflector is a better design for light trapping. For the conformal back reflector design the structure height is not as important as for the flat design as a strong anti-reflection effect and enhanced diffraction of steep structure (both effects generated at the front interface) is almost counterbalanced by an increased out-coupling generated by the conformal textured back reflector. A flat back reflector is likely to conserve a large amount of diffracted light for higher structures with $h > 300$ nm.

Next, the unit cell of Fig. 9.1 was stretched in x- and y-direction. This leads to a unit cell with $A = 4.228\ \mu m \times 4.228\ \mu m = 17.88\ \mu m^2$ representing pyramid period sizes P = 0.56 µm – 1.7 µm. For the periodic single pyramid texture the conformal back reflector leads to higher currents for larger pyramids. This was also found in the Quasi Random approach. The larger pyramids enhance the current by plus ~ 0.5 mA/cm^2.

Again the current of this Quasi Random structure is close to a superposition of the individual single pyramid currents.

A beneficial randomization of scattered light (as often mentioned in literature) by a random texture distribution is not observed in our optical simulations.

A periodic structure with the characteristic features: interface shape, period size and structure height is generally expected to offer more potential for a controllable fine tuning of the light trapping properties than the common random texture concepts.

Conclusion

The first structures used for the investigation of light trapping in thin-film silicon solar cells were binary gratings. They were ideal to test the simulation method and learn about the optical properties as they have only two basic structure parameters, i.e. the period size and the structure height. A comparison of prototype thin-film silicon solar cells with gratings as interface texture showed similar results and trends as in the corresponding Maxwell simulation models of gratings solar cells. The simulation method was thus verified.

The Maxwell simulations were further optimized and showed stable and reliable results for numerous solar cell designs. Several parameters like the individual thickness of the absorber or TCO layer(s) were varied and their influence on the optical response of the solar cell discussed.

The 1D grating design was modified and 2D and 3D structures were successfully tested. They showed significantly improved incoupling properties especially for blue light.

A modification of the cell design from a 2D to a 3D structure resulted in the same blue response but a strongly enhanced red response for the 3D structure.

To further optimize the short-circuit current of the solar cell novel structures with pyramidal multi-step interface and single pyramids with flat interfaces were modeled and the optimum parameters for the period size and pyramid height were calculated. The design of the back reflector, consisting of a 80 nm thick TCO (ZnO) and silver layer, has a strong influence on the optical response. For a flat back reflector design, with a flat interface between the back-TCO and Silver layer, the ideal period size of the pyramid was calculated with P ~ 1 µm. A conformal back reflector, which is the common approach in most labs, shows the highest short circuit currents for a period size of P ~ 2 µm.

After the periodic pyramid approach a solar cell design with a distribution of different pyramid sizes was investigated. The often proposed “beneficial randomization effect” that “shall” be present for randomly textured interfaces was not discovered. The short circuit current of a large, quasi random unit cell with an area of ~ 18.3 μm^2 and a distribution of different pyramid sizes showed almost a superposition of the current of the individual pyramids generated in the single periodic approach. This leads to the conclusion that a

periodic 3D pyramid shaped structure has a strong potential as light trapping texture. A fine tuning of the period size and the height of the pyramid can be used to reach high short circuit currents. Currently, there are many nano-techniques under investigation to find a way to integrate a periodic nano / sub-micrometer texture into a thin-film silicon solar cell. To implement these structures it is either possible to structure the substrate itself or a transparent lacquer on top of the glass substrate.

First prototypes of thin-film silicon solar cells with a periodic pyramid like interface texture in amorphous and microcrystalline single junction configuration were recently fabricated [1].
The periodic texture was "written" in a transparent lacquer on top of a standard glass substrate. An optical lithography replication method known from optical data storage techniques was used to texture a transparent lacquer on top of a glass substrate.

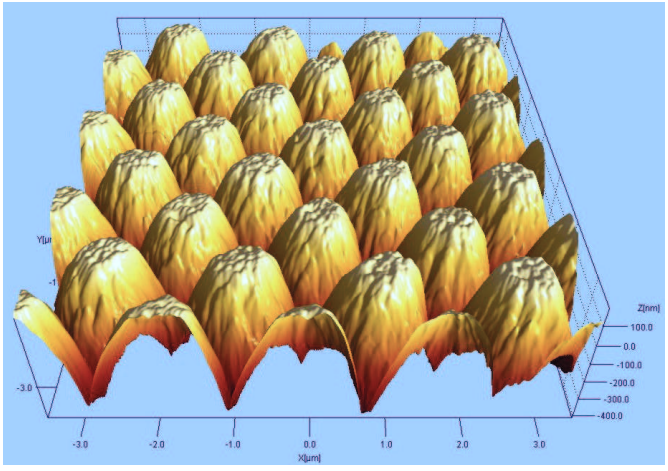

Fig. 1: AFM scan of a periodic texture that was "written" with an optical replication method common in the optical data storage industry. The texture is in a transparent lacquer on top of a standard glass substrate [1].

[1] Erven, A.J.M., Franken R. H.,. de Ruijter J, Peeters P.,. Vugts W, Isabella O., Zeman M., Haase C., Rau U., Borg H., 'Controlled texturing of thin-film silicon solar cell substrates', Proceedings of the 22nd European Photovoltaic Solar Energy Conference, Valencia, Spain – 2008. p. 1597

List of publications

2005:

Haase, C.; Brammer, T.; Senoussaoui, N.; Stiebig, H. 'Optical Simulations of Thin-Film Silicon Solar Cells with Integrated Grating Couplers' Proceedings of the 20th European Photovoltaic Solar Energy Conference and Exhibition, 6-10 June, Barcelona, Spain. - 2005. - p. 1647

Haase, C.; Stiebig, H. 'Light In-Coupling in Thin-Film Silicon Solar Cells with Periodically Textured Grating Couplers' Proceedings of the 15th International Photovoltaic Science and Engineering Conference (PVSEC-15), October 10-15, Shanghai, China. - 2005. - p. 790

Stiebig, H.; Reetz, W.; **Haase, C.;** Repmann, T.; Rech, B. 'Stability of Non-encapsulated Thin-film Silicon Solar Cells in Damp Heat Tests' Proceedings of the 15th International Photovoltaic Science and Engineering Conference, PVSEC-15, Shanghai, China. - 2005. - p. 561 - 562

2006:

Haase, C.; Stiebig, H. 'Optical properties of thin-film silicon solar cells with grating couplers' *Progress in Photovoltaics: Research and Applications* 14 (2006), 629 - 641 10.1002/pip.694

Haase, C.; Stiebig, H.; Thin-film silicon solar cells with diffractive elements, Proceedings of the 21st European Photovoltaic Solar Energy Conference, Dresden, Germany - 2006. p 1712

Haase, C. ; Stiebig, H. 'Fundamental optical simulations of light trapping in microcrystalline thin-film silicon solar cells' Photonics Europe 2006 : Optoelectronics and Photonic Materials. - SPIE, 2006. - (Proceedings of the SPIE ; 6197). - p. 32

Haase, C.; Stiebig, H. 'Light trapping in thin-film silicon solar cells with periodic structures' Proceedings of the IEEE World Conference on Photovoltaic Energy Conversion, Hawaii, USA, 2006. - 2006. - p. 1509

Haase, C.; Stiebig, H. 'Thin-film silicon solar cells with diffractive elements' *SPIE Newsroom*, 10.1117/2.1200602.0150

Stiebig, H.; Senoussaoui, N.; Zahren, C.; **Haase, C.**; Müller, J. 'Silicon thin-film solar cells with rectangular shaped grating couplers' *Progress in Photovoltaics : Research and Applications* 14 (2006), p. 13 – 24

Stiebig, H.; **Haase, C**.; Zahren, C.; Rech, B.; Senoussaoui, N. 'Thin-film silicon solar cells with grating couplers - an experimental and numerical study' *Journal of Non-Crystalline Solids* 352 (2006), p. 1949

Stiebig, H.; Schulte, M.; Zahren, C.; **Haase, C**.; Rech, B.; Lechner, P. 'Light trapping in thin-film silicon solar cells by nano-textured interfaces' Photonics Europe 2006 : Optoelectronics and Photonic Materials. - SPIE, 2006. - (Proceedings of the SPIE ; 6197).-p.1

2007:
Haase, C.; Stiebig, H. 'Thin-film silicon solar cells with efficient periodic light trapping texture' *Applied Physics Letters* 91 (2007), 061116

Haase, C.; Knipp, D.; Stiebig, H., Periodic Pyramid Texture for Efficient Light Trapping in Thin-Film Silicon Solar Cells, Proceedings of the 21st European Photovoltaic Solar Energy Conference, Milano, Italy – 2007. p. 2186

2008:
Haase, C.; Rau, U.; Stiebig, H. 'Efficient light trapping scheme by periodic and quasi-random nanostructures 'Proceedings of the 33rd IEEE Photovoltaics Specialists Conference, San Diego, CA, USA 2008. - 2008. - A5, p. 171

Obermeyer, P.; **Haase, C.**; Stiebig, H. Advanced light trapping management by diffractive interlayer for thin-film silicon solar cells, *Applied Physics Letters* 92 (2008), 181102

Stiebig, H.; **Haase, C**.; Jorke, S.; Obermeyer, P.; Moulin, E.; Schulte, M. 'New Management concepts for thin-film silicon solar cells' Light management in photovoltaic devices - theory and practice, MRS, 2008. - KK06-03

Erven, A.J.M., Franken R. H.,. de Ruijter J, Peeters P.,. Vugts W, Isabella O., Zeman M., **Haase C.**, Rau U., Borg H., 'Controlled texturing of thin-film silicon solar cell substrates', Proceedings of the 22nd European Photovoltaic Solar Energy Conference, Valencia, Spain – 2008. p. 1597

2009:
Stiebig, H.; **Haase, C**.; Schulte, M.; Hüpkes, J.; Beyer, W., Thin-Film Solar Cells with Patterned Surfaces, Technical Journal Galvanotechnik Ed. 03/2009,100 (2009)3, p. 646-652,

Pflaum, C.; **Haase, C.;** Stiebig, H.; Jandl, C.; Optical Efficiency of Thin-Film Silicon Solar Cells for Oblique Incident Waves, submitted to Journal of Progress in Photovoltaics, 2009

Pflaum, C.; **Haase, C.;** Stiebig, H.; Jandl, C.; Simulation of Light In-coupling at Oblique Angles in Thin-Film Silicon Solar Cells, submitted to Proceedings of the 23nd European Photovoltaic Solar Energy Conference, Hamburg, Germany

AWARDS:

1) **Outstanding Poster Award**
   "Light trapping in thin-film silicon solar cells with periodic structures"
   Amorphous/Microcrystalline Silicon Materials & Devices
   IEEE 4th World Conference on Photovoltaic Energy Conversion, Waikoloa, Hawaii, 2006
2) **Best Poster Prize**
   Wilhelm und Else Heraeus-Stiftung
   386. WE-Heraeus-Seminar, Physikzentrum Bad Honnef
   Computational Nano-Photonics Conference, 2007

Acknowledgements

Diese Arbeit wurde am Forschungszentrum Jülich im Institut für Photovoltaik und in Kooperation mit der School of Electrical Engineering and Science an der Jacobs University Bremen durchgeführt.
Für die sehr gute Betreuung meiner Arbeit an der Jacobs University Bremen möchte ich mich bei Professor Dietmar Knipp ausdrücklich bedanken.
Herrn Dr. Helmut Stiebig danke ich für die intensive Einarbeitung in das Thema Dünnfilm Silizium Photovoltaik und die sehr gute Einführung in die Thematik der Computer Simulationen.
Beim Institutsdirektor in Jülich, Professor Uwe Rau, bedanke ich mich für die Einbindung ins Institutsleben und die Möglichkeit bei zukunftsweisenden Projektförderanträgen und multilateralen Kooperationen selbstständig mitarbeiten zu dürfen.
Für die Übernahme des Koreferats danke ich Herrn Professor Werner Bergholz. Es ist sehr ermutigend für mich wenn ein so erfahrener Experte der Silizium Mikroelektronik voller Begeisterung die Parallelen in der Lernkurve von Solartechnologie und Computerchips sieht.

Meinen Kollegen im Forschungszentrum möchte ich für die fachliche Unterstützung ebenso wie für die angenehme und lockere Atmosphäre danken. Hervorheben möchte ich Thilo Kilper, Andreas Lambertz, Gunnar Schöpe, Urs Aeberhardt, Thomas Kirchartz, Matthias Schneemann, Uli Paetzold, Christoph Pflaum, Michelle Bosquet, Bart Pieters, Aad Goordijn, Jürgen Hüpkes, Wolfhard Beyer, Friedhelm Finger, Reinhard Carius, Dimitri Hrunski, Torsten Brammer, und Christoph Zahren.

Ganz besonderen Dank möchte ich an meine Familie richten, die in allen Lebenslagen zu mir hält und auf die ich mich immer verlassen kann.

Christian Haase

1. **Einsatz von multispektralen Satellitenbilddaten in der Wasserhaushalts- und Stoffstrommodellierung – dargestellt am Beispiel des Rureinzugsgebietes**
   von C. Montzka (2008), XX, 238 Seiten
   ISBN: 978-3-89336-508-1

2. **Ozone Production in the Atmosphere Simulation Chamber SAPHIR**
   by C. A. Richter (2008), XIV, 147 pages
   ISBN: 978-3-89336-513-5

3. **Entwicklung neuer Schutz- und Kontaktierungsschichten für Hochtemperatur-Brennstoffzellen**
   von T. Kiefer (2008), 138 Seiten
   ISBN: 978-3-89336-514-2

4. **Optimierung der Reflektivität keramischer Wärmedämmschichten aus Yttrium-teilstabilisiertem Zirkoniumdioxid für den Einsatz auf metallischen Komponenten in Gasturbinen**
   von A. Stuke (2008), X, 201 Seiten
   ISBN: 978-3-89336-515-9

5. **Lichtstreuende Oberflächen, Schichten und Schichtsysteme zur Verbesserung der Lichteinkopplung in Silizium-Dünnschichtsolarzellen**
   von M. Berginski (2008), XV, 171 Seiten
   ISBN: 978-3-89336-516-6

6. **Politikszenarien für den Klimaschutz IV – Szenarien bis 2030**
   hrsg.von P. Markewitz, F. Chr. Matthes (2008), 376 Seiten
   ISBN 978-3-89336-518-0

7. **Untersuchungen zum Verschmutzungsverhalten rheinischer Braunkohlen in Kohledampferzeugern**
   von A. Schlüter (2008), 164 Seiten
   ISBN 978-3-89336-524-1

8. **Inorganic Microporous Membranes for Gas Separation in Fossil Fuel Power Plants**
   by G. van der Donk (2008), VI, 120 pages
   ISBN: 978-3-89336-525-8

9. **Sinterung von Zirkoniumdioxid-Elektrolyten im Mehrlagenverbund der oxidkeramischen Brennstoffzelle (SOFC)**
   von R. Mücke (2008), VI, 165 Seiten
   ISBN: 978-3-89336-529-6

10. **Safety Considerations on Liquid Hydrogen**
    by K. Verfondern (2008), VIII, 167 pages
    ISBN: 978-3-89336-530-2

11. **Kerosinreformierung für Luftfahrtanwendungen**
    von R. C. Samsun (2008), VII, 218 Seiten
    ISBN: 978-3-89336-531-9

12. **Der 4. Deutsche Wasserstoff Congress 2008 – Tagungsband**
    hrsg. von D. Stolten, B. Emonts, Th. Grube (2008), 269 Seiten
    ISBN: 978-3-89336-533-3

13. **Organic matter in Late Devonian sediments as an indicator for environmental changes**
    by M. Kloppisch (2008), XII, 188 pages
    ISBN: 978-3-89336-534-0

14. **Entschwefelung von Mitteldestillaten für die Anwendung in mobilen Brennstoffzellen-Systemen**
    von J. Latz (2008), XII, 215 Seiten
    ISBN: 978-3-89336-535-7

15. **RED-IMPACT**
    Impact of Partitioning, Transmutation and Waste Reduction Technologies on the Final Nuclear Waste Disposal
    SYNTHESIS REPORT
    ed. by W. von Lensa, R. Nabbi, M. Rossbach (2008), 178 pages
    ISBN 978-3-89336-538-8

16. **Ferritic Steel Interconnectors and their Interactions with Ni Base Anodes in Solid Oxide Fuel Cells (SOFC)**
    by J. H. Froitzheim (2008), 169 pages
    ISBN: 978-3-89336-540-1

17. **Integrated Modelling of Nutrients in Selected River Basins of Turkey**
    Results of a bilateral German-Turkish Research Project
    project coord. M. Karpuzcu, F. Wendland (2008), XVI, 183 pages
    ISBN: 978-3-89336-541-8

18. **Isotopengeochemische Studien zur klimatischen Ausprägung der Jüngeren Dryas in terrestrischen Archiven Eurasiens**
    von J. Parplies (2008), XI, 155 Seiten, Anh.
    ISBN: 978-3-89336-542-5

19. **Untersuchungen zur Klimavariabilität auf dem Tibetischen Plateau - Ein Beitrag auf der Basis stabiler Kohlenstoff- und Sauerstoffisotope in Jahrringen von Bäumen waldgrenznaher Standorte**
    von J. Griessinger (2008), XIII, 172 Seiten
    ISBN: 978-3-89336-544-9

20. **Neutron-Irradiation + Helium Hardening & Embrittlement Modeling of 9%Cr-Steels in an Engineering Perspective (HELENA)**
by R. Chaouadi (2008), VIII, 139 pages
ISBN: 978-3-89336-545-6

21. **in Bearbeitung**

22. **Verbundvorhaben APAWAGS (AOEV und Wassergenerierung) – Teilprojekt: Brennstoffreformierung – Schlussbericht**
von R. Peters, R. C. Samsun, J. Pasel, Z. Porš, D. Stolten (2008), VI, 106 Seiten
ISBN: 978-3-89336-547-0

23. **FREEVAL**
Evaluation of a Fire Radiative Power Product derived from Meteosat 8/9 and Identification of Operational User Needs
Final Report
project coord. M. Schultz, M. Wooster (2008), 139 pages
ISBN: 978-3-89336-549-4

24. **Untersuchungen zum Alkaliverhalten unter Oxycoal-Bedingungen**
von C. Weber (2008), VII, 143, XII Seiten
ISBN: 978-3-89336-551-7

25. **Grundlegende Untersuchungen zur Freisetzung von Spurstoffen, Heißgaschemie, Korrosionsbeständigkeit keramischer Werkstoffe und Alkalirückhaltung in der Druckkohlenstaubfeuerung**
von M. Müller (2008), 207 Seiten
ISBN: 978-3-89336-552-4

26. **Analytik von ozoninduzierten phenolischen Sekundärmetaboliten in *Nicotiana tabacum* L. cv Bel W3 mittels LC-MS**
von I. Koch (2008), III, V, 153 Seiten
ISBN 978-3-89336-553-1

27. **IEF-3 Report 2009. Grundlagenforschung für die Anwendung**
(2009), ca. 230 Seiten
ISBN: 978-3-89336-554-8

28. **Influence of Composition and Processing in the Oxidation Behavior of MCrAlY-Coatings for TBC Applications**
by J. Toscano (2009), 168 pages
ISBN: 978-3-89336-556-2

29. **Modellgestützte Analyse signifikanter Phosphorbelastungen in hessischen Oberflächengewässern aus diffusen und punktuellen Quellen**
von B. Tetzlaff (2009), 149 Seiten
ISBN: 978-3-89336-557-9

30. **Nickelreaktivlot / Oxidkeramik – Fügungen als elektrisch isolierende Dichtungskonzepte für Hochtemperatur-Brennstoffzellen-Stacks**
von S. Zügner (2009), 136 Seiten
ISBN: 978-3-89336-558-6

31. **Langzeitbeobachtung der Dosisbelastung der Bevölkerung in radioaktiv kontaminierten Gebieten Weißrusslands – Korma-Studie**
von H. Dederichs, J. Pillath, B. Heuel-Fabianek, P. Hill, R. Lennartz (2009), Getr. Pag.
ISBN: 978-3-89336-532-3

32. **Herstellung von Hochtemperatur-Brennstoffzellen über physikalische Gasphasenabscheidung**
von N. Jordán Escalona (2009), 148 Seiten
ISBN: 978-3-89336-532-3

33. **Real-time Digital Control of Plasma Position and Shape on the TEXTOR Tokamak**
by M. Mitri (2009), IV, 128 pages
ISBN: 978-3-89336-567-8

34. **Freisetzung und Einbindung von Alkalimetallverbindungen in kohlebefeuerten Kombikraftwerken**
von M. Müller (2009), 155 Seiten
ISBN: 978-3-89336-568-5

35. **Kosten von Brennstoffzellensystemen auf Massenbasis in Abhängigkeit von der Absatzmenge**
von J. Werhahn (2009), 242 Seiten
ISBN: 978-3-89336-569-2

36. **Einfluss von Reoxidationszyklen auf die Betriebsfestigkeit von anodengestützten Festoxid-Brennstoffzellen**
von M. Ettler (2009), 138 Seiten
ISBN: 978-3-89336-570-8

37. **Großflächige Plasmaabscheidung von mikrokristallinem Silizium für mikromorphe Dünnschichtsolarmodule**
von T. Kilper (2009), XVII, 154 Seiten
ISBN: 978-3-89336-572-2

38. **Generalized detailed balance theory of solar cells**
by T. Kirchartz (2009), IV, 198 pages
ISBN: 978-3-89336-573-9

39. **The Influence of the Dynamic Ergodic Divertor on the Radial Electric Field at the Tokamak TEXTOR**
von J. W. Coenen (2009), xii, 122, XXVI pages
ISBN: 978-3-89336-574-6

40. **Sicherheitstechnik im Wandel Nuklearer Systeme**
von K. Nünighoff (2009), viii, 215 Seiten
ISBN: 978-3-89336-578-4

41. **Pulvermetallurgie hochporöser NiTi-Legierungen für Implanat- und Dämpfungsanwendungen**
von M. Köhl (2009), XVII, 199 Seiten
ISBN: 978-3-89336-580-7

42. **Einfluss der Bondcoatzusammensetzung und Herstellungsparameter auf die Lebensdauer von Wärmedämmschichten bei zyklischer Temperaturbelastung**
von M. Subanovic (2009), 188, VI Seiten
ISBN: 978-3-89336-582-1

43. **Oxygen Permeation and Thermo-Chemical Stability of Oxygen Permeation Membrane Materials for the Oxyfuel Process**
by A. J. Ellett (2009), 176 pages
ISBN: 978-3-89336-581-4

44. **Korrosion von polykristallinem Aluminiumoxid (PCA) durch Metalljodidschmelzen sowie deren Benetzungseigenschaften**
von S. C. Fischer (2009), 148 Seiten
ISBN: 978-3-89336-584-5

45. **IEF-3 Report 2009. Basic Research for Applications**
(2009), 217 Seiten
ISBN: 978-3-89336-585-2

46. **Verbundvorhaben ELBASYS (Elektrische Basissysteme in einem CFK-Rumpf) - Teilprojekt: Brennstoffzellenabgase zur Tankinertisierung - Schlussbericht**
von R. Peters, J. Latz, J. Pasel, R. C. Samsun, D. Stolten
(2009), xi, 202 Seiten
ISBN: 978-3-89336-587-6

47. **Aging of ^{14}C-labeled Atrazine Residues in Soil: Location, Characterization and Biological Accessibility**
by N. D. Jablonowski (2009), IX, 104 pages
ISBN: 978-3-89336-588-3

48. **Entwicklung eines energetischen Sanierungsmodells für den europäischen Wohngebäudesektor unter dem Aspekt der Erstellung von Szenarien für Energie- und CO_2 - Einsparpotenziale bis 2030**
von P. Hansen (2009), XXII, 281 Seiten
ISBN: 978-3-89336-590-6

49. **Reduktion der Chromfreisetzung aus metallischen Interkonnektoren für Hochtemperaturbrennstofzellen durch Schutzschichtsysteme**
von R. Trebbels (2009), iii, 135 Seiten
ISBN: 978-3-89336-591-3

50. **Bruchmechanische Untersuchung von Metall / Keramik-Verbundsystemen für die Anwendung in der Hochtemperaturbrennstoffzelle**
von B. Kuhn (2009), 118 Seiten
ISBN: 978-3-89336-592-0

51. **Wasserstoff-Emissionen und ihre Auswirkungen auf den arktischen Ozonverlust**
Risikoanalyse einer globalen Wasserstoffwirtschaft
von T. Feck (2009), 180 Seiten
ISBN: 978-3-89336-593-7

52. **Development of a new Online Method for Compound Specific Measurements of Organic Aerosols**
by T. Hohaus (2009), 156 pages
ISBN: 978-3-89336-596-8

53. **Entwicklung einer FPGA basierten Ansteuerungselektronik für Justageeinheiten im Michelson Interferometer**
von H. Nöldgen (2009), 121 Seiten
ISBN: 978-3-89336-599-9

54. **Observation – and model – based study of the extratropical UT/LS**
by A. Kunz (2010), xii, 120, xii pages
ISBN: 978-3-89336-603-3

55. **Herstellung polykristalliner Szintillatoren für die Positronen-Emissions-Tomographie (PET)**
von S. K. Karim (2010), VIII, 154 Seiten
ISBN: 978-3-89336-610-1

56. **Kombination eines Gebäudekondensators mit H2-Rekombinatorelementen in Leichwasserreaktoren**
von S. Kelm (2010), vii, 119 Seiten
ISBN: 978-3-89336-611-8

57. **Plant Leaf Motion Estimation Using A 5D Affine Optical Flow Model**
by T. Schuchert (2010), X, 143 pages
ISBN: 978-3-89336-613-2

58. **Tracer-tracer relations as a tool for research on polar ozone loss**
by R. Müller (2010), 116 pages
ISBN: 978-3-89336-614-9

59. **Sorption of polycyclic aromatic hydrocarbon (PAH) to Yangtze River sediments and their components**
by J. Zhang (2010), X, 109 pages
ISBN: 978-3-89336-616-3

60. **Weltweite Innovationen bei der Entwicklung von CCS-Technologien und Möglichkeiten der Nutzung und des Recyclings von CO_2**
Studie im Auftrag des BMWi
von W. Kuckshinrichs et al. (2010), X, 139 Seiten
ISBN: 978-3-89336-617-0

61. **Herstellung und Charakterisierung von sauerstoffionenleitenden Dünnschichtmembranstrukturen**
von M. Betz (2010), XII, 112 Seiten
ISBN: 978-3-89336-618-7

62. **Politikszenarien für den Klimaschutz V – auf dem Weg zum Strukturwandel, Treibhausgas-Emissionsszenarien bis zum Jahr 2030**
hrsg. von P. Hansen, F. Chr. Matthes (2010), 276 Seiten
ISBN: 978-3-89336-619-4

63. **Charakterisierung Biogener Sekundärer Organischer Aerosole mit Statistischen Methoden**
von C. Spindler (2010), iv, 163 Seiten
ISBN: 978-3-89336-622-4

64. **Stabile Algorithmen für die Magnetotomographie an Brennstoffzellen**
von M. Wannert (2010), ix, 119 Seiten
ISBN: 978-3-89336-623-1

65. **Sauerstofftransport und Degradationsverhalten von Hochtemperatur-membranen für CO2-freie Kraftwerke**
von D. Schlehuber (2010), VII, 139 Seiten
ISBN: 978-3-89336-630-9

66. **Entwicklung und Herstellung von foliengegossenen, anodengestützten Festoxidbrennstoffzellen**
von W. Schafbauer (2010), VI, 164 Seiten
ISBN: 978-3-89336-631-6

67. **Disposal strategy of proton irradiated mercury from high power spallation sources**
by S. Chiriki (2010), xiv, 124 pages
ISBN: 978-3-89336-632-3

68. **Oxides with polyatomic anions considered as new electrolyte materials for solid oxide fuel cells (SOFCs)**
by O. H. Bin Hassan (2010), vii, 121 pages
ISBN: 978-3-89336-633-0

69. **Von der Komponente zum Stack: Entwicklung und Auslegung von HT-PEFC-Stacks der 5 kW-Klasse**
von A. Bendzulla (2010), IX, 203 Seiten
ISBN: 978-3-89336-634-7

70. **Satellitengestützte Schwerewellenmessungen in der Atmosphäre und Perspektiven einer zukünftigen ESA Mission (PREMIER)**
von S. Höfer (2010), 81 Seiten
ISBN: 978-3-89336-637-8

71. **Untersuchungen der Verhältnisse stabiler Kohlenstoffisotope in atmosphärisch relevanten VOC in Simulations- und Feldexperimenten**
von H. Spahn (2010), IV, 210 Seiten
ISBN: 978-3-89336-638-5

72. **Entwicklung und Charakterisierung eines metallischen Substrats für nanostrukturierte keramische Gastrennmembranen**
von K. Brands (2010), vii, 137 Seiten
ISBN: 978-3-89336-640-8

73. **Hybridisierung und Regelung eines mobilen Direktmethanol-Brennstoff-zellen-Systems**
von J. Chr. Wilhelm (2010), 220 Seiten
ISBN: 978-3-89336-642-2

74. **Charakterisierung perowskitischer Hochtemperaturmembranen zur Sauerstoffbereitstellung für fossil gefeuerte Kraftwerksprozesse**
von S.A. Möbius (2010) III, 208 Seiten
ISBN: 978-3-89336-643-9

75. **Characterization of natural porous media by NMR and MRI techniques: High and low magnetic field studies for estimation of hydraulic properties**
by L.-R. Stingaciu (2010), 96 pages
ISBN: 978-3-89336-645-3

76. **Hydrological Characterization of a Forest Soil Using Electrical Resistivity Tomography**
by Chr. Oberdörster (2010), XXI, 151 pages
ISBN: 978-3-89336-647-7

77. **Ableitung von atomarem Sauerstoff und Wasserstoff aus Satellitendaten und deren Abhängigkeit vom solaren Zyklus**
von C. Lehmann (2010), 127 Seiten
ISBN: 978-3-89336-649-1

78. **18th World Hydrogen Energy Conference 2010 – WHEC2010 Proceedings**
Speeches and Plenary Talks
ed. by D. Stolten, B. Emonts (2010)
ISBN: 978-3-89336-658-3

78-1. **18th World Hydrogen Energy Conference 2010 – WHEC2010 Proceedings**
Parallel Sessions Book 1:
Fuel Cell Basics / Fuel Infrastructures
ed. by D. Stolten, T. Grube (2010), ca. 460 pages
ISBN: 978-3-89336-651-4

78-2. **18th World Hydrogen Energy Conference 2010 – WHEC2010 Proceedings**
Parallel Sessions Book 2:
Hydrogen Production Technologies – Part 1
ed. by D. Stolten, T. Grube (2010), ca. 400 pages
ISBN: 978-3-89336-652-1

78-3. **18th World Hydrogen Energy Conference 2010 – WHEC2010 Proceedings**
Parallel Sessions Book 3:
Hydrogen Production Technologies – Part 2
ed. by D. Stolten, T. Grube (2010), ca. 640 pages
ISBN: 978-3-89336-653-8

78-4. **18th World Hydrogen Energy Conference 2010 – WHEC2010 Proceedings**
Parallel Sessions Book 4:
Storage Systems / Policy Perspectives, Initiatives and Cooperations
ed. by D. Stolten, T. Grube (2010), ca. 500 pages
ISBN: 978-3-89336-654-5

78-5. **18th World Hydrogen Energy Conference 2010 – WHEC2010 Proceedings**
Parallel Sessions Book 5:
Stategic Analysis / Safety Issues / Existing and Emerging Markets
ed. by D. Stolten, T. Grube (2010), ca. 530 pages
ISBN: 978-3-89336-655-2

78-6. **18th World Hydrogen Energy Conference 2010 – WHEC2010 Proceedings**
Parallel Sessions Book 6:
Stationary Applications / Transportation Applications
ed. by D. Stolten, T. Grube (2010), ca. 330 pages
ISBN: 978-3-89336-656-9

78 Set (complete book series)

18th World Hydrogen Energy Conference 2010 – WHEC2010 Proceedings
ed. by D. Stolten, T. Grube, B. Emonts (2010)
ISBN: 978-3-89336-657-6

79. **Ultrafast voltex core dynamics investigated by finite-element micromagnetic simulations**
by S. Gliga (2010), vi, 144 pages
ISBN: 978-3-89336-660-6

80. **Herstellung und Charakterisierung von keramik- und metallgestützten Membranschichten für die CO_2-Abtrennung in fossilen Kraftwerken**
von F. Hauler (2010), XVIII, 178 Seiten
ISBN: 978-3-89336-662-0

81. **Experiments and numerical studies on transport of sulfadiazine in soil columns**
by M. Unold (2010), xvi, 115 pages
ISBN: 978-3-89336-663-7

82. **Prompt-Gamma-Neutronen-Aktivierungs-Analyse zur zerstörungsfreien Charakterisierung radioaktiver Abfälle**
von J.P.H. Kettler (2010), iv, 205 Seiten
ISBN: 978-3-89336-665-1

83. **Transportparameter dünner geträgerter Kathodenschichten der oxidkeramischen Brennstoffzelle**
von C. Wedershoven (2010), vi, 137 Seiten
ISBN: 978-3-89336-666-8

84. **Charakterisierung der Quellverteilung von Feinstaub und Stickoxiden in ländlichem und städtischem Gebiet**
von S. Urban (2010), vi, 211 Seiten
ISBN: 978-3-89336-669-9

85. **Optics of Nanostructured Thin-Film Silicon Solar Cells**
by C. Haase (2010), 150 pages
ISBN: 978-3-89336-671-2

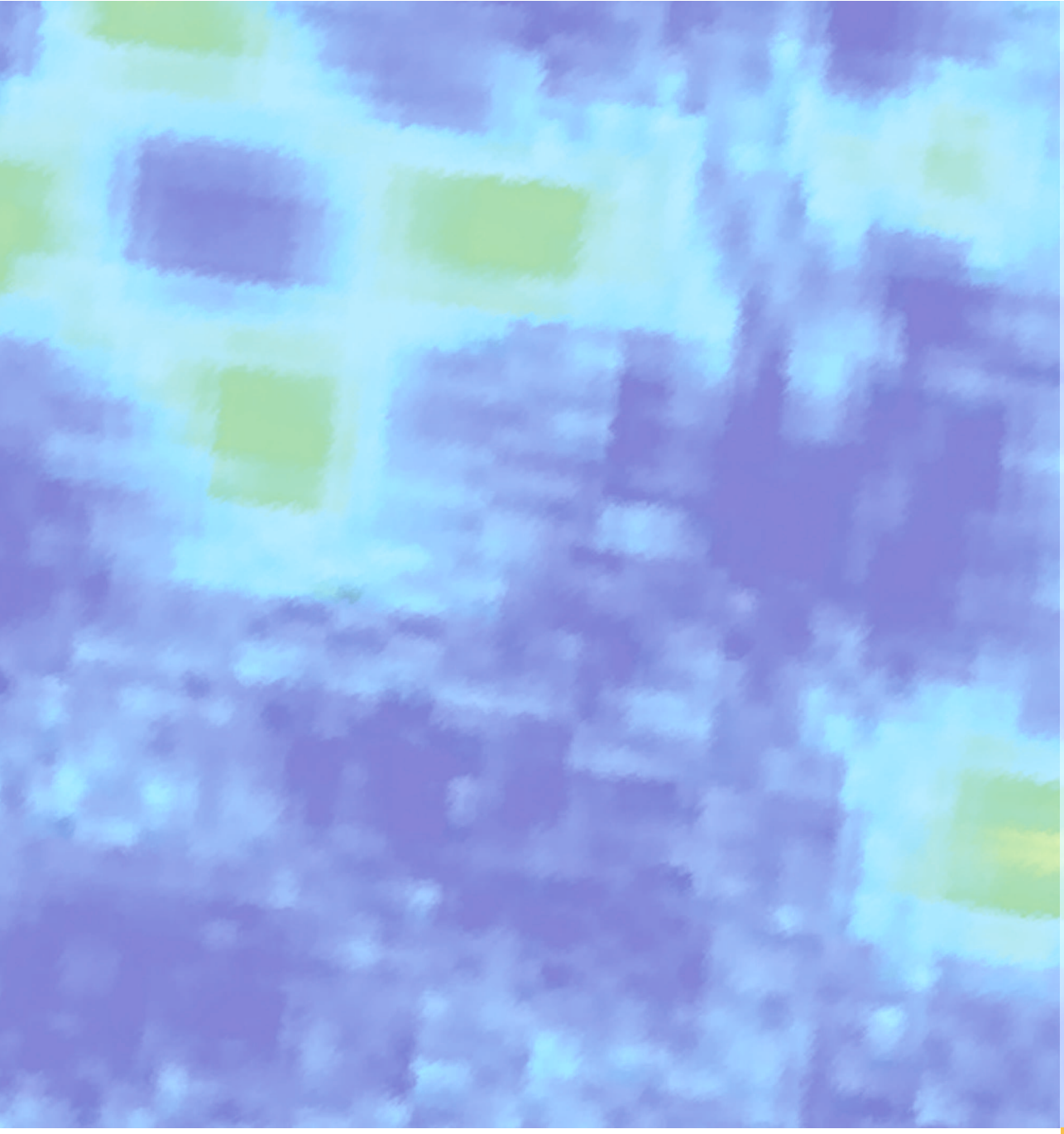

Energie & Umwelt / Energy & Environment
Band / Volume 85
ISBN 978-3-89336-671-2

JÜLICH
FORSCHUNGSZENTRUM